

**Search for ADD large extra dimensions in
 $\gamma + \cancel{E}_T$ final state in proton proton collisions,
using The Compact Muon Solenoid Detector
at The Large Hadron Collider**

**Thesis submitted to The University of Calcutta
for the degree of
DOCTOR OF PHILOSOPHY**

SUBMITTED BY: Sandhya Jain
SAHA INSTITUTE OF NUCLEAR
PHYSICS
1/AF, SALT LAKE CITY
BIDHAN NAGAR,
KOLKATA-700064

UNDER THE SUPERVISION OF

Satyaki Bhattacharya
SAHA INSTITUTE OF NUCLEAR PHYSICS
1/AF, SALT LAKE CITY
BIDHAN NAGAR,
KOLKATA-700064

Gautam Gangopadhyay
DEPARTMENT OF PHYSICS
UNIVERSITY OF CALCUTTA
92, A.P.C ROAD
KOLKATA-700009

March 19, 2014

*Dedicated
To
the memory of my babaji*

Acknowledgements

Completing thesis work would not have been possible without the support of my family, friends and colleagues. I was blessed to work at various places and with many collaborators during these years. I would like to express my gratitude to all of you in the following without who I would not be here.

Foremost, I would like to thank my supervisor Prof. Satyaki Bhattacharya for introducing me to this area of research and seeding the interest that still lightens the path ahead. His guidance and support enabled to develop a basic understanding of the subject. I am heartily thankful to Prof. Debajyoti Choudhury for his joint supervision and his training while I was at University of Delhi. His anxious questions always helped me to think broadly and grow as an independent individual. I am extremely grateful to Prof. Gautam Gangopadhyay for offering his joint supervision at University of Calcutta while migrating to the Saha Institute of Nuclear Physics (SINP). His constant support never let me worry about any of the involved official matters. I am sincerely thankful to Prof. Sunanda Banerjee for his throughout encouragement, tremendous support and useful advices. His knowledge, efficiency and patience at work will continue to motivate me always. I would like to extend my thanks to the entire CMS group of SINP and University of Delhi for providing me a nice working environment.

I am indebted to all my collaborators at CERN with whom I have worked for my analysis. In particular, I would like to thank Prof. Albert De Roeck and Dr. Umberto Berzano with whom I performed my first analysis based on Monte-Carlo simulations. It was a great time working with both of them. I learned basic ingredients and the challenges to perform this search starting from the initial level to the final level with them. This experience helped me to perform the analysis discussed in this thesis with 7 TeV data. For the monophoton analysis at 7 TeV, I would like to thank everyone in the team for their timeless efforts and discussions. It has been a pleasure working with all of them.

Dr. David Anthony Petyt has been a source of inspiration. With his deep sense of knowledge, expertise and experience, I learned a lot about the detector related challenges. His continuous guidance and discussions helped me to build up a profound understanding of the results.

I would like to thank every member of India-CMS collaboration with whom I have interacted, discussed physics and had fun apart from the dedicated time at work. I would like to take this as an opportunity to thank a few explicitly. Sudha, you have been an awesome friend. Thanks for being what you have been. Shilpi, I have learned many lessons being with you throughout and am really thankful to you for all of it. Pratishruti, I will always appreciate the constructive discussions that we had. Bhawna, Raman, Varun, Ruchi, Sanmay, Pooja, Arun, Shivali, Atanu, Kalyanmoy, Debarati, Swagata, I would

really like to thank you all for being there and for the much valuable friendship. I will really miss the time that we spent together and the discussions we had. I really appreciate all the help that you provided me in the time of need.

My research activities have been supported by the University Grants Commission (UGC), Govt. of India and the SINP, Kolkata. The travel grants were funded by Department of Science and Technology (DST), Govt. of India and Department of Atomic Energy (DAE), Govt. of India. I would like to acknowledge all of these for providing me a financial support throughout.

I would like to thank all my friends who have been there to make me smile through difficult times. And finally ofcourse, this journey would not have been possible without the endless faith, unconditional love and support of my family. I love you all deep from my heart. Thank you all very much.

List of Publications Related to Thesis

- **Measurement of the production cross section for $Z\gamma \rightarrow \nu\bar{\nu}\gamma$ in pp collisions at $\sqrt{s} = 7$ TeV and limits on trilinear gauge boson couplings $ZZ\gamma$ and $Z\gamma\gamma$, CMS collaboration,**
JHEP 10 (2013) 164
- **Search for Dark Matter and Large Extra Dimensions in pp collisions Yielding a Photon and Missing Transverse Energy, CMS collaboration**
Phy. Rev. Lett. 108, 261803, 2012.

List of Conference Reports

- **Measurement of the cross-section of $Z\gamma$ and limits on ADD models at the CMS with 7 TeV Large Hadron Collider data, Sandhya Jain**
Pramana, Volume 79, Issue 4 (2012), 925.

Other Technical Publications

- **Assembly, testing and production of bakelite RPCs for the end-cap region of the Compact Muon Solenoid experiment at CERN, L.M. Pant, S.D. Tripathi, P. Shukla, D. Dutta, V. Kumar, A.K. Mohanty, R.K. Choudhury, S. Kailas, A.K. Dubey, Shilpi Jain, Sandhya Jain, S. Ahuja, S.P. Singh, A. Sharma, J.B. Singh, S.B. Beri,**
Nuclear Instruments and Methods in Physics Research Section A: Accelerators, Spectrometers, Detectors and Associated Equipment,
<http://dx.doi.org/10.1016/j.nima.2008.12.208>

List of Internal Notes Related to Thesis

- **Search for Large Extra Dimension in the ADD model using photon plus MET final state in early CMS data, Umberto Berzano, Satyaki Bhattacharya, Sandhya Jain, Albert De Roeck, AN-2009-191.**
- **$Z\gamma$ at $\sqrt{s} = 7$ TeV where Z Decays Invisibly, N. Akchurin, A. Askew, S. Bhattacharya, S. Chauhan, J. Damgov, B. Gomber, Sa. Jain, C. Kopecky, S.W. Lee, Y. Maravin, T. Miceli, S. Shrestha, I. Svintradze, M. Tripathi, and M. Weinberg, AN-11-108.**

- Search for ADD Extra-dimensions with Photon + MET signature, N. Akchurin, A. Askew, U. Berzano, S. Bhattacharya, S. Chauhan, J. Damgov, B. Gomber, Sa. Jain, C. Kopecky, S.W. Lee, Y. Maravin, T. Miceli, A. Nowack, S. Shrestha, I. Svintradze, M. Tripathi, and M.Weinberg, **AN-11-319**.
- Search for Extra Dimensions using the Monophoton Final State, A. Askew, Y. Maravin, S. Shrestha, I. Svintradze, Sa. Jain, B. Gomber, S. Bhattacharya, J. Damgov, S. Lee, N. Akchurin, M. Tripathi, T. Miceli, C. Kopecky, S. Chauhan, A. Nowack, U. Berzano, **EXO-11-058**.

Contents

Contents	vi
List of Figures	ix
List of Tables	xiv
1 The Theoretical Perspective	3
1.1 Standard Model of Particle Physics	3
1.1.1 Shortcomings of the Standard Model	7
1.2 Introduction to ADD Large Extra Dimensions	7
1.3 Searches for ADD Large Extra Dimensions at Large Hadron Collider	9
1.4 Previous Limits on ADD Extra Dimensions	11
2 The Experimental Setup	13
2.1 LHC	13
2.2 CMS	15
2.2.1 The Superconducting Magnet	17
2.2.2 The Inner Tracking System	17
2.2.3 The Electromagnetic Calorimeter	20
2.2.4 The Hadron Calorimeter	22
2.2.5 The Muon System	24
3 The Data Handling & Event Reconstruction	26
3.1 The Trigger System	26
3.1.1 Level-1 Trigger System	27
3.1.2 Data Acquisition System and High Level Trigger	28
3.2 Event Reconstruction	30
3.2.1 Tracks & Vertex reconstruction	30
3.2.2 Electrons	31
3.2.3 Muons	32

3.2.4	Jets & Missing Transverse Energy	32
3.3	Photon Reconstruction	33
3.3.1	Clustering Algorithms	34
3.4	Monte Carlo Simulation	36
4	Anomalous signals in CMS Electromagnetic Calorimeter	38
4.1	Spike properties	38
4.2	Rejection algorithms	40
4.3	Spike killing efficiency using 2012 data	42
4.4	Spike simulation	44
4.4.1	Validation of spike simulation using 8 TeV data	44
4.4.2	Validation of spike simulation at 14 TeV	45
4.5	Future projections	47
4.5.1	Offline spike killing performance	48
4.5.2	Online Spike Rejection Performance	53
4.6	Summary	55
5	Analysis	57
5.1	Signal	58
5.2	Backgrounds	60
5.3	Event Selection	61
5.4	Selection Efficiencies	65
5.4.1	Trigger selection	65
5.4.2	Photon identification	66
5.4.3	Embedded spike removal	67
5.4.4	Veto efficiency	68
5.5	Backgrounds estimates using Monte Carlo	69
5.5.1	Rescaling of MC for pileup distribution	70
5.6	Data-driven estimates	71
5.6.1	Jet fakes photon background	71
5.6.2	Electron faking photon background	73
5.6.3	Non-collision backgrounds	74
5.7	Acceptance Calculation	76
5.8	Systematics	78
5.9	Results	80
5.9.1	Cross-section measurement for $Z(\nu\bar{\nu})+\gamma$ process	80
5.9.2	Limits on the ADD model of large extra dimensions	80
5.10	Summary	84

Bibliography	86
Appendices	93
A List of samples used for the analysis	94
A.1 Data Samples	94
A.2 Monte Carlo samples	94
B Selection optimization	97
B.1 Photon P_T^γ and E_T' combined cut optimization	97
B.2 E_T' cut optimization	98
B.3 Jet and track veto optimization	98

List of Figures

1.1	Feynman diagrams for the process $q\bar{q} \rightarrow \gamma G$.	10
2.1	CERN accelerator complex	14
2.2	Total integrated luminosity plotted as a function of time	15
2.3	Layout of the CMS detector	16
2.4	A slice of CMS detector in transverse plane showing particle interactions as they pass through the detector volume.	17
2.5	Bore of the CMS solenoid being inserted within the muon chambers interspersed with the steel yokes at the surface.	18
2.6	Schematic view of the CMS tracker	18
2.7	Material budget in units of radiation length as a function of pseudorapidity η for the different sub-detectors.	19
2.8	CMS ECAL barrel (left) and endcap (right) crystals with their attached photodetectors as APD and a VPT respectively.	20
2.9	Schematic view of the CMS ECAL.	22
2.10	r-z view of the CMS HCAL.	23
2.11	Longitudinal view of the CMS Muon System.	24
3.1	Production cross sections for some benchmark physics processes in pp collisions at $\sqrt{s} = 14\text{TeV}$. Interaction rates corresponding to the nominal luminosity of $10^{34} \text{ cm}^{-2}\text{s}^{-1}$ are shown on the right of the Y-axis [37].	27
3.2	Schematic view of the Level 1 Trigger [26]	28
3.3	DAQ system	29
3.4	An illustration of the a) Hybrid clustering algorithm used in the ECAL barrel region and b) 2 overlapping Multi5x5 clusters.	35
3.5	Various stages of an event generation in a pp collision [51]	37
4.1	a) a pair of APD b) Typical spike energy deposit in the ECAL barrel. RecHit transverse energy: 184 GeV, Rechet reconstructed time: -10.5 ns [53]	39
4.2	Working mechanism of sFGVB	40

4.3	Calculation of E_4/E_1 and E_6/E_2 . E_6/E_2 is calculated as $((E_{4_1}/E_{1_1}) + (E_{4_2}/E_{1_2})) / (E_{1_1} + E_{1_2}) - 1$, where 1 & 2 are the first and second highest energy crystals respectively.	41
4.4	a) $1-E_4/E_1$ b) E_6/E_2 , where the black histogram shows the distribution for all photon objects followed by a red histogram after rejecting photons that pass kWeird and in blue the distribution is plotted after rejecting photons further requiring kDiWeird to be true.	41
4.5	The timing distribution is plotted using data where, no cleaning at HLT is applied(black), topological cleaning (used at HLT) is applied(red) and topological and timing cleaning (used in offline reconstruction) are applied (green).	42
4.6	a) Fraction of spike-induced EG triggers as a function of the number of reconstructed vertices for the 2011B data (triangles) and High pileup runs (squares). The red points represent the spike removal working point used in 2011 and the green points the optimized working point for 2012 [56]. b) Efficiency of the Swiss-cross topological cut as a function of the number of reconstructed vertices for early 2012 data.	43
4.7	2012 Data/MC comparison plot of a) rehit energy b) swiss-cross and c) rehit timing with spikes simulated in MC.	45
4.8	a) Noise increase with the ageing of the detector. c) Pile-up interactions per bunch crossing.	46
4.9	Spike rate (number of in-time spikes with ADC count above 50) plotted as a function of in-time pile up (pile up corresponding to BX0).	47
4.10	The swiss-cross distribution is plotted for spikes and $Z \rightarrow ee$ in left and right respectively for 8 TeV MC sample with 2012C ageing and PU conditions.. In left plot, the distribution is plotted for all the hits with their energy above 10 GeV (gray) and for the hits that are recognized as a spike (matched to an APD digi above an amplitude of 50 ADC counts) in black dotted line. In right plot, all the seeds of the super-clusters above 10 GeV are being considered.	48

4.11	The swiss-cross distributions are plotted for spikes and $Z \rightarrow ee$ in left and right respectively for 14 TeV MC samples. Three different rows here show three different run conditions with $\langle PU \rangle = 70$, integrated lumi = 300fb^{-1} ; $\langle PU \rangle = 140$, integrated lumi = 1000fb^{-1} and $\langle PU \rangle = 140$, integrated lumi = 3000fb^{-1} . For left set of plots, the distribution is plotted for all the hits with their energy above 10 GeV (gray) and for the hits matched to a spike in black dotted line. For Zee samples, all the seeds of the super-clusters above 10 GeV are being considered.	49
4.12	The timing distribution is plotted for 14 TeV MC sample with mean PU = 140 and ageing of 3000fb^{-1} for spikes and $Z \rightarrow ee$ in a) and b) respectively. In left plot, the distribution is plotted for all the hits that get matched to an APD digi with their energy above 10 GeV (gray). In right plot, all the seeds of the super-clusters above 10 GeV are being considered in gray. Black dotted line shows the hits which get flagged by swiss-cross ($1\text{-E4}/\text{E1} > 0.95$).	50
4.13	The η distribution is plotted for 14 TeV MC sample with mean PU = 140 and ageing of 3000fb^{-1} for spikes and $Z \rightarrow ee$ in c) and d) respectively . In left plot, the distribution is plotted for all the hits that get matched to an APD digi with their energy above 10 GeV (gray). In right plot, all the seeds of the super-clusters above 10 GeV are being considered in gray. Black dotted line shows the hits which get flagged by swiss-cross ($1\text{-E4}/\text{E1} > 0.95$).	50
4.14	Efficiency of swiss cross cut ($1\text{-E4}/\text{E1} > 0.95$) is plotted as a function of a) time, b) energy, c) eta and d) pile up in spike samples.	51
4.15	Efficiency of swiss cross cut ($1\text{-E4}/\text{E1} > 0.95$) is plotted as a function of eta in Zee samples.	52
4.16	a) Efficiency of tagging spikes is plotted as a function of swiss cross value in spike samples (spike hits in the full readout region). b) Efficiency of tagging super-clusters is plotted as a function of swiss cross value in Zee samples.	52
4.17	Super-cluster efficiency Vs Spike rejection curves for various values of the Swiss-cross cut for hits in full-readout regions	53
4.18	Efficiency/rejection curves for various values of the Swiss-cross cut, for hits in full-readout regions including the effect of adding a timing for a) Run2012C ageing and PU conditions b) Integrated lumi = 300fb^{-1} , mean PU=70, c) Integrated lumi = 1000fb^{-1} , mean PU=140 and d) Integrated lumi = 3000fb^{-1} , mean PU=140.	54

4.19	Efficiency of the sFGVB algorithm for rejecting spike signals versus acceptance of super-clusters from $Z \rightarrow ee$ events, for a range of ageing and PU conditions and for different threshold values of the transverse energy sum of the rechits in the tower. The conditions simulated are: a) Run2012C ageing and PU conditions; b) integrated lumi = 300fb^{-1} , mean PU=70; c) integrated lumi = 1000fb^{-1} , mean PU=140 and d) integrated lumi = 3000fb^{-1} , mean PU=140.	55
5.1	Tree level Feynman diagrams for the process $q\bar{q} \rightarrow \gamma Z$	57
5.2	Kinematic distributions for the photon at the generator level: (a) photon p_T distribution, (b) photon η distribution. Histograms are normalized to unity.	59
5.3	N-1 distributions for all the isolation variables a) ECAL isolation, b) HCAL isolation, c) Tracker isolation, d) HadronicOverEM and e) $\sigma_{i\eta i\eta}$	63
5.4	An event display for the highest p_T^γ event in 5fb^{-1} of data in a) Cylindrical and b) X-Y view.	65
5.5	Efficiency of single photon trigger a) (HLT_Photon125) and b) (HLT_Photon135)	66
5.6	Invariant mass and fits for tag and probe method applied to data [68]. . . .	67
5.7	Invariant mass and fits for tag and probe method applied on Monte Carlo [68].	67
5.8	a) events selected in numerator (red) and denominator (blue) for the raw fake ratio b) a template distribution for $\sigma_{i\eta i\eta}$ and fits to QCD and true photon components in p_T bin of 160 to 200 GeV. c) True fake ratio ratio as a function of p_T [68].	73
5.9	Timing distribution of photons for a) spikes, b) tagged as beam halo using the HE tagger, c) prompt photons and d) candidate sample with vetoes. [68]	75
5.10	Fit of template shapes to candidate timing distribution, shown in both linear and log scales. The contribution in blue is from beam halo and red corresponds to prompt candidates. A contribution due to anomalous signals would have been purple, but the fitter rejected this hypothesis in the candidate sample. [68]	76
5.11	Photon p_T spectra and E_T' for the Standard Model processes and ADD extra dimensions after the full event selection overlayed with $M_D = 1\text{ TeV}$, $n=3$	77
5.12	Photon p_T and E_T' comparison between Standard Model processes and the data in the region where jet and track vetoes are removed.	78
5.13	Number of vertices for the data and pile up reweighted $Z(\nu\bar{\nu})+\gamma$ sample. .	79
5.14	Shape comparison of Photon p_T spectrum between various MD values . .	81

5.15	95% CL upper limit on the cross section is plotted along with the cross-section for 4 extra dimensions as a function of M_D a) using shape based limit b) using counting limit for all the p_T bins c) using only first p_T bin and d) using only fifth p_T bin.	83
5.16	a) Limits on M_D as a function of n and comparison with LEP and Tevatron results for $\gamma + E'_T$. b) Limits on M_D as a function of n and comparison between shape-based and counting limits within the CMS experiment. . . .	84

List of Tables

1.1	Size of the large extra dimension for $M_D = 1$ TeV	9
1.2	Existing lower bounds on M_D in TeV, from LEP and Tevatron at 95% CL. The Tevatron bounds are from Run II with 1.05 fb^{-1} from $D\bar{O}$ and 2 fb^{-1} from CDF [?].	12
2.1	ECAL parameters	21
3.1	Values of the clustering algorithm parameters	36
4.1	Average spike rates per Minimum Bias event as a function of LHC center-of- mass energy. Spikes are defined as RecHits with 3 GeV and $(1-E4/E1)>0.95$	39
5.1	Total signal cross-sections, in pb, for the signal for different model parame- ters calculated by PYTHIA8 with a lower value on Photon p_T of 130 GeV.	59
5.2	K-factors as a function of M_D and number of extra dimensions n	60
5.3	Integrated luminosity by trigger.	61
5.4	N-1 efficiencies	68
5.5	The difference in the efficiencies between data and Monte Carlo simulation.	69
5.6	Cumulative efficiencies of the background processes after successive analysis cuts and in the last column it shows the total number of events from every background at 5.0 fb^{-1}	70
5.7	Summary of estimated background events and observed candidate events from the data	77
5.8	Calculated $A \times \epsilon_{MC}$ as a function of M_D and n for $\hat{p}_T > 130$ GeV.	77
5.9	Systematic uncertainties on $A \times \epsilon_{MC}$ calculation.	80
5.10	Summary of the parameters needed for cross-section calculation	80
5.11	ADD 95% CL observed(expected) limits on the cross section as a function of M_D and n ($\hat{p}_T > 130$ GeV).	83

5.12 95%CL observed limits on M_D as a function of n, with and without the k-factor applied	84
A.1 List of datasets used in this analysis.	94
A.2 Details of the Monte Carlo samples used for ADD signal.	95
A.3 Details of the simulated samples used for background analysis.	96
B.1 ADD search sensitivity: $P_T^{\gamma} = \cancel{E}_T$ scan.	97
B.2 ADD search sensitivity : \cancel{E}_T scan.	98
B.3 ADD search sensitivity: jet and track veto scan.	99

Introduction

Particle physics forms a sector of physics that explores nature at the fundamental level. It is a study of elementary particles and their interactions. The quest started more than a century ago when the electron was discovered as the first fundamental particle by J. J. Thomson [1]. Atoms were thought to be fundamental until the beginning of the 20th century prior to Rutherford's experiment confirmed that atoms had a sub-structure [2]. The field thrived through the discovery of protons, neutrons [3] forming the nucleus towards the present day knowledge of quarks and other fundamental particles.

The Standard Model (SM) of particle physics [4, 5, 6] is a theoretical framework that elucidates in detail known particles in nature along with their interactions. The recent discovery of the Higgs boson at the Large Hadron Collider (LHC) completes the particle content predicted by the Standard Model. However, there are a few open questions that SM fails to explain. One well known limitation of the SM is that it does not incorporate the gravitational interactions. These observations motivate new physics beyond the SM which form the basis of theories introducing extra-dimensions. In this thesis, a search is performed for large extra-dimensions in events with a monophoton final state using pp collision data collected by the Compact Muon Solenoid (CMS) experiment at the LHC.

This thesis starts with a brief introduction to the SM in chapter 1. The chapter builds up on the theoretical establishment of the SM and its problems, driving an introduction to the Large Extra Dimensional scenario and its corresponding searches. Chapter 2 gives a brief overview of the experimental setup that is chosen to perform the search in the interest of this thesis. It gives a short introduction to the Large Hadron Collider followed by the description of various sub-detectors of the CMS detector with their respective performance. Chapter 3 describes the challenging trigger system used in CMS to accept the physics data compared to a very high input rate of interactions that happen at design luminosity of LHC. It further illustrates the reconstruction techniques designed to measure muons, electrons, photons, jets and missing transverse energy in an event and Monte Carlo simulations. Understanding the photon reconstruction and rejecting fake photons from background events is the key ingredient of the monophoton search addressed in this thesis. Chapter 4 focuses on the detailed study of spurious signals in the electromagnetic calorimeter which can mimic signal events for the monophoton analysis and are potential danger to the collection of physics data at CMS. Finally, Chapter 5 is devoted to the complete analysis for large extra dimensions in the monophoton channel.

In this document, natural units with $\hbar = c = 1$ are used where \hbar ($h/2\pi$, with h as Planck's constant) and c (velocity of light) are two fundamental constants of relativistic quantum mechanics. The space-time coordinate x represents a contra-variant vector $x = x^\mu = (t, \vec{x})$. The corresponding co-variant vector is obtained by : $x_\mu = g_{\mu\nu}x^\nu$ with the

metric tensor $g_{\mu\nu}$ defined as $\text{diag}(1, -1, -1, -1)$ in 3+1 dimensions.

Chapter 1

The Theoretical Perspective

The Standard Model (SM) of particle physics is a very successful model of particles and their interactions, experimentally tested very precisely. Standard model field contains: Matter Fields (Fermion[spin-1/2] + Scalar[spin-0]) and Gauge Fields (photon, W^\pm , Z , gluon [all spin1]) . The origin of masses of W^\pm and Z bosons is explained by a spontaneous symmetry breaking mechanism and assigning the scalar field a non-zero vacuum expectation value (VEV). SM gives a complete description of strong and electroweak interactions, however it fails to unify the gravitational interactions along with them. Various theories have been modelled to address it and corresponding to that various experimental searches have been conducted.

In this chapter, first a brief overview of the Standard Model is presented, alongwith a brief description of the hierarchy problem of the SM. Section 1.2 introduces the model of Large extra dimensions proposed by Arkani Hamed, Dimopoulos and Dvali (ADD) that forms the underlying physics motivation for the subject of this thesis. In the third section, experimental searches that can be performed at the Large Hadron Collider to look for these extra-dimensions are discussed. Finally, the constraints from previous experimental searches have been reviewed.

1.1 Standard Model of Particle Physics

SM is formulated to explain the existence of fundamental particles in nature, their properties and interactions between them. Particle content of SM can be described by fermions: quarks and leptons each in 3 generations (as shown below), where leptons can only interact through electroweak interactions while quarks can interact both through strong and electroweak interactions. There are 4 gauge bosons W^\pm , Z^0 , γ and a scalar higgs boson

which are needed to explain the interactions.

$$\begin{aligned}
\text{Quarks : } & \begin{pmatrix} u \\ d \end{pmatrix}, \quad \begin{pmatrix} c \\ s \end{pmatrix}, \begin{pmatrix} t \\ b \end{pmatrix} \rightarrow \begin{pmatrix} Q = +2/3 \\ Q = -1/3 \end{pmatrix} \\
\text{leptons : } & \begin{pmatrix} \nu_e \\ e \end{pmatrix}, \quad \begin{pmatrix} \nu_\mu \\ \mu \end{pmatrix}, \begin{pmatrix} \nu_\tau \\ \tau \end{pmatrix} \rightarrow \begin{pmatrix} Q = 0 \\ Q = -1 \end{pmatrix} \\
\text{Gauge Bosons : } & W^\pm, Z^0, \gamma, g \\
\text{Scalar : } & H^0
\end{aligned} \tag{1.1}$$

The SM is dictated by a symmetry principle. If a system remains invariant under some particular operation, it is said to be symmetric. In particle physics, this becomes of utmost importance as soon as the concept of symmetry connects to the conservation laws observed in everyday life. In the language of classical field theory, dynamics of any system is understood in terms of the Lagrangian. Thus, if Lagrangian remains invariant under some continuous transformation, then this symmetry leads to a corresponding conservation law. This is known as Noether's theorem [7].

Standard Model builds up on the concept of gauge invariance [8]. A gauge transformation on matter fields is given by a unitary operator :

$$U = e^{i\theta^i Q^i} \tag{1.2}$$

where, Q^i are the generators of the gauge group and θ^i are the parameters of gauge transformation. Here, indices i run over all the generators of the particular group. If the parameters θ^i are dependent on the space-time co-ordinates, it is known as local gauge transformation else its a global gauge transformation. If the transformation,

$$\Psi(x) \rightarrow U\Psi(x) \tag{1.3}$$

where, $\Psi(x)$ is the field content of the system, leaves the Lagrangian invariant, it leads to conserved quantities. This transformation can be thought of as phase rotation of the field. If it is a local gauge transformation, an additional gauge field is needed which can be thought of as the information carrier from one space-time coordinate to another in order to maintain the invariance of the system.

SM is a locally gauge invariant theory, based on the $SU(3)_C \times SU(2)_L \times U(1)_Y$ gauge group. $SU(3)_C$ sector of the gauge group corresponds to the strong interactions characterized by colour charge(C). $SU(2)_L \times U(1)_Y$ sector describes the electroweak interactions where, $SU(2)_L$ corresponds to weak isospin(L) and $U(1)_Y$ corresponds to the

hypercharge(Y). The fermionic part of the Lagrangian [9] is given by:

$$\mathcal{L}_{Fermion} = \bar{\Psi}_f \gamma^\mu (i\partial_\mu - \frac{g_s}{2} G_\mu^a T_f^a - \frac{g}{2} W_\mu^b L_f^b - \frac{g'}{2} B_\mu Y_f) \Psi_f \quad (1.4)$$

Where, Ψ_f represent the fermionic field. G_μ^a ($a = 1, \dots, 8$) represent the gluon fields with g_s as the coupling and T_f^a as the generators to the associated $SU(3)_C$ group. W_μ^b ($b = 1, \dots, 3$) are 3 weak fields with g as the coupling with L_f^b as the generators of $SU(2)_L$ group and B_μ as the field associated to $U(1)_Y$ with Y_f as hypercharge and g' as coupling. Under the local gauge transformation, as pointed out before if :

$$\Psi(x) \rightarrow U\Psi(x), A_\mu \rightarrow U(A_\mu + \partial_\mu)U^{-1}, U = e^{i\theta^i Q^i} \quad (1.5)$$

where, $Q = (T^a, L^b, Y)$ and $A_\mu = G_\mu^a T^a + W_\mu^b L^b + B_\mu Y$, leads to the invariant Lagrangian and hence conserved charges as colour, iso-spin and hypercharge. The kinetic part of the gauge fields is given by :

$$\mathcal{L}_{Gauge} = -\frac{1}{4}(G_{\mu\nu}^a G^{a\mu\nu} + W_{\mu\nu}^b W^{b\mu\nu} + B_{\mu\nu} B^{\mu\nu}) \quad (1.6)$$

with :

$$\begin{aligned} G_{\mu\nu}^a &= (\partial_\mu G_\nu^a - \partial_\nu G_\mu^a) + if^{abc} G_\mu^b G_\nu^c, \\ W_{\mu\nu}^a &= (\partial_\mu W_\nu^a - \partial_\nu W_\mu^a) + i\epsilon^{abc} W_\mu^b W_\nu^c, \\ B_{\mu\nu} &= (\partial_\mu B_\nu - \partial_\nu B_\mu) \end{aligned} \quad (1.7)$$

where, f^{abc} are the structure constants of the $SU(3)$ gauge group and ϵ^{abc} are the structure constants of the $SU(2)$ group. ϵ^{abc} is a completely antisymmetric pseudo-tensor. This formulation does not allow the electroweak gauge fields to be massive since the mass terms like $m^2 B_\mu B^\mu$ are not gauge invariant. However, experimentally three massive gauge bosons have been observed. In the SM, this is explained by adding a complex scalar field in the theory with the Lagrangian as:

$$\mathcal{L}_{Higgs} = \left| \left(i\partial_\mu - g\frac{L_i}{2} W_\mu^i - \frac{g'Y}{2} B_\mu \right) \phi \right|^2 - V(\phi) \quad (1.8)$$

with,

$$V(\phi) = \frac{\mu^2}{2} |\phi|^2 + \frac{\lambda}{4} |\phi|^4 \quad (1.9)$$

where, for $\mu^2 < 0$ and $\lambda > 0$, the potential resembles the shape of a Mexican hat, and the continuous state of minima is given by VEV(vacuum expectation value) as

$|\phi_0|^2 = -\mu^2/\lambda = v^2$. Therefore, as the field acquires a given state of minimum, the $SU(2) \times U(1)$ symmetry of the Lagrangian is broken. This is known as the Electroweak Symmetry Breaking(EWSB) mechanism [10, 11, 12]. The vacuum is invariant under $U(1)_{em}$ transformations with generator

$$Q = L^3 + Y/2 \quad (1.10)$$

leaving photon massless. This $SU(2) \times U(1)$ broken symmetry to $U(1)_Y$ generates the masses of the observed particles, W^\pm, Z^0 as given in equation 1.11. This process is technically achieved by assigning the complex scalar doublet ϕ a non-zero VEV. The complex scalar doublet ϕ has 4 real fields. Three of them are auxiliary fields (termed as ‘‘Goldstone bosons’’ [13]) which can be eliminated or ‘‘gauged’’ away at each point in space time by a suitable choice of local gauge. These corresponding three degrees of freedom in the Lagrangian appears back as the three mass parameters of W^\pm, Z bosons. The unbroken $U(1)_Y$ leads to the massless gauge boson called photons.

$$\begin{aligned} M_W &= \frac{1}{2}gv \\ M_Z &= \frac{M_W}{\cos \theta_W} \\ \rho &= \frac{M_W^2}{M_Z^2 \cos^2 \theta_W} = 1 \end{aligned} \quad (1.11)$$

where, θ_W is the Weinberg angle given by $\frac{g'}{g} = \tan \theta_W$ and the four corresponding gauge fields are :

$$\begin{aligned} W_\mu^\pm &= \frac{1}{\sqrt{2}}(W_\mu^1 \mp W_\mu^2) \\ A_\mu &= \cos \theta_W B_\mu + \sin \theta_W W_\mu^3 \\ Z_\mu &= -\sin \theta_W B_\mu + \cos \theta_W W_\mu^3 \end{aligned} \quad (1.12)$$

A scalar massive field (Higgs field) remains in the theory with its mass as $\sqrt{2\lambda}v$. In the low energy limit when electroweak interaction reduces to 4-Fermi interaction, the value of VEV can be estimated by $v^2 = 1/2\sqrt{G_F}$, with Fermi-constant G_F well known from muon decay gives $v = 246$ GeV.

The interaction of the complex scalar field with the fermions (Yukawa interactions) is sufficient to give mass to the fermions. This part is given by :

$$\mathcal{L}_{Yukawa} = -G_d^{ij} \bar{Q}_{L_i} \phi D_{R_j} - G_u^{ij} \bar{Q}_{L_i} \bar{\phi} U_{R_j} - G_e^{ij} \bar{L}_{L_i} \phi E_{R_j} + h.c. \quad (1.13)$$

where, $G_{d,u,e}^{ij}$ contains the Yukawa coupling giving rise to $M_{u,d,e} = v/\sqrt{2}G_{u,d,e}$. \bar{Q}_{L_i} is the left handed quark doublet, U_{R_j} and D_{R_j} are the right handed singlets of up and down type quarks, L_{L_i} is left handed doublet of leptons and E_{R_j} is the right handed component of charged leptons.

Thus, the complete SM Lagrangian of particle physics is :

$$\mathcal{L}_{SM} = \mathcal{L}_{Fermion} + \mathcal{L}_{Gauge} + \mathcal{L}_{Higgs} + \mathcal{L}_{Yukawa} \quad (1.14)$$

1.1.1 Shortcomings of the Standard Model

Despite having successfully predicted and explained a wide variety of elementary particles and their interactions, there is a clear case to be made for the SM not being the end of the quest for a fundamental theory of particle physics. SM sets a number of open questions in front which can't be explained with the above described theory. The most obvious one to say that SM is not a complete theory is that it does not describe gravitational interactions.

The ratio of gravitational and electromagnetic forces between two protons kept apart at an arbitrary distance r is given by $\sim 10^{-36}$. The apparent weakness of the gravitational forces is not understood yet. In SM, the corresponding lack of understanding appears via fine-tuning or hierarchy problem. When higgs mass receives the radiative corrections via $t\bar{t}$ one-loop correction, it becomes proportional to the cut-off scale of the SM, upto which the theory holds. The new physics scale where gravity becomes strong is given by Planck scale $M_{Pl} \sim 10^{19}$ GeV compared to the electroweak scale of 10^2 GeV leading to a requirement of the cancellation of such large corrections. This is known as fine-tuning problem. The existence of two widely different fundamental length scales of nature is known as the hierarchy problem. This problem can be dealt by two scenarios where in one case, large radiative corrections get cancelled due to the presence of other particles in nature by the extension of the above theory as Supersymmetry (SUSY) and in another case when new physics lies at a much lower scale similar to electroweak scale which form the basis of theories introducing extra-dimensions.

1.2 Introduction to ADD Large Extra Dimensions

In 1998, Arkani Hamed, Dimopoulos and Dvali (ADD) [14] proposed a framework for solving the hierarchy problem. In this framework, the issue is addressed by the considering the possibility that the 4D Planck scale (M_{Pl}) is not the fundamental scale and there may be a much lower scale of gravity that exists if there exists new extra spatial dimensions. The SM particles are confined to the 3+1 dimensional subspace (called as brane) residing

in a higher dimensional space-time while gravity can propagate to much larger volume spanned by the extra dimensions.

Because of the compactification of the extra dimensions, the gravitational field appears as a series of quantized energy states in 4 dimensions, which are referred to as Kaluza-Klein modes [?]. This can be realized if one starts from a simpler problem where a free massless scalar field theory in 4+1 dimensions is considered and the extra spacial dimension is compactified on a circle of length $2\pi R$. The action for this theory is given by :

$$S = \int d^4x dy (\partial_\mu \phi \partial^\mu \phi - \partial_y \phi \partial^y \phi) \quad (1.15)$$

where, x^μ are non-compact directions with $\mu= 0,1,2,3$ as indices in 4D and y is the index for compactified extra dimension. Fourier decomposition of the field ϕ can be written as:

$$\phi(x, y) = \sum_n \phi_n(x^\mu) e^{ik_n y} \quad (1.16)$$

where, $k_n = 2\pi \frac{n}{R}$ similar to simple harmonic oscillator case. Inserting this in equation 1.15, gives

$$S = \int d^4x \sum_n (\partial_\mu \phi_{-n} \partial^\mu \phi_n - k_n^2 \phi_{-n} \phi_n) \quad (1.17)$$

which is equivalent to Klein-Gordon equation with infinite number of modes. This says that a single field in 4+1 dimensions can be thought of as a four dimensional field theory with infinite number of modes, known as Kaluza-Klein modes.

A Kaluza-Klein graviton (G) behaves like a massive, weakly-interacting, stable particle whose direct production gives an imbalance in the final state momentum as its collider signature. In distinction to the electroweak and strong interactions, gravitons do not couple to the charge but to the energy-momentum tensor.

Gauss's law for the gravitational potential in $4+n$ dimensions leads to the form of the potential energy $V(r)$ between two particles of masses m_1 and m_2 separated by a distance r .

$$V(r) \approx \begin{cases} \frac{m_1 m_2}{M_D^{n+2} R^n} \frac{1}{r} & \text{if } r \gg R \\ \frac{m_1 m_2}{M_D^{n+2}} \frac{1}{r^{n+1}} & \text{if } r \ll R \end{cases} \quad (1.18)$$

where, R is the size of the extra dimensions and M_D is fundamental scale of gravity in $4+n$ dimensions. Compared with Newton's law, equation 1.18 gives the observed Planck's

scale in four dimensions :

$$M_{Pl}^2 \approx M_D^{n+2} R^n \quad (1.19)$$

Thus, if M_D is of the same order of magnitude as the electroweak scale (instead of 10^{19} GeV), no fine-tuning of the higgs mass will be required. Equation 1.19 shows that the observed weakness of gravity or equivalently, large value of M_{Pl} in 4D is a consequence of the large size of R and it depends on the number of extra dimensions in the theory. M_D and n are the parameters of the model.

Considering $M_D = 1$ TeV, the size of extra-dimensions is given by:

$$R = 10^{\frac{30}{n}-19} m \quad (1.20)$$

For up to four extra dimensions the values for R are listed in Table 1.1. This shows, for the case of $n = 1$, R is about the scale of astrophysics where nature of the gravitational interactions is well known. In this model, these extra-dimensions are called large compared to the electroweak scale (M_{EWK}^{-1}).

n	1	2	3	4
R[m]	10^{11}	10^{-4}	10^{-9}	10^{-12}

Table 1.1: Size of the large extra dimension for $M_D = 1$ TeV

In the interest of this thesis, large-extra dimensions have been searched with the final states as predicted by ADD model.

However, there is a problem with the solution offered by the ADD model as well. Though the Planck scale (M_{Pl}) has been brought down to the electroweak scale, the hierarchy problem persists and is reformulated through the existence of large volume of extra-dimensions (R^{-1} is very small compared to electroweak scale for $M_D = 1$ TeV). Therefore, more sophisticated extensions were postulated using the idea of extra-dimensions to deal best with this problem. One such important model has been given by Randall-Sundrum (RS) [15], where a “warp” factor is introduced which is a rapidly changing function of an additional dimension.

1.3 Searches for ADD Large Extra Dimensions at Large Hadron Collider

The ADD model predicts a number of observable signatures at the Large Hadron Collider (LHC). One of the direct signatures is the production of a graviton in association with

other particles in proton-proton (pp) collisions. Indirect searches involve virtual graviton production decaying in final states with two leptons, photons, or Z bosons. Gravitons can directly be produced at the LHC via the reactions $gg \rightarrow qG$, $q\bar{q} \rightarrow gG$, $qg \rightarrow qG$ and $q\bar{q} \rightarrow \gamma G$. The cross section for graviton production goes inversely with fundamental Planck scale M_D (the terms that are proportional to M_{Pl} coming from graviton-parton coupling gets cancelled with the increased phase space volume due to the presence of the extra-dimensions $R^n \approx M_{Pl}^2/M_D^{n+2}$). However, the produced graviton doesn't gain from increased phase space, interacts weakly and escapes detection [16]. Therefore, the first three processes will lead to a single high p_T jet and a large missing transverse momentum \cancel{E}_T in the final state while the last process will give \cancel{E}_T and a single high p_T photon in the final state. The Feynman diagrams for the reaction $q\bar{q} \rightarrow \gamma G$ are shown in Figure 1.1. Since the contact interaction is the only one which is not propagator suppressed and grows as s , this will be the dominant contributor to the direct graviton production at the LHC. In this thesis, a search for ADD large extra dimensions is performed in the final state of $\gamma + \cancel{E}_T$ using the CMS detector at LHC.

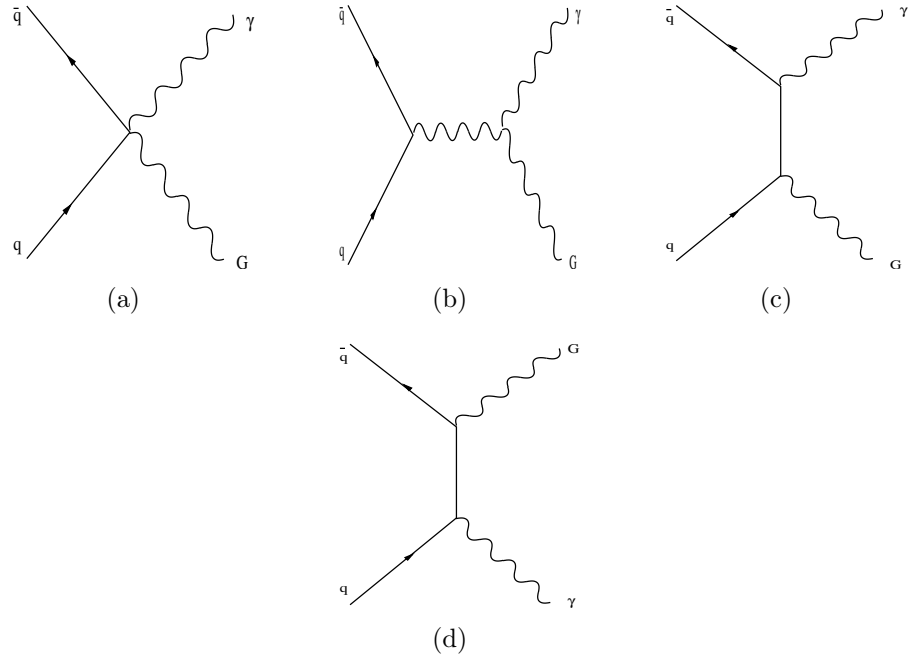


Figure 1.1: Feynman diagrams for the process $q\bar{q} \rightarrow \gamma G$.

In ADD model, the differential cross section [16] for the production of Kaluza-Klein graviton of mass m via $q\bar{q} \rightarrow \gamma G$ is given by :

$$\frac{d\sigma_m}{dt}(q\bar{q} \rightarrow \gamma G) = \frac{\alpha Q^2}{16N} \frac{1}{sM_p^2} F_1(t/s, m^2/s) \quad (1.21)$$

Here, Q is the electric charge of the interacting quarks, $N = 3$, the factor due to the colour charges of the quarks, s and t are the Mandelstam variables, $\alpha = e^2/4\pi$, $\bar{M}_p = M_{pl}/\sqrt{8\pi}$ and F_1 is given by:

$$F_1(x, y) = \frac{1}{x(y-1-x)} [-4x(1+x)(1+2x+2x^2) + y(1+6x+18x^2+16x^3) - 6y^2x(1+2x) + y^3(1+4x)] \quad (1.22)$$

For e^+e^- collider, s is the center of mass energy while for a hadron collider, it refers to $\sqrt{\hat{s}}$, the partonic center of mass energy. It is apparent from the $1/\bar{M}_p^2$ factor in equation 1.21 that graviton is weakly interacting. However, for experimental searches of graviton production, inclusive cross section is studied where the contributions of the different Kaluza-Klein modes have been summed up to compensate the $1/\bar{M}_p^2$ factor in equation 1.21

The inclusive cross-section [16] is given as

$$\frac{d^2\sigma_m}{dt dm} = S_{n-1} \frac{\bar{M}_p^2}{M_D^{2+n}} m^{n-1} \frac{d\sigma_m}{dt}, \quad S_{n-1} = 2\pi^{n/2}/\Gamma(n/2) \quad (1.23)$$

where, S_{n-1} is the surface area of a unit sphere in n dimensions. This is an effective low-energy theory valid when effective centre-of-mass energy in the parton collision $\sqrt{\hat{s}}$ is less than M_D [16]. Therefore, while integrating over all possible values of the partonic center of mass energy, $\sqrt{\hat{s}}$, the integral is taken up to $\hat{s} = M_D^2$. A consequence of this limit, important for this analysis is that the p_T spectrum of the final state photon becomes harder at higher values of M_D .

1.4 Previous Limits on ADD Extra Dimensions

Since its proposal, the ADD model of Large Extra Dimension has been tested at the Tevatron, HERA, the Large Electron Positron (LEP) collider experiments. At both LEP and Tevatron, graviton production has been searched for in the $\gamma + \cancel{E}_T$ channel. LEP experiments have also studied final states with a pair of photons, leptons, W or Z. The best LEP limits on M_D are from the $\gamma + \cancel{E}_T$ channel.

At the Tevatron jet + \cancel{E}_T , diphoton, dilepton (e^+e^- , $\mu^+\mu^-$) and ZZ channels have been studied. Table 1.2 shows the limits reported by LEP and Tevatron experiments in the $\gamma + \cancel{E}_T$ channel as well as the limits obtained by CDF, combining this channel with the jet + \cancel{E}_T channel [17]. Lower limits have been reported from astrophysical observations [18] and from sub-millimeter gravity [19] experiments as well. The most

recent bounds are from the LHC experiments where a search for ADD gravitons has been made in the final states of diphoton ($\gamma\gamma$) [20], dilepton(e^+e^- , $\mu^+\mu^-$) [21], $\gamma + \cancel{E}_T$ [22] and jet + \cancel{E}_T [23], [24].

Source n	LEP $\gamma + \cancel{E}_T$	DØ $\gamma + \cancel{E}_T$	CDF $\gamma + \cancel{E}_T$	CDF jet + \cancel{E}_T	CDF combined
2	1.600	0.921	1.080	1.310	1.400
3	1.200	0.877	1.000	1.080	1.150
4	0.940	0.840	0.970	0.980	1.040
5	0.770	0.821	0.930	0.910	0.980
6	0.660	0.810	0.900	0.880	0.940

Table 1.2: Existing lower bounds on M_D in TeV, from LEP and Tevatron at 95% CL. The Tevatron bounds are from Run II with 1.05 fb^{-1} from DØ and 2 fb^{-1} from CDF [?].

Chapter 2

The Experimental Setup

CERN, European Center for Nuclear Research, is world's largest particle physics laboratory situated in Geneva on the border of Switzerland and France. It hosts a large number of accelerators and experiments including the Large Hadron Collider (LHC). The main goals of the LHC includes understanding of the Electroweak Symmetry Breaking mechanism, search for Supersymmetry, Large Extra Dimensions (LED), search for dark matter candidates and quark-lepton substructure. It hosts two large general purpose detectors, the ATLAS (A Toroidal LHC Apparatus) and the CMS (Compact Muon Solenoid).

With the discovery of Higgs boson, from both the ATLAS and CMS experiments at the LHC this year, with mass ~ 125 GeV responsible for Electroweak Symmetry Breaking, shows that the accelerator and its experiments are capable of accomplishing the physics program which motivated their design. The study presented in this thesis uses data collected at the CMS detector produced by the LHC. This chapter gives an overview of the LHC and CMS experiment.

2.1 LHC

The LHC [25] is the world's highest energy collider. It is designed to collide two counter rotating beams of protons or heavy ions guided by superconducting magnets around the accelerator ring. It is installed in a 26.659 km long tunnel present from the previous CERN experiment, the Large Electron-Positron Collider (LEP).

The CERN accelerator complex is a chain of machines that accelerate particles to increasingly higher energies injecting them finally to the two beam pipes of the LHC (Figure 2.1). The proton source is where it all starts. It is a bottle of hydrogen gas, wherefrom the electrons are stripped off to yield protons. These protons are sent to LINAC where the particles are accelerated upto 50 MeV. Protons reach the Proton Synchrotron Booster (PSB) via 80 m long beamline. PSB is 157 m circumference circular accelerator

and accelerates the energy upto 1.4 GeV. Further, protons are injected in the 628 m circumference circular accelerator Proton Synchrotron (PS) where protons are boosted upto 25 GeV. PS is responsible for the bunch formation with the required bunch spacing at the LHC. These bunches are then sent to the 7 km circumference circular accelerator Super Proton Synchrotron (SPS). Here, protons get accelerated upto 450 GeV. Finally, protons are transferred to the LHC ring, both in clockwise and anti-clockwise direction where the protons are accelerated to higher energies of 3.5 / 4 TeV each. The total time taken starting from the source till the protons are accelerated upto the energy at which they collide in the LHC ring is about 45 minutes.

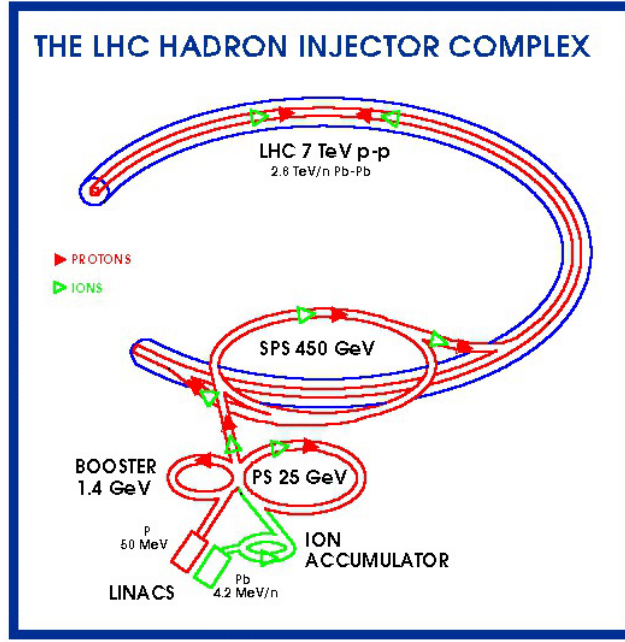


Figure 2.1: CERN accelerator complex

The number of events produced per second in the LHC collisions is given by

$$N = L \times \sigma \quad (2.1)$$

where, σ is the cross section for the particle interaction and L is the machine luminosity.

The amount of data delivered to the detectors is given by the integrated machine luminosity defined as $\int_0^t L dt$, where t is the machine operation time. The luminosity in the LHC is not constant for a given run, but decays with time because of a decrease in the number of protons per bunch due to collisions, beam-gas and beam-beam interactions.

The machine has already completed its phase 1 run and this has been very successful. The bunch separation was 75 ns during the collection of most of the 2010 data and was reduced to 50 ns for 2011 – 2012 data taking. The LHC has reached an instantaneous luminosity of $3.5 \times 10^{33} \text{ cm}^{-2}\text{s}^{-1}$ with about 1.45×10^{11} number of protons per bunch and

1380 proton bunches per beam. It has delivered 44.22 pb^{-1} of data in the year of 2010 and 6.13 fb^{-1} of data during the period 2010 – 2011 at 7 TeV center of mass energy. The center of mass energy was increased in year 2012 to 8 TeV and delivered 23.30 fb^{-1} of integrated luminosity. Figure 2.2 shows the integrated luminosity delivered by the LHC for three years of consecutive run.

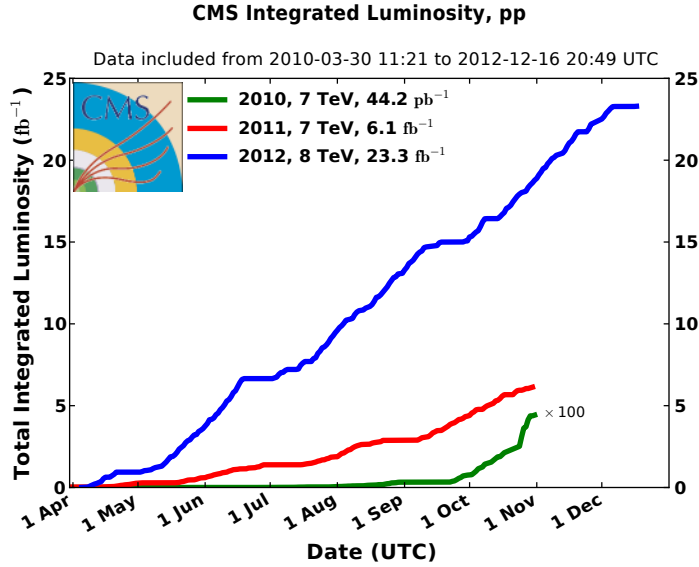


Figure 2.2: Total integrated luminosity plotted as a function of time

2.2 CMS

The Compact Muon Solenoid (CMS) [26] is a multi layered detector installed 100 m under the ground (Figure 2.3). It is 21.6 m in length, 14.6 m in diameter and has a total weight of 12500 tonnes. It is considered compact compared to ATLAS detector which takes up 3 times as much space. The design of the CMS is motivated by the physics goals from re-establishing the Standard Model to explore the new physics regime at TeV scale. Thus, a high performance detector in terms of achieving good resolution of the parameters like energy/momentum of the particle and its good reconstruction efficiency is being aimed at.

A general layout of the CMS detector is shown in Figure 2.3. The main components forming the full CMS detector are the inner tracking system, the electromagnetic calorimeter (ECAL), the hadron calorimeter (HCAL), the superconducting magnet, the muon system and the forward detectors. The components of the detector are arranged into a central barrel region and two endcaps along the beamline to provide as close as the 4π coverage to give best possible measurements for missing transverse energy.

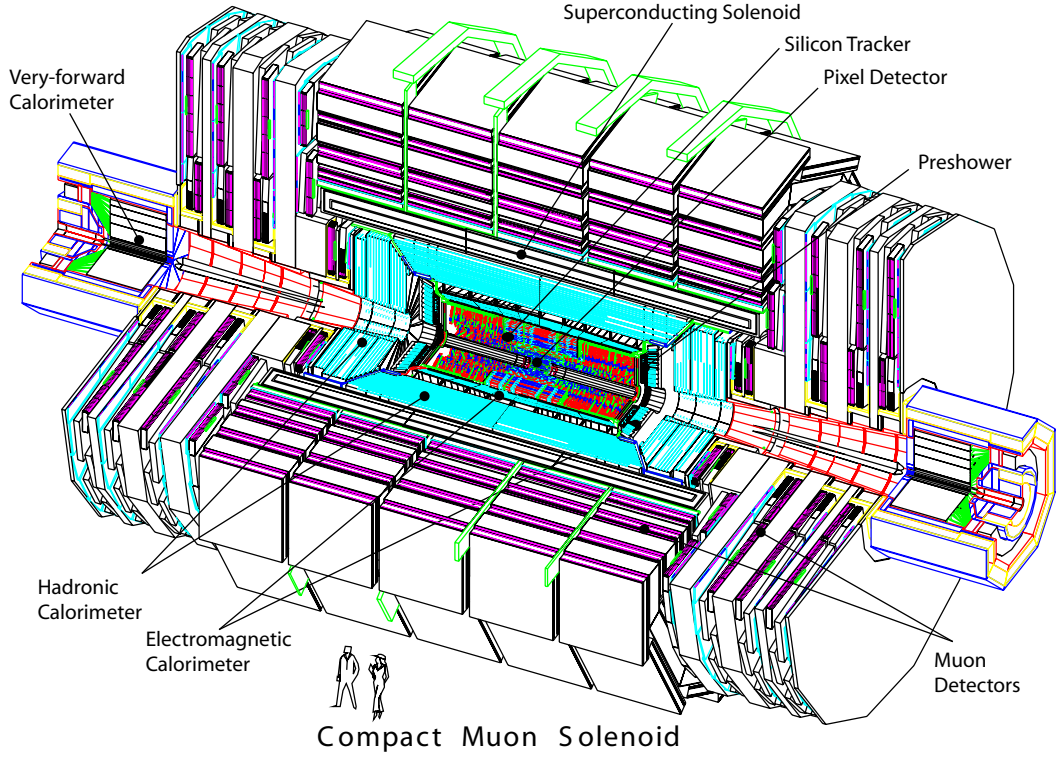


Figure 2.3: Layout of the CMS detector

An important aspect driving the detector design and layout is the choice of the magnetic field configuration for the measurement of the momentum of muons precisely requiring a resolution better than 10% with p_T upto 1 TeV. Large bending power is needed to measure the momentum of high-energy charged particles. Therefore, the central feature of the CMS apparatus is a superconducting solenoid. Inside the bore of the solenoid, the CMS tracker, the electromagnetic calorimeter (ECAL) and the brass+scintillator hadron calorimeter (HCAL) are placed. Any charged particle trajectory is tracked in the tracker. While particles pass through the ECAL and HCA, they deposit their energy in them. Muons are measured in gas-ionization detectors embedded in the return yoke. A slice of the CMS detector is shown in Figure 2.4 in transverse plane with the interaction of particles as they pass through the detector. A detailed description of CMS can be found in reference [26]. In this chapter, the main detector components are reviewed.

CMS uses the right handed coordinate system. It has the origin centered at the nominal collision point, the y-axis pointing vertically upward and the x-axis pointing radially inward toward the center of the LHC. Thus, the z-axis points along the beam in anticlockwise direction. The azimuthal angle ϕ is measured from the x-axis in the x-y plane and the radial coordinate in this plane is denoted by r. The polar angle θ is measured from the z-axis. Pseudorapidity is defined as $\eta = -\ln[\tan(\theta/2)]$. Thus, the momentum

and energy transverse to the beam direction, denoted by p_T and E_T respectively, are computed from the x and y components.

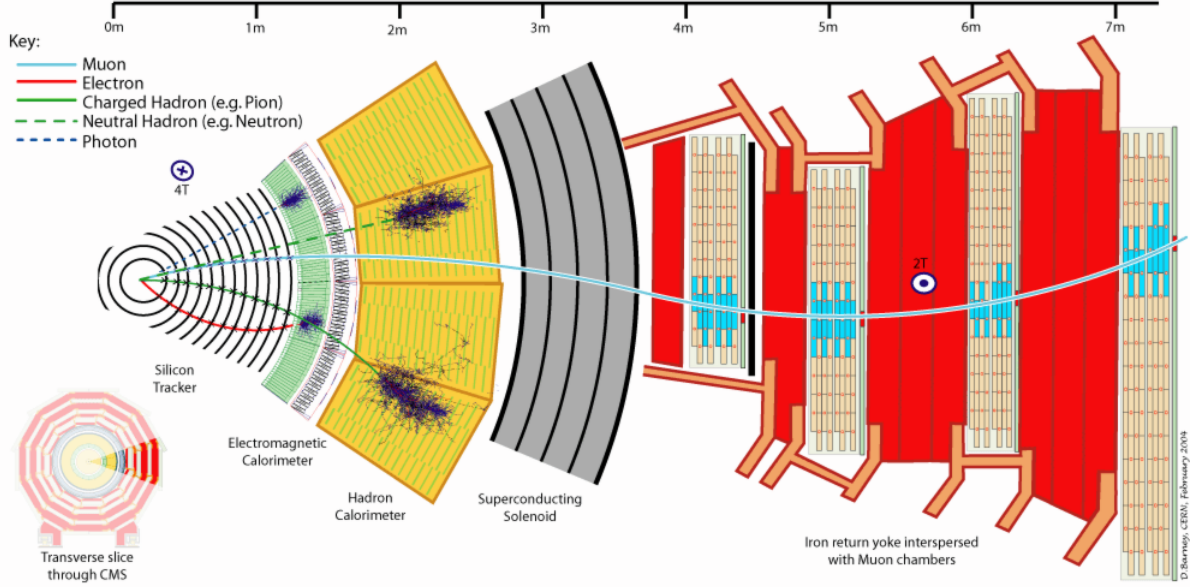


Figure 2.4: A slice of CMS detector in transverse plane showing particle interactions as they pass through the detector volume.

2.2.1 The Superconducting Magnet

The distinctive feature of the CMS is a 4 T superconducting solenoid with a bore of a diameter of 6 m and a length of 12.5 m. The inner coil radius is big enough to accommodate the inner tracker and the complete calorimeter. The magnetic flux is returned by 12,000 tonne steel yoke embedded with the muon chambers. The yoke is composed of five barrel wheels and 2 endcaps, composed of three disks each. Figure 2.5 shows the cross-sectional view of the CMS detector in r - ϕ plane with the solenoid being inserted inside the muon chambers.

2.2.2 The Inner Tracking System

The tracker subsystem (Figure 2.6) consists of silicon pixel and strip layers and is used to reconstruct the trajectories of the charged particles. At the LHC design luminosity of $10^{34} \text{ cm}^2\text{s}^{-1}$, about 1000 particles on average traverse the tracker from more than 20 overlapping proton-proton interactions for each bunch crossing, i.e. every 25 ns. This leads to a hit rate density of 1 MHz/mm² at a radius of 4 cm, falling to 60 kHz/mm² at a radius of 22 cm and 3 kHz/mm² at a radius of 115 cm. In order to keep the occupancy below 1%, 3 regions are defined:



Figure 2.5: Bore of the CMS solenoid being inserted within the muon chambers interspersed with the steel yokes at the surface.

- Closest to the interaction vertex where pixel detectors are placed with size of $100 \times 150 \mu\text{m}^2$ providing an occupancy of $\sim 10^{-4}$ per pixel per bunch crossing.
- Intermediate region ($20 < r < 55 \text{ cm}$), where silicon microstrip detectors are used with minimum strip length of 10 cm and pitch of $80 \mu\text{m}$ giving an occupancy of $\sim 2 - 3\%$ per strip per crossing.
- Outermost region ($r > 55 \text{ cm}$), where larger silicon microstrips are used with a maximum strip length of 25 cm and pitch of $\sim 180 \mu\text{m}$ with occupancy to $\sim 1\%$.

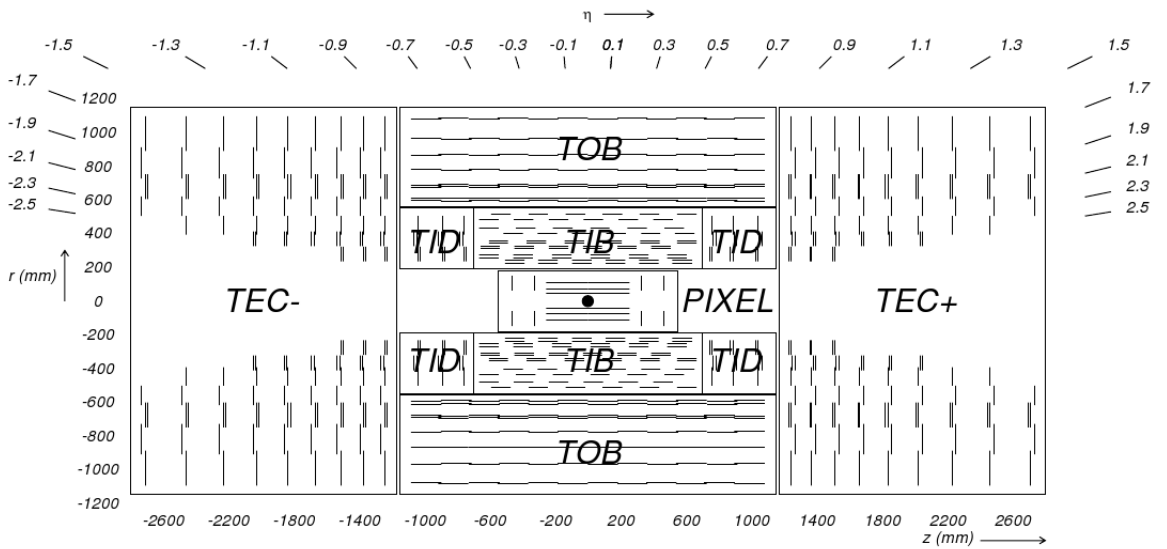


Figure 2.6: Schematic view of the CMS tracker

Three cylindrical layers of pixel detector modules at the radii of 4.4 cm, 7.3 cm and 10.2 cm surround the interaction point in the barrel region with the total length of 53 cm. The 2 end disks extend from 6 to 15 cm in radius and are placed on each side at $|z| = 34.5$ cm and 46.5 cm.

The radial region between 20 cm and 116 cm is covered by silicon strip detector. In barrel, silicon strip tracker is divided into 2 parts with a total of 10 layers: a TIB (Tracker Inner Barrel) and a TOB (Tracker Outer Barrel). The TIB is made of 4 layers and covers up to $|z| < 65$ cm, using silicon sensors with a thickness of $320 \mu\text{m}$ and a strip pitch which varies from 80 to $120 \mu\text{m}$ from layer 1-2 to 3-4. The first 2 layers are made with “stereo” modules with a stereo angle of 100 mrad. This leads to a single-point resolution of 23 - 34 μm in $r\text{-}\phi$ direction and 23 μm in z . The TOB comprises of 6 layers made up of 500 μm thick silicon sensors. In first 4 layers, the strip pitch is 183 μm whereas in last 2 layers, it is 122 μm . This extends upto $|z| < 118$ cm. Here also, first 2 layers are made with “stereo” modules with the same stereo angle as TIB. Here, the single-point resolution varies from 35 - 52 μm in the $r\text{-}\phi$ direction and 52 μm in z .

The tracker endcap region is divided in 2 parts as well: TEC (Tracker End Cap) and TID (Tracker Inner Disks). Each TEC has 9 disks covering the region $120 \text{ cm} < |z| < 280$ cm, and each TID comprises 3 small disks to fill the gap between the TIB and the TEC. Here modules are arranged in rings with their center on the beam axis.

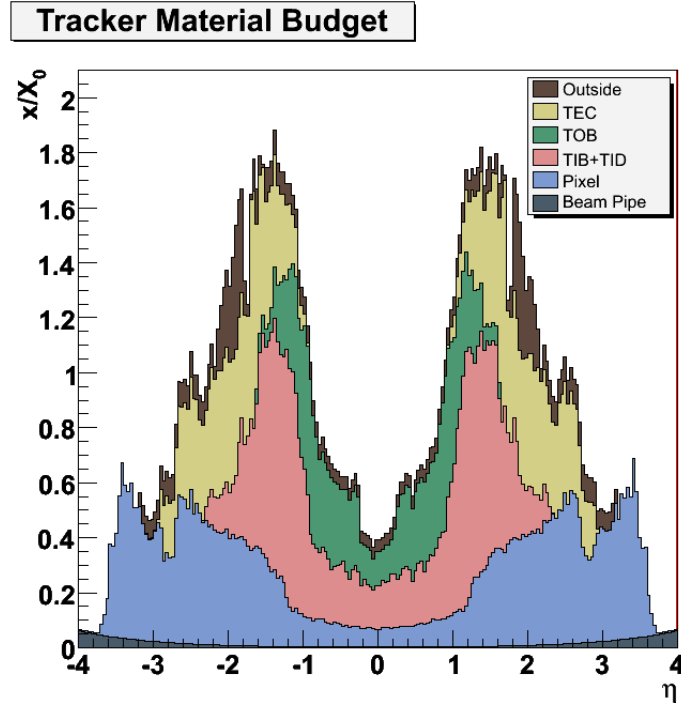


Figure 2.7: Material budget in units of radiation length as a function of pseudorapidity η for the different sub-detectors.

For high p_T (100 GeV) isolated muons, the resolution in the central region is $\sim 2.8\%$ in p_T and $10\ \mu\text{m}$ ($30\ \mu\text{m}$) in transverse (longitudinal) impact parameter [27]. The full tracker gives a coverage of $|\eta| < 2.5$ and have ~ 75 million channels to be readout. The large amount of tracking detectors combined with the electronics, cabling and cooling services leads to a relatively large amount of material in the detector. This degrades the performance of the calorimeter system since particles interact with this material and may undergo radiative effects before reaching the inner surface of the ECAL. The estimated material budget, as a function of pseudorapidity, is shown in Figure 2.7. The estimated total material budget ranges from about 0.4 radiation lengths in the very central barrel, to a peak of about 1.8 radiation lengths near the barrel-endcap transition region.

2.2.3 The Electromagnetic Calorimeter

The electromagnetic calorimeter (ECAL) [28] is located outside the CMS tracker. It is a homogeneous sub-detector layer made up of lead tungstate (PbWO_4) crystals (Figure 2.8) where the electrons and photons deposit all their energies. When an electron or a photon enters the crystal, they produce a shower initiated by bremsstrahlung or pair production to e^+/e^- . This shower produces scintillation photons which are collected by the photo-detectors connected at the back of each crystal. The amount of energy deposited by the particle is estimated using this scintillation signal from the crystals. In the barrel part, Avalanche Photo Diodes (APD) are used while in endcap, Vacuum Photo-Triodes (VPT) are used as the photo-detectors because of high radiation in endcaps.

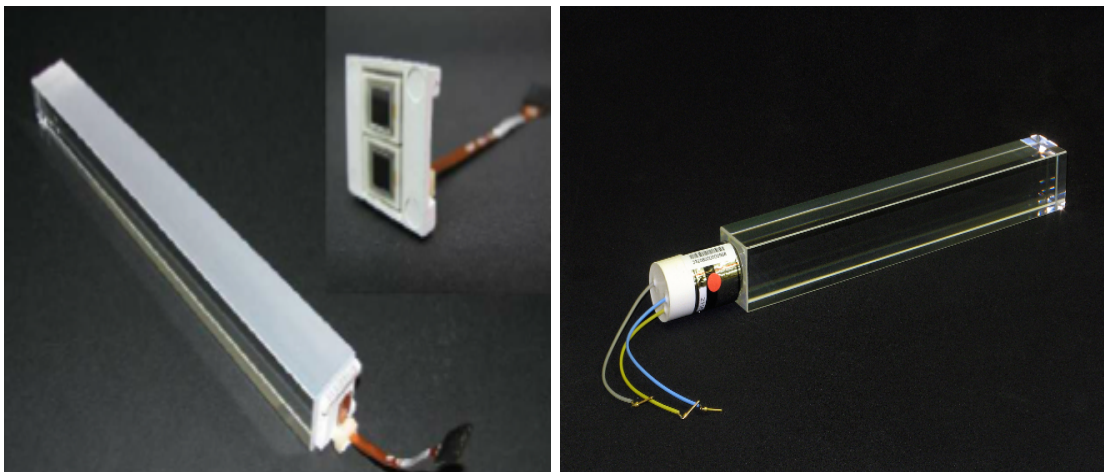


Figure 2.8: CMS ECAL barrel (left) and endcap (right) crystals with their attached photodetectors as APD and a VPT respectively.

Table 2.1 summarizes the design parameters for both ECAL barrel and endcap geometry. ECAL (Figure 2.9) has a total of 82728 crystals including both barrel and endcap

region. In the ECAL Barrel (EB), these crystals are mounted in a way so that they are off-pointing with respect to the center of the detector. Crystals are tilted by a small angle (3°) in both η and ϕ direction. Crystals are grouped to form supermodules covering half of the barrel along the eta direction and 20° in phi direction. Thus, EB is arranged in a total of 36 (2×18) supermodules. Each supermodule has a granularity of 20-fold in ϕ and 85-fold in η . Further, each supermodule is divided in 4 modules along the eta direction. First module is 25 crystals in η and 20 crystals in ϕ respectively, while remaining 3 modules are 20×20 crystals. Crystals are first ensembled in submodules of 2 in $\phi \times 5$ (or 4) in η crystals to be assembled in modules comprising a supermodule.

Parameters	Barrel	Endcaps
Pseudorapidity coverage	$ \eta < 1.48$	$1.48 < \eta < 3.0$
ECAL envelope: r_{inner}, r_{outer} [mm]	1238, 1750	316, 1711
ECAL envelope: z_{inner}, z_{outer} [mm]	$0, \pm 3045$	$\pm 3170, \pm 3900$
Granularity: $\Delta\eta \times \Delta\phi$	0.0175×0.0175	0.0175×0.0175 to 0.05×0.05
Crystal dimension [mm ³]	$21.8 \times 21.8 \times 230$	$24.7 \times 24.7 \times 220$
Depth in Radiation length	25.8	24.7

Table 2.1: ECAL parameters

The mechanical design of the endcap calorimeter has 4 Dees to form 2 endcap disks at each side. Here, crystals are grouped together into units of 36, referred to as supercrystals. A total of 268 identical supercrystals cover each endcap with extra 64 supercrystals to complete the inner and other perimeter. The ECAL is complemented by a preshower (ES) detector in the endcap region ($1.65 < |\eta| < 2.6$) to provide better spatial resolution of the impact point and is used to discriminate a photon from two photons coming from a π^0 decay.

ECAL readout is performed in steps. As mentioned already, at first the crystal converts the energy to light, which is collected by the photo-detector. Photodetectors convert light to current. The low light yield of crystal compels the requirement of the preamplifiers. These preamplifies have a pulse shaping time of 40 ns and convert the current to a voltage waveform. This preamplified signal is digitized in 10 time samples of 25 ns by a floating-point analog-to-digital converter (ADC) which is then transferred to the off-detector electronics via optical fibers.

ECAL energy resolution is parametrized as :

$$\left(\frac{\sigma}{E}\right)^2 = \left(\frac{S}{\sqrt{E}}\right)^2 + \left(\frac{N}{E}\right)^2 + C^2 \quad (2.2)$$

where, S is the stochastic term, N the noise term and C the constant term. The stochastic term includes the fluctuations in lateral shower containment and number of

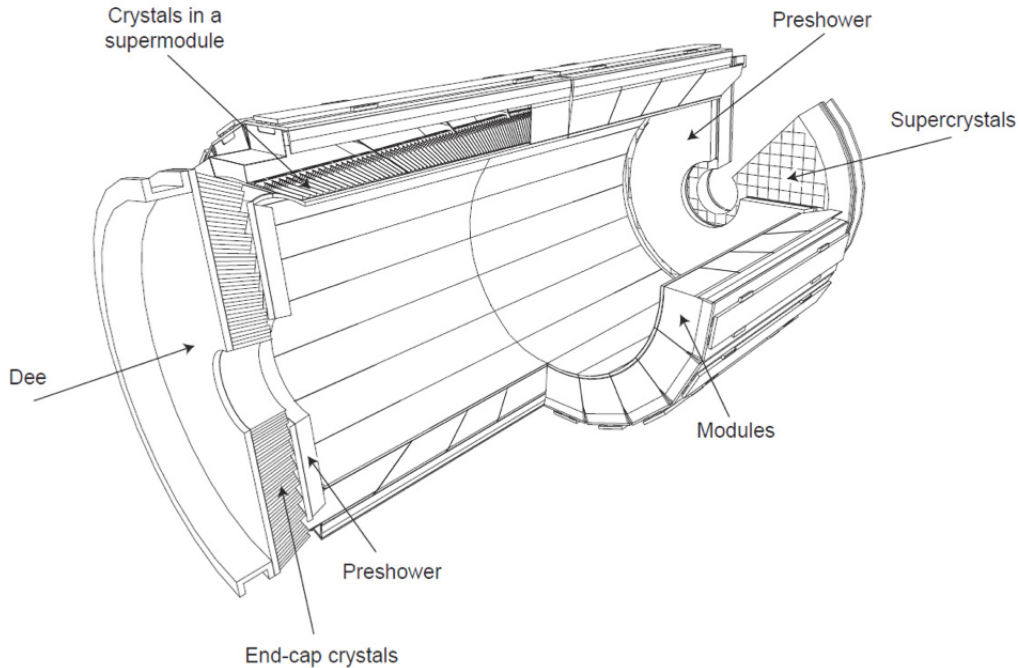


Figure 2.9: Schematic view of the CMS ECAL.

primary photoelectrons produced in the photodetector per GeV. The constant term includes the effects coming from longitudinal light collection, intercalibration errors and leakage of energy from the back of the crystal. The noise term contains the contributions from electronics noise and pile-up noise. Using electrons with test beams, the corresponding contributions are found to be $S = 2.8\%$, $N = 12\%$ and $C = 0.3\%$ [29]. The energy resolution (σ_E/E) measured for electrons and photons is $\sim 1 - 5\%$ [30], [31] depending on barrel or endcap region of the ECAL. and the energy deposited in the preshower absorber

2.2.4 The Hadron Calorimeter

The Hadron Calorimeter (HCAL) is a sampling calorimeter using brass as its absorber plates and plastic scintillator tiles located inside the magnet surrounding the ECAL. The innermost and outermost absorber layers are made of stainless steel for structural strength. There are 17 active plastic scintillator tiles in the barrel and 18 layers in the endcap placed between the stainless steel and brass absorber plates. Particles leaving the ECAL first see a scintillator plate with a thickness of 9 mm rather than 3.7 mm for the other plates. The deposited energy is converted in scintillation photons which are measured in hybrid photodiodes (HPDs) via wavelength-shifting (WLS) fibers embedded within the scintillator tiles. HCAL is used to measure the energy of hadrons and missing transverse energy. It needs a good hermetic coverage for the measure of missing transverse

energy which is one of the most important parameter in this analysis to be looked at.

HCAL is divided in 4 parts as HCAL Barrel (HB), HCAL Endcap (HE), HCAL Outer (HO) and HCAL Forward (HF). Figure 2.10 shows the r-z view of the CMS HCAL. HCAL provides an interaction length that varies between 7-11 λ_I (10-15 λ_I with HO) depending on the η . ECAL in front of HB adds ~ 1 interaction length of material.

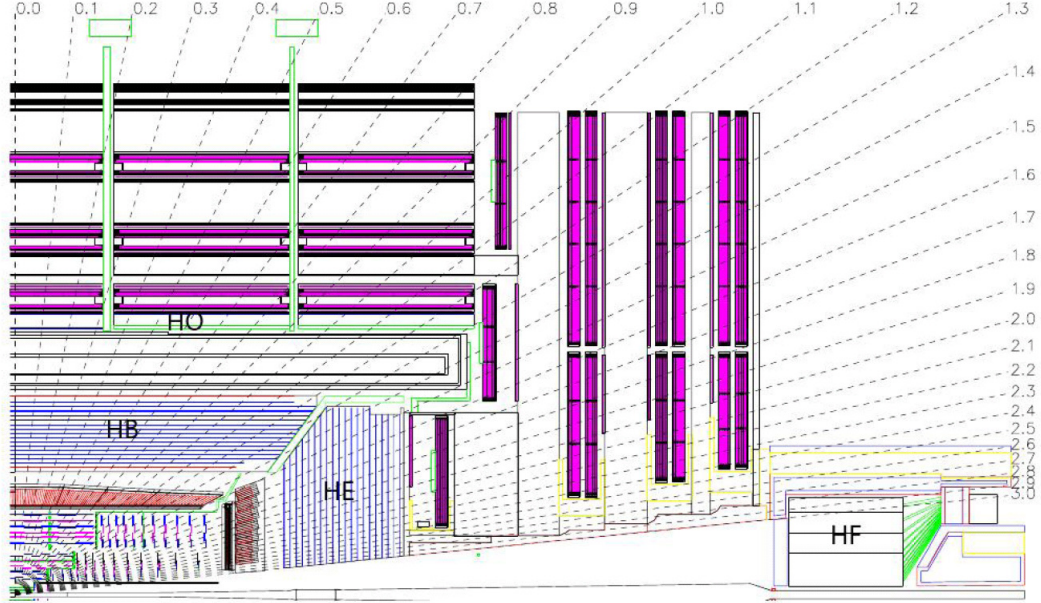


Figure 2.10: r-z view of the CMS HCAL.

The Hadron Barrel (HB) part of HCAL consists of 32 towers along η covering the pseudorapidity region $1.4 < \eta < 1.4$ with a granularity of $\Delta\eta \times \Delta\phi = 0.087 \times 0.087$. The HB consists of 2 half barrels each with 18 identical 20° azimuthal wedges, similar to ECAL. Thus HB has a total of 2592 towers.

HCAL is extended with an additional layer of calorimeter HO beyond the solenoid, physically located inside the barrel muon system to take care of the showers that are produced late in the detector covering an eta range of $|\eta| < 1.26$. It uses solenoid as the absorber and has plastic scintillator at a radial distance of 4.097 m. An additional iron block of thickness ~ 18 cm known as “tail catcher”, is present in the central barrel wheel to take care of the showers that are produced late in the detector. Thus, in this wheel extra scintillation layer is used at a radial distances of 3.850 m.

Hadron Endcap (HE) of HCAL covers the pseudorapidity region $1.3 < |\eta| < 3.0$. HE is composed entirely of brass absorber plates in an 18-fold ϕ -geometry matching that of the barrel calorimeter. There are 18 active plastic scintillator layers in HE. HE tower has a segmentation of 5° in ϕ and 0.087 in η . This granularity increases in η with increase in η while remain 10° in ϕ .

Since in the forward region ($3.0 < |\eta| < 5.2$), rate of energy flow is much higher, the

forward calorimeter (HF) is made up of quartz fibers due to their radiation hardness as the active medium and steel absorbers. It is placed at 11.2 m from the interaction point. HF tower has a increasing granularity from 0.111 to 0.302 in η and 10° to 20° in ϕ . HCAL is read in 1 depth in HB except near the transition region from HB to HE where it is read in 2 depths. At the transition region between HE and HF, HE is read in 3 depths, however HF is read in 2 depths always.

Energies of jets are reconstructed with lower resolutions of $\sigma_E/E \sim 10-15\%$. Missing Transverse Energy (\cancel{E}_T) resolution gets dominated by this in events where hadronic activity gets reconstructed [32], [33].

2.2.5 The Muon System

The CMS muon detection system [34] is shown in longitudinal view in Figure 2.11. It is designed to provide an identification of muon, its momentum measurement and triggering. CMS uses three different gaseous detectors to detect the muons; drift tubes (DT) in the barrel region, cathode strip chambers (CSC) in the endcap region, and resistive plate chambers (RPC) in both the barrel and endcap. The choice is driven by large surface to be covered and different radiation environments. The barrel DTs cover roughly from $\eta=0$ to $|\eta|=1.3$ while the endcap CSCs cover from $|\eta|=0.9$ to $|\eta|=2.4$. The RPCs cover the region from $\eta = 0$ to $|\eta| = 2.1$.

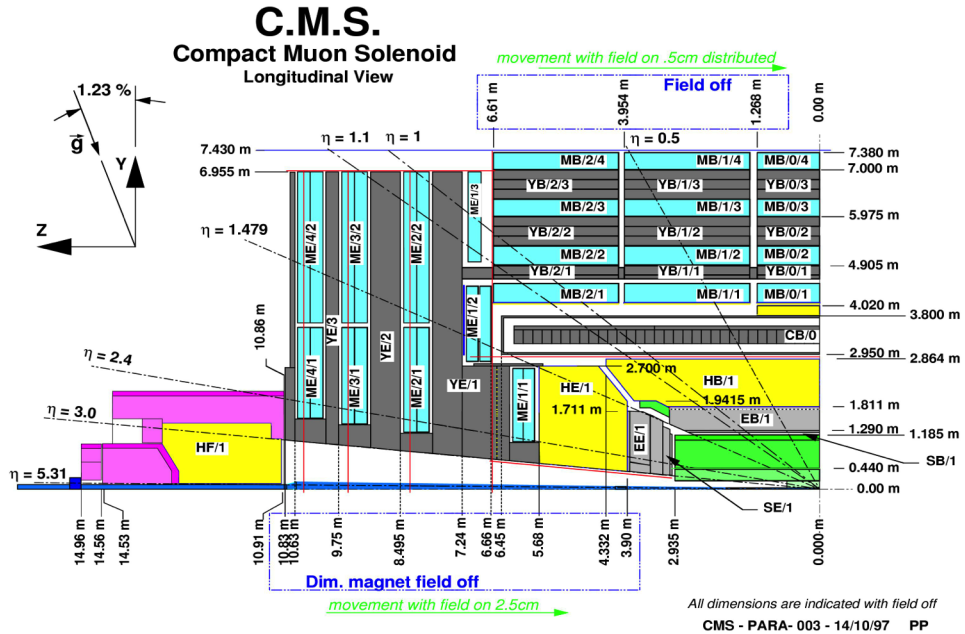


Figure 2.11: Longitudinal view of the CMS Muon System.

The barrel muon system consists of four stations integrated in the return yoke, referred to as MB1, MB2, MB3, MB4. The whole system is assembled in 5 wheels perpendicular

to the beam axis, each 2.5 long. These wheels are labelled from YB-2 for the furthest wheel in -z to YB+2 for the furthest is +z. Each wheel is divided into 12 sectors, each covering a 30° in ϕ . Each sector contains one DT chamber except the 4th station, where top and bottom sectors host 2 chambers each, thus leading to a total of 14 chambers per wheel in the outermost station. The basic unit of the chambers is a drift cell with ~ 400 ns maximum drift time. Each chamber has 12 planes of DT grouped in 3 superlayers(SL) with 4 planes of parallel wires per SL. 2 SLs(1 and 3) provide the measurement in r - ϕ while SL2 in r - z with a single point resolution of $\sim 100\mu\text{m}$. In MB1 and MB2, a DT chamber is coupled with 2 RPC while for the outermost 2 stations, one RPC is placed in the innermost side of the station.

Muon Endcap system has 4 stations (ME1, ME2, ME3, ME4) of CSCs. In each of the endcaps, the CSCs and RPCs are arranged in these 4 stations (or disks) perpendicular to the beam-axis in concentric rings, 3 rings in the innermost station, and 2 in the others. These are represented by MEn/i, where n is a particular station with its corresponding ring. There are 36 chambers in each ring of a muon station, except for the innermost ring of the second through fourth disks (ME2/1, ME3/1, and ME4/1) where there are 18 chambers. CSCs are multiwire proportional chambers and trapezoidal in shape. Each CSC consists of 6 gas gaps sandwiched with cathode strips and anode wires to measure the ionization. The single point resolution is $\sim 200\mu\text{m}$ ($100\mu\text{m}$ for ME1/1) with angular resolution of order 10 mrad in ϕ . There are 36 chambers mounted in each of 2 rings in each of the endcap stations. No RPC's are placed in the innermost ring in the first station and thus providing the eta coverage till $|\eta| < 1.6$. RPCs are double gas gap parallel plate chambers, operated in avalanche mode. In addition to the momentum measurement of the muon, RPCs assigns the bunch crossing to the candidate track. Its timing resolution less than 25 ns and thus makes it very useful for triggering.

The transverse momentum resolution varies from 1% to 6% depending on pseudorapidity for muons with p_T below 100 GeV and is better than 10% in the central region with p_T upto 1 TeV.

Chapter 3

The Data Handling & Event Reconstruction

At the designed luminosity of the LHC, two proton bunches cross each other at a frequency of 40 MHz. One of the biggest challenges at LHC is to select interesting physics events through the CMS Trigger and Data Acquisition (DAQ) system. Once the interesting event is accepted, the offline event reconstruction process progresses in various steps. This involves the reconstruction of the tracks, vertex and all the physics objects (electrons, photons, muons, jets and missing transverse energy as E_T^{miss}) within the event. Various algorithms are run to get the energy-momentum and position measurement of the particles using the digitized signals from the outcome of all the electronic channels coming from all the subsystems of the detector. These particles are used as input for any physics analysis. To understand the detector response, one simulates the data using Monte Carlo (MC) generators, GEANT4 [35] and the response of the readouts from the detector.

In this chapter, first section gives an introduction to the CMS Trigger and DAQ system. The second section briefs the reconstruction approach for the tracks, primary vertex and the physics objects. In the third section, the photon reconstruction is discussed in detail. The final section briefly discusses the Monte Carlo (MC) simulation.

3.1 The Trigger System

The CMS Trigger and Data Acquisition System (TriDAS) [36], [37], faces the detector information at the full crossing frequency of 40 MHz. At the luminosity of $10^{34} \text{ cm}^{-2}\text{s}^{-1}$ at the LHC, each crossing results in an average of ~ 20 inelastic pp events leading to about 1 MB of data. This corresponds to approximately 40 TB of data per second. This high data rate poses two challenges :

- Transferring 40 TB/s over a fast network.

- Writing this data on the storage.

However, the storage capability is limited to the $O(100)$ Hz at the data rates of $O(100)$ MB/s. Therefore, algorithms are needed to reduce the data volume online. This is achieved via Trigger and Data Acquisition System in CMS. The CMS Trigger system is divided in 2 levels, Level-1 (L1) and High Level Triggers (HLT) discussed in sub-sections 3.1.1 and 3.1.2 respectively.

Figure 3.1 shows the cross section for some of the important physics processes. The production of Higgs boson or SUSY processes which are one of important key searches at LHC are more than 9 orders of magnitude down compared to the inelastic pp cross section. Thus, the rate reduction that is done by the CMS Trigger system represents the selection of interesting physics events.

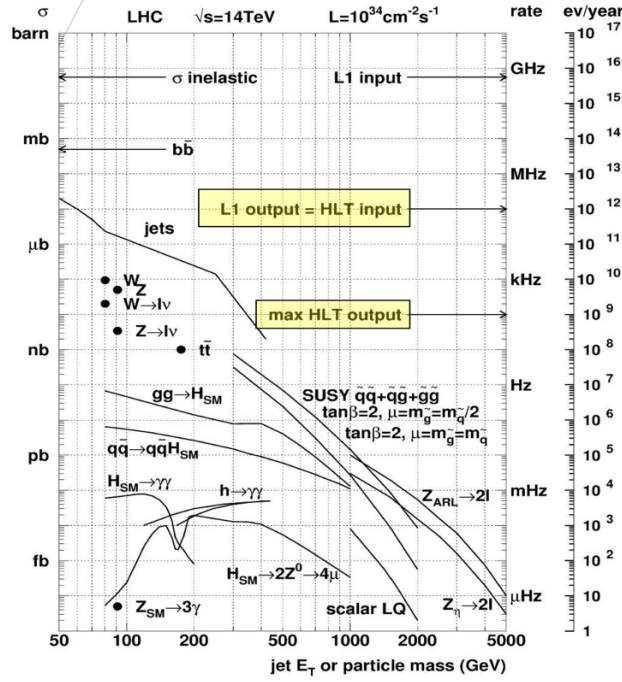


Figure 3.1: Production cross sections for some benchmark physics processes in pp collisions at $\sqrt{s} = 14 \text{ TeV}$. Interaction rates corresponding to the nominal luminosity of $10^{34} \text{ cm}^{-2} \text{ s}^{-1}$ are shown on the right of the Y-axis [37].

3.1.1 Level-1 Trigger System

L1 Trigger system is implemented using custom designed programmable electronics. Level-1 Trigger receives full event rate at the LHC and is able to process them fast. The capability of L1 trigger is limited by the Front End (FE) electronics to store the information coming from all the subdetectors. FE electronics is designed to store 128

bunches($\sim 3.2 \mu\text{s}$) in pipeline, process them and provide the decision for the approval of an event. It uses coarsely segmented data from the calorimeters and the muon system. The decision taking occurs every 25 ns and the event is passed on for further processing such that every 25 ns a new event can enter the buffer. L1 is designed to provide the output event rate at 100 kHz.

Working scheme of L1 Trigger is illustrated in Figure 3.2. The L1 Trigger has local, regional and global components. At the bottom end, the Local Triggers, also called as Trigger Primitive Generators (TPG), are based on energy deposits in calorimeter trigger towers and track segments or hit patterns in muon chambers, respectively. These make up the first or local step of the Calorimeter or Muon Trigger pipeline. Regional Triggers combine their information and use pattern logic to determine ranked and sorted trigger objects such as electron or muon candidates in limited spatial regions. The rank is determined as a function of energy or momentum and quality of the L1 trigger objects. The Global Calorimeter and Global Muon Triggers determine the highest-rank calorimeter and muon objects across the entire experiment and transfer them to the Global Trigger. The latter takes the decision to reject an event or to accept it for further evaluation by the HLT. The decision is based on algorithm calculations and on the readiness of the sub-detectors and the DAQ, which is determined by the Trigger Control System (TCS). The Level-1 Accept (L1A) decision is communicated to the sub-detectors through the Timing, Trigger and Control (TTC) system.

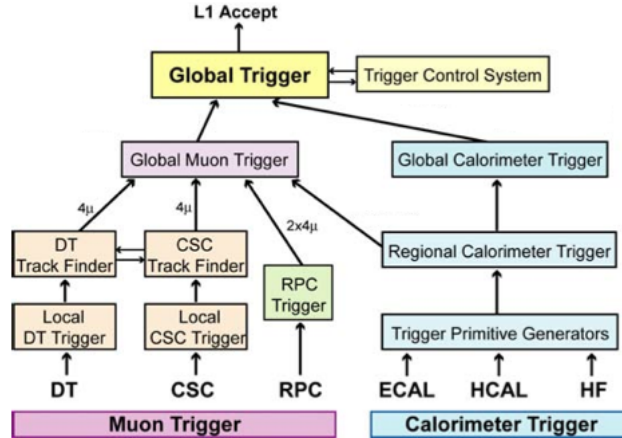


Figure 3.2: Schematic view of the Level 1 Trigger [26]

3.1.2 Data Acquisition System and High Level Trigger

The DAQ is responsible for the readout of the detector and for the collection of all data fragments recorded during a bunch crossing into one single event and make it available to the HLT. Unlike L1, the HLT is fully software based and runs on a processor farm to

decide whether to keep the event or not. The design of the CMS TriDAS system is shown schematically in Figure 3.3.

Upon a L1 Accept (L1A) signal, the Front End Drivers (FEDs) extract the data from the frontend buffers located on the detector. The data from the ~ 600 FEDs are read into ~ 500 Front-end Read-out Links (FRLs) that are able to merge data from two FEDs and generate event fragments with an average size of ~ 2 kB. The sub-detector read-out and FRL electronics are located in the underground electronics room (USC). With 100 KHz as the input from L1, this provides an input data flow at the rate of up to ~ 100 GB/s ($100 \text{ KHz} \cdot 1 \text{ MB}$) to the building unit of DAQ system.

The event builder consists of two stages: the FED-builder and the Readout Unit (RU) builder. The task of FED-builder is to transport the event fragments to the surface building (SCX) and assemble them into 72 super-fragments. A RU-builder is made up of a number of Readout Units (RU), Builder Units (BU) and a single Event Manager (EVM) connected together via builder network. The super-fragments are stored in RUs until a request for this data is made to be transmitted to the Builder Units (BU). The Event Manager (EVM) manages the flow of data and contains the status of all the events in the RU-builder at any point in time. After storage in the RU memory, the event super-fragment is assigned a temporary Event Identifier (Event ID), which remains valid as long as the event is being processed by the event builder (and filter farm). The primary function of the BU is to build complete event from the event super-fragments residing in different RUs. A secondary function is to buffer these events until they are processed by the filter farm.

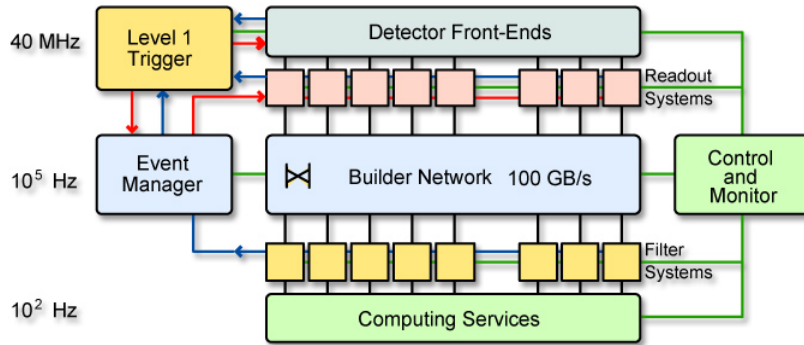


Figure 3.3: DAQ system

Filter Systems execute the HLT algorithms to select the events to be kept for offline processing. HLT provides the selection of 1 : 1000 from the maximum average L1 output rate of 100 kHz to 100 Hz for the final storage purposes. HLT is implemented in 3 steps as Level-2, Level-2.5 and Level-3. Level-2 trigger refers to the first step inside the HLT algorithm. It gets the maximum input rate of events and uses information from only

the calorimeter and muon detectors. The second Level-2.5 trigger uses partial tracker information, e.g. demanding pixel hits for a fast confirmation of the electron candidate by matching it to the super-clusters (discussed in Section 3.3.1) formed in the calorimeters. In the final step, “Level-3”, selection is based on the reconstruction of full tracks in the tracker and the rate is controlled via various calorimetric isolation requirements. To minimize the CPU usage required by the HLT, the algorithms reconstruct the regional information in the CMS detector based on the L1 seeded trigger objects.

Control and Monitor System is responsible for the configuration, control and monitoring of all the DAQ elements. The Computing services include a host of monitoring services, storage and the interface of the DAQ to the “offline” environment, where physicists perform data analyses.

3.2 Event Reconstruction

The offline reconstruction process is carried out in two steps after the event is accepted by the HLT algorithm. First a local reconstruction is performed separately for the various subdetectors under the form of charged-particle tracks using the CMS Tracker, calorimetric clusters from the ECAL and HCAL and muon tracks from the muon chambers. In the second step, global reconstruction combines the information from all the subdetectors “globally” to provide the information of various particles (like $e^-s/\gamma s$) or physics objects like jets or \cancel{E}_T to be used for the analysis purposes. In the following sub-sections, the reconstruction algorithms are briefly outlined for tracks, vertices using the tracker and other physics objects used in this analysis.

3.2.1 Tracks & Vertex reconstruction

In the dense environment at LHC, many charged particles within a single bunch crossing pass through different layers in the tracker. The track reconstruction mainly relies on the fact that the magnetic field is nearly constant in a large part of the tracker which allows the tracks to be described using a helix model. A measurement of the curvature of the track in the given magnetic field gives a determination of the transverse momentum of the particle that passed through.

Starting from the reconstructed hits from the pixel or strip detector layers, the track reconstruction follows in 4 steps [38], [39], [40]. In the first stage, pairs or triplets of hits compatible with the interaction region above a p_T threshold are taken as seeds from the pixel tracker. In the higher eta range, $2 < |\eta| < 2.5$ combination of hits from the pixel and inner layers of the strips are taken. The second stage, track finding (or pattern recognition), called as combinatorial track finder (CTF) at the CMS is based

on a combinatorial Kalman Filter approach. Starting from the seed layer, the track trajectory is extrapolated to the successive tracker layers one by one and compatible hits are assigned to the track. At each succession towards the new layer, the track parameters are updated with the new hit assigned to it allowing for a missing hit from the current layer. The possible ambiguities with tracks sharing several hits are resolved in favour of the track having the larger fraction of the hits that are shared between the two trajectories. The final estimate for the parameters of track trajectory is completed by applying a least-squares fit in two stages - a “forward” fit proceeding inside-out from the interaction region and a “backward” fit in the opposite direction yielding best estimate of the track parameters.

Tracks are reconstructed in multiple iterations using the iterative tracking. After each iteration, hits associated with tracks already found are removed, reducing the combinatorial complexity and thus allowing to search for lower p_T or highly displaced tracks. For 2011 data reconstruction, the iterative tracking consisted of 6 iterations. For $t\bar{t}$ events under 2011 pileup conditions, the track reconstruction efficiency for all charged particles with $p_T \geq 900$ MeV is greater than 95% in the central region of the detector [27].

Once the tracks are reconstructed for a given bunch crossing, these are used for the reconstruction of the vertices. Vertex reconstruction is done in 2 steps, vertex finding and vertex fitting. In vertex finding, the tracks are clustered in several vertex candidates based on the z-coordinate of the track at the point of closest approach to the beam axis (called as the impact point), number of hits and the quality of fit for the given track. However, in the vertex fitting, a fit [41] is performed with the given set of tracks for each vertex candidate determining the vertex parameters. The vertex resolution achieved is $10 - 12 \mu\text{m}$ in all the three directions (x,y,z) [27].

3.2.2 Electrons

Since electron is a charged particle, it leaves a track in the Tracker and deposits its energy in the ECAL. Therefore, the reconstruction algorithm for an electron involves the combination of information from these two sub-systems. Electron is composed of a single track emerging from the interaction vertex and matched to an electromagnetic super-cluster (Section 3.3.1) in the ECAL. The building of electron objects is initiated by the presence of electromagnetic super-clusters followed by matching of 2 pixel hits (pixel seed) in the Tracker. Then, electron tracks are built from these pixel seed [38], [42].

The efficiency of pixel-seed matching is measured to be $99.4 \pm 0.25\%$ in $W\gamma$ and $Z\gamma$ events [43]. The inefficiency of pixel seeds matching to super-clusters is important to this study since photon uses the information of these super-clusters. Hence, if the associated track is not found with the super-cluster corresponding to an electron, it fakes a photon

object.

3.2.3 Muons

A Muon passes through entire length of the detector, leaving behind its track in the tracker and gives signals in the muon chambers. Using the information from the tracker as well as muon chambers, muon tracks are reconstructed independently in the inner tracker as tracker tracks and in the muon system as standalone-muon tracks. Based on that two reconstruction approaches are designed as Global Muon reconstruction and Tracker Muon reconstruction [38], [44]. In Global Muon reconstruction, the stand-alone muon trajectory is extrapolated from the innermost muon station to the outer tracker surface (Outside-in). The Tracker Muon algorithm goes inside-out, considering all tracker tracks with a minimum p_T threshold as possible muon candidates and are extrapolated to the muon system to match atleast one muon-segment (DT/CSC hits). Combined algorithms lead to highly efficient muon reconstruction of about 99% within the geometrical acceptance of the detector.

The muon objects that are relevant to this thesis are Cosmic muons and beam-halo muons. The beam has outlier protons forming a gaussian distribution of protons about its center that can hit collimators or beam walls. They may shower to pions and those pions that decay to muons can travel through the layers of detector. Beam-halo muons move predominantly along the beam-axis. However, Cosmic-ray muons typically traverse the detector from top to bottom. Both Cosmic-ray muon and beam-halo can deposit energy in the calorimeters but avoid detection in the tracking detectors, which would result in, e.g., mismeasured missing transverse energy causing a fake signal for a single $\gamma + \cancel{E}_T$ in the CMS detector. Cosmic Muons are reconstructed as standalone muon tracks that don't require to be projective from a interaction vertex to the track in the x-y plane. Impact parameter d_{xy} , the distance from the interaction point to the track in the x-y plane, is very close to zero for muons from the collision while Cosmic muons have a flat d_{xy} distribution. Requiring these muons to be absent from the candidate sample is effective in suppressing the Cosmic muon contamination from the candidate data sample. Since both Cosmics and halo muons enter from outside CMS, their shower and timing profile is used as a discriminator to differentiate them from the direct photons as discussed in Section 5.6.3

3.2.4 Jets & Missing Transverse Energy

Jets and \cancel{E}_T are physics objects that need an information from multiple detector subsystems. In this analysis, jets and \cancel{E}_T are reconstructed using particle flow algorithm [45], [46]. The algorithm aims at reconstructing the stable particles using all the

CMS subdetectors to provide a complete global description of an event. It begins with the building of its fundamental elements, charged-particle tracks, calorimeter clusters and muon tracks. Then, it links the information between these “elements” to create the blocks. These links are created between a charged-particle track and a calorimeter cluster, between two calorimeter clusters and a charged-particle track in the tracker and a muon track in the muon system based on the distance between their positions in $\eta - \phi$ plane. In the final step, the algorithm identifies the particles. For each block, muons are reconstructed first followed by electrons, after which their corresponding tracks and clusters are removed from further processing. Depending on the energies deposited in the ECAL, HCAL clusters and their compatibility with the track momentum, the remaining information is used to form charged hadrons, neutral hadrons and photons.

All the reconstructed particles are then clustered to form jets according to anti- k_T [47] algorithm with radius parameter $R = 0.5$. The efficiency of the jets, defined as fraction of generated jets that get reconstructed, is more than 80% with $p_T > 20$ GeV and 100% is reached above 40 GeV. Neutral weakly-interacting particles, such as neutrinos or gravitons escape from the detectors without interacting and hence they don’t produce any response in the detector elements. The presence of such particles is inferred from the imbalance of total momentum. The vector momentum imbalance in the plane perpendicular (transverse) to the beam direction is known as missing transverse momentum and its magnitude as missing transverse energy, E'_T . Missing transverse momentum is calculated as negative of the vector sum of transverse momenta of all the reconstructed particles using particle flow algorithm. Its modulus gives the measure of *met* in the event.

3.3 Photon Reconstruction

In the interest of this thesis, photon is the only visible particle in the detector that forms the final state of the process being looked at. Photons and electrons behave very similar when interacting with the material. At high energies, they loss their energy via pair production and Bremsstrahlung. Electrons radiate photons and photons convert to electron-positron pairs leading to electromagnetic showers inside the calorimeter crystals. These showers are spread over several crystals in the ECAL. A photon or an electron deposits about 97% of its energy into an array of 5×5 crystals [38]. Hence, to give the best possible energy measurement neighbouring crystals are grouped together to form clusters. This process is referred to as basic clustering and the resulting clusters of crystals are referred to as basic clusters.

However, the interactions of photons and electrons in the tracker material in front of the electromagnetic calorimeter adds on another complexity. The magnetic field causes

the charged particles to separate along the ϕ direction leading to the energy deposits to be spread over broader regions in ϕ . Therefore, to recover this energy loss, clusters in both the EB and EE over a larger region in ϕ are grouped among themselves. This process is referred to as super clustering and the resulting group of basic clusters as one is referred to as a super cluster. The super-cluster (SC) reconstruction is similar for both the photons and electrons. Once the super-clusters are formed, various energy corrections are applied and then after they are associated with a photon or an electron present in the event. This section details the clustering algorithms used for electron and photon reconstruction followed by the definition of the photon candidate in the event.

3.3.1 Clustering Algorithms

In the ECAL Barrel (EB), clustering is performed using the Hybrid algorithm [48]. The algorithm works as follows:

- Starting from all the hits in the EB, a list of hits above a minimal E_T ($E_T > E_T^{seedthr}$) is formed from the event and sorted in E_T . All such hits can seed a cluster and thus called as seeds.
- To avoid any sort of double counting, each seed is checked if it doesn't belong to a cluster already.
- A domino of 3×1 crystals is made in $\eta - \phi$ direction around the seed. The domino is extended to 5×1 crystals if energy of the domino is greater than E_{wing} (with E_{wing} set to 0 ensures that 5×1 dominoes are always made).
- If the energy of this domino, called as seed domino, is below E_{seed} the algorithm goes back to next seed in the list of seeds.
- If the seed passes all the above requirements, dominoes are made as done in third step for all the crystals aligned in the same η as the seed crystal which satisfy $|\phi^{crystal} - \phi^{seed}| < \phi^{road}(N_{step})$. If energy of the domino is below the threshold E_{domthr} , it is eliminated.
- The dominoes are then clustered in the ϕ direction ending up as a super-cluster of one or more sub-clusters (or basic clusters) for this seed.
- The algorithm continues until all the seeds from the list have been scanned.

Since the EE has a different geometry than the EB, the Hybrid algorithm cannot be applied there. Instead, the same idea of collecting the clusters within a window in η and ϕ is implemented in a different manner in Multi 5×5 algorithm [48]. Similar to

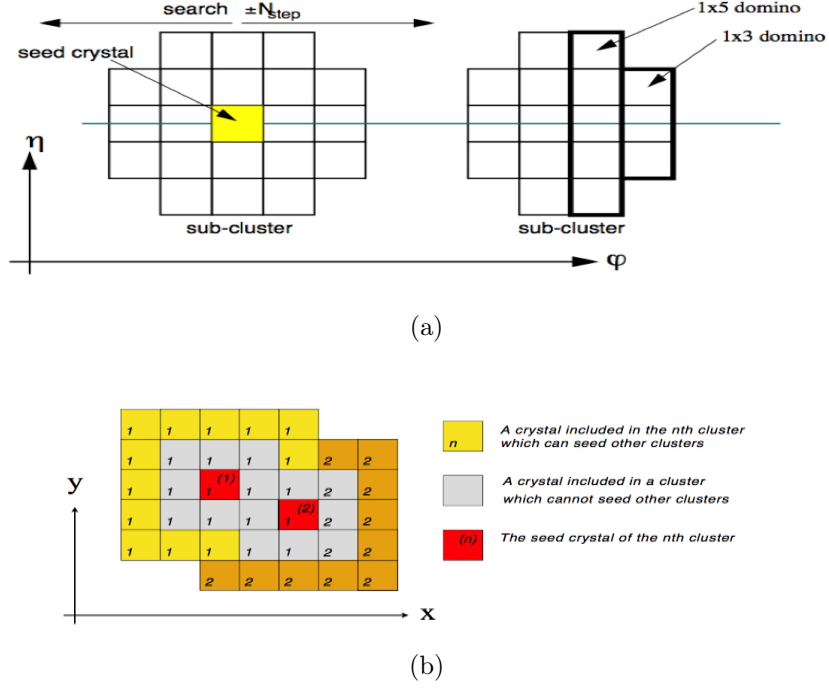


Figure 3.4: An illustration of the a) Hybrid clustering algorithm used in the ECAL barrel region and b) 2 overlapping Multi5x5 clusters.

Hybrid algorithm, this algorithm also starts from sorted hits (seeds) in E_T above $E_{seedthr}$ and makes sure that it does not belong to a cluster already. The algorithm proceeds as follows:

- If the seed is a local maxima in energy by comparing its energy to its four neighbours in a Swiss Cross pattern, the clustering process continues else it goes back to the previous step to look for the next hit.
- A 5×5 matrix of crystals is constructed around the seed including only crystals that do not already belong to a cluster.
- The algorithm continues until all the seeds have been scanned giving a set of clusters.

In distinction with the hybrid algorithm, to allow for the recovery of showers due to bremsstrahlung, here the outer 16 crystals of the 5×5 matrix may seed a new matrix, thus the matrices can overlap. Common crystals between the matrices can belong only to one matrix. Having the set of clusters, clusters within a particular $\eta - \phi$ window ($\Delta \eta^{road} - \Delta \phi^{road}$) are collected with the seed cluster above E_{seed} to form a super-cluster.

The working scheme of both the algorithms is shown pictorially in Figure 3.4 and the values of the parameters that were used during 2011 data-taking are given in Table 3.1. Regardless of the algorithm, the super-cluster position is calculated by taking the

Hybrid Algorithm		Multi5x5 Algorithm	
Parameter	value	Parameter	value
$E_T^{seedthr}$	1 GeV	$E_T^{seedthr}$	0.18 GeV
E_{seed}	0.35 GeV	E_{seed}	1 GeV
ϕ^{road}	17 crystals	ϕ^{road}	0.6
E_{domthr}	0.1 GeV	η^{road}	0.14

Table 3.1: Values of the clustering algorithm parameters

energy-weighted mean of positions of its component clusters. Total clustered energy from the super-cluster is then corrected for various factors coming from η dependence of the lateral energy leakage that arise from the 3° off-pointing of the EB crystals, interactions with material in front of the ECAL and another correction function to compensate the dependence on super-cluster E_T and η [31].

Since super-clusters are in common between electrons and photons, the electrons are distinguished from the photons by requiring a corresponding track in the tracker as discussed in section 3.2.2. However, photon candidates are reconstructed from all the super-clusters above a $E_T > 10$ GeV and $H/E < 0.5$ assigning them the location of the primary vertex. H/E is defined as the ratio of energy in the HCAL in a cone of $\Delta R = 0.15$ around the SC centroid behind the SC, to the SC energy where $\Delta R = \sqrt{\Delta \phi^2 + \Delta \eta^2}$. Further, these photon candidates are cleaned from the electron SCs in the event such that the both the electron and photon SC are well separated in ΔR . To increase the purity of the photon, additional isolation and identification requirements are applied based on the activity around the direction of the photon in the tracker, ECAL and the HCAL. Such identification has been used in the analysis and is discussed in section 5.3.

3.4 Monte Carlo Simulation

Monte Carlo (MC) simulation is done to predict the results, study various properties of inelastic pp collisions and understand the detector response. Various MC event generators are available that generates/simulates such events giving a chance to high-energy-physics community to study them. The processes that model a pp collision include modelling of partonic sub-structure of proton, calculation for matrix-element for a hard-scattering, the initial/final state radiations, hadronization of quarks and gluons into jets, the decay of unstable particles and the underlying event activity. Figure 3.5 shows a typical hadron-hadron collision from the beginning when two protons collide until the final stage where final state particles are open to be observed in the detector.

An event is simulated broadly in four steps where, the first step is to calculate the

matrix element for a hard scattering that happens between the two high energetic partons of the incoming protons. In the second step, the initial or final state radiations are taken into account with their non-negligible probability which initiate a shower. At this step parton showering takes care of the collinear splittings of the partons. In the third step, the hadronization is done that describes the modelling of colour neutral hadrons from various quarks/gluons produced after the parton showering. Ultimately, the interactions of all the other particles that are present within the hadrons that pass through each other at collision point are described by the underlying event description.

There are various event generators that are available for use. PYTHIA 6 [49] is one of the most well established package that performs all the steps described above, whereas MADGRAPH [50] is only a Matrix Element generator which calculates the matrix element for the hard scattering information which is then passed to pythia for parton showering followed by complete steps to have the description of the full event.

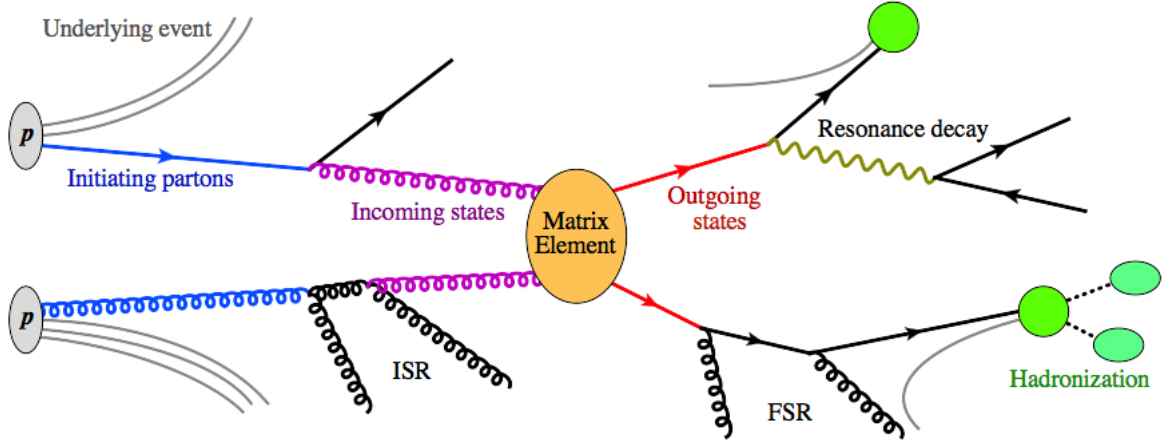


Figure 3.5: Various stages of an event generation in a pp collision [51]

To understand the response of the readouts from the detector, one simulates all the particles that come out from event generation using the detector simulation. All particles are propagated from the interaction point through the magnetic field and the CMS detector geometry. GEANT4 [35] provides a full description of how every element of the detector is positioned in space, its material. It simulates the detector effects considering all the possible interactions that particles may undergo inside the detector volume providing the simulated hits and the energy loss to mimic the real collision activity. Finally, the readouts and trigger electronics are emulated, also referred to as digitization process from these simulated hits.

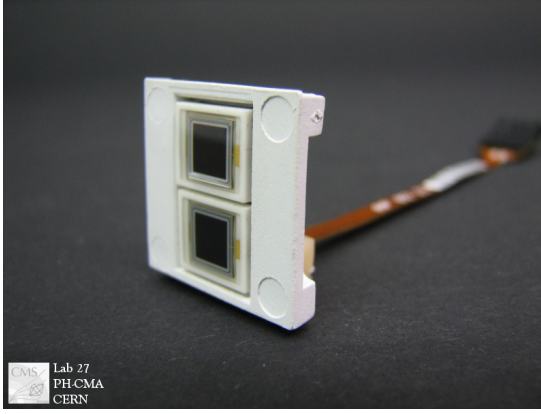
Chapter 4

Anomalous signals in CMS Electromagnetic Calorimeter

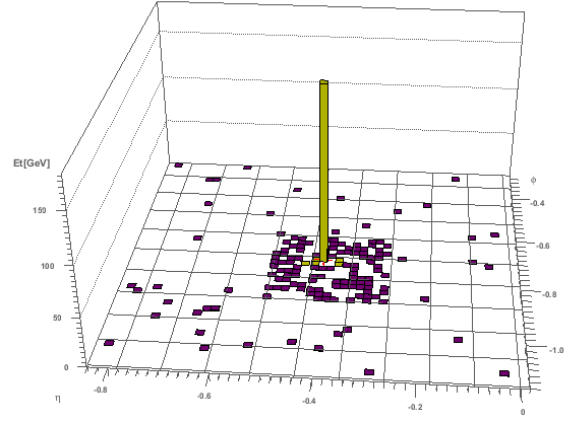
This chapter describes the large anomalous signals in the electromagnetic calorimeter often called spikes, that are observed in the CMS ECAL Barrel. These are spurious signals and if remain untreated, majority of the candidates that fire the electromagnetic triggers would be caused by spikes. This poses a big challenge at different levels of the ECAL data flow, starting from the Level-1 trigger till the offline reconstruction and analysis of EM objects. First $\gamma + \cancel{E}_T$ event seen in the CMS data in the year 2010 was soon established to be an ECAL spike. This indicated the importance of study of these anomalous signals in the monophoton study presented in this thesis. Section 4.1 describes the properties of spikes and the methods that are employed to reject them from the physics data at Level-1, the high-level trigger and in offline reconstruction are discussed in section 4.2. The performance of these algorithms is summarized using 2012 data in section 4.3. With the upcoming challenges of higher pile-up, increased noise due to ageing of the detector, a study is conducted to understand spike removal performance using MC simulations. To achieve that first a validation is done for the spikes simulations covered in section 4.4. Finally, the projections for future spike killing performance at 14 TeV are derived from Monte Carlo simulations in section 4.5.

4.1 Spike properties

In the barrel part of the ECAL, the signal is read out using Avalanche Photo Diodes (APD). Each APD has an active area of $5 \times 5 \text{ mm}^2$ and a pair is mounted on back of each of the lead tungstate crystal (Figure 4.1a). The origin of the spikes is understood to be due to low energy charged hadrons or ions that enter the APD's and cause large anomalous signals through ionization loss in the thin high gain silicon layer [52]. The



(a)



(b)

Figure 4.1: a) a pair of APD b) Typical spike energy deposit in the ECAL barrel. RecHit transverse energy: 184 GeV, Rehit reconstructed time: -10.5 ns [53]

general properties of the anomalous signals [53] are as follows:

- These are isolated high energy deposits as shown in Figure 4.1b. They have anomalous pattern of energy sharing between the crystals which is inconsistent with that expected from an average electromagnetic shower.
- They are reconstructed as apparent “early” signals. As a consequence of that timing distribution has a long positive tail.

Table 4.1 shows the average spike rate per minimum-bias event as a function of LHC center-of-mass energy. At 7 TeV, one spike is observed in every 370 minimum bias events. The rate of these anomalous hits is proportional to the number of charged particles per event, hence it increases with center of mass energy of the pp collisions. Given the high pile up scenario (multiple interactions per bunch crossing) at the LHC, the average event activity increases. This makes spikes less isolated and hence adds on another complexity.

C.M. energy (GeV)	Spikes/Minimum Bias event
0.9	$(1.666 \pm 0.089) \times 10^{-3}$
2.36	$(1.811 \pm 0.342) \times 10^{-3}$
7.0	$(2.697 \pm 0.005) \times 10^{-3}$

Table 4.1: Average spike rates per Minimum Bias event as a function of LHC center-of-mass energy. Spikes are defined as RecHits with 3 GeV and $(1-E_4/E_1) > 0.95$.

4.2 Rejection algorithms

In order to eliminate spikes from physics analysis, a multi-layer cleaning method is applied. This cleaning is sub-divided into online and offline cleaning. Online reconstruction of any signal from the detectors is done at L1 and HLT, when a decision is made whether the data is to be stored for the further processing [54].

At L1, these signals are prevented from triggering the Egamma (EG) triggers by adding an additional functionality in ECAL front-end electronics [54] called as Strip Fine Grain Veto Bit (sFGVB). To distinguish real EM showers against the spikes, sFGVB algorithm counts the number of crystals above a given E_T threshold within the eta strips of a trigger tower. If any of the 5 eta strips have more than 2 crystals above this threshold, the energy deposition is considered as real EM shower and the designed bit returns 1. Working of sFGVB is explained in Figure 4.2. If sFGVB is set to zero and transverse energy of the trigger tower is more than 8 GeV (another parameter known as killing threshold), the energy deposit is considered as a spike. It rejects $> 95\%$ of the spikes with transverse energy greater than 8 GeV while affecting the efficiency of well identified electrons to a level less than 0.5% with $E_T > 20$ GeV [55].

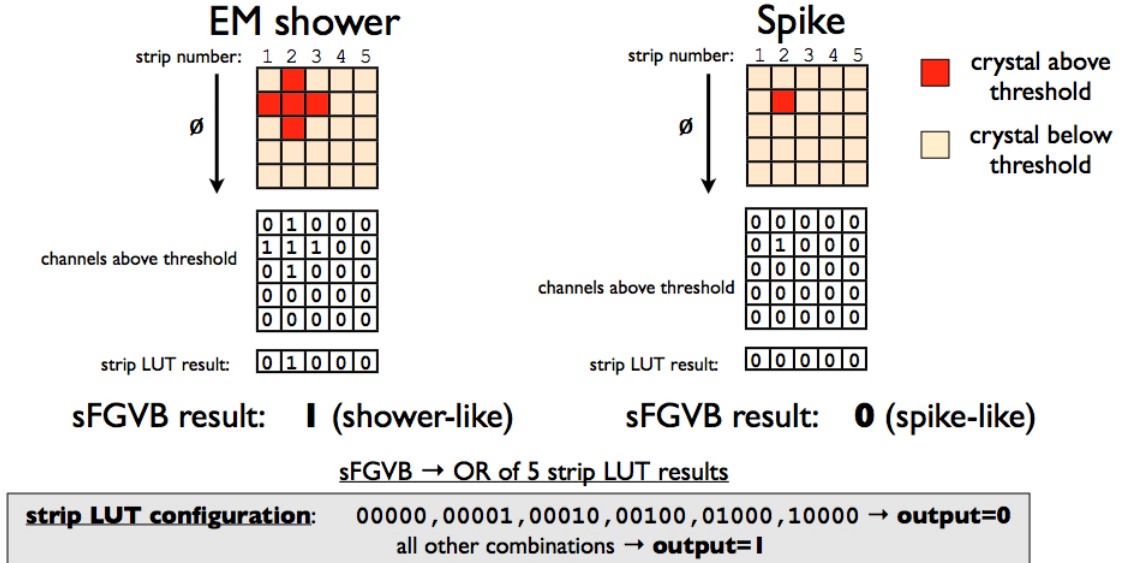


Figure 4.2: Working mechanism of sFGVB

While at HLT, a second level of topological cleaning is applied. Two discriminating variables are designed for the purpose called as kWeird and kDiweird. kWeird is defined as the ratio of E_4/E_1 as shown in Figure 4.3, where E_1 is the highest energy central crystal and E_4 as the summed energy in the adjacent crystals in the swiss-cross pattern. The crystal's energy is considered in the sum only if its energy is above 80 MeV. kDiweird

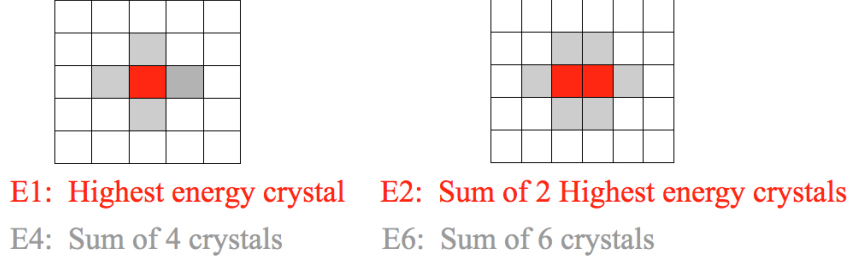


Figure 4.3: Calculation of $E4/E1$ and $E6/E2$. $E6/E2$ is calculated as $((E4_1/E1_1) + (E4_2/E1_2))/(E1_1 + E1_2) - 1$, where 1 & 2 are the first and second highest energy crystals respectively.

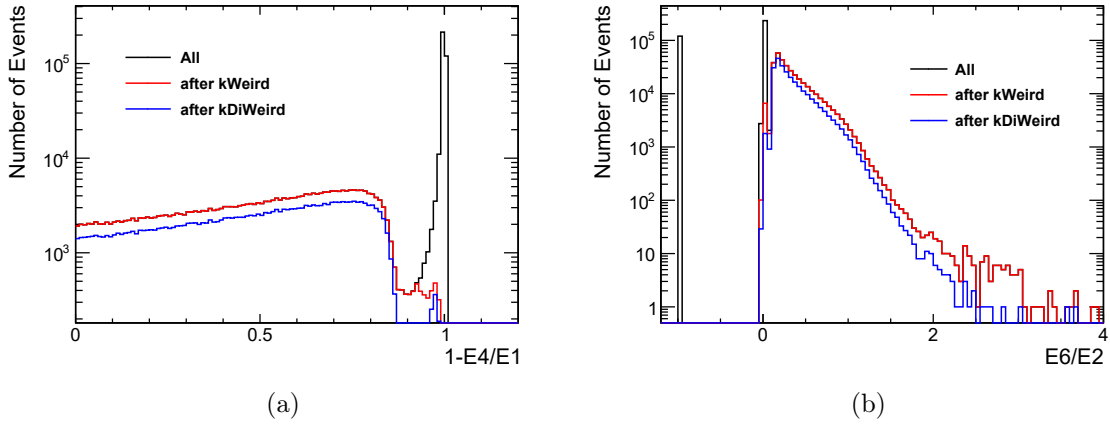


Figure 4.4: a) $1-E4/E1$ b) $E6/E2$, where the black histogram shows the distribution for all photon objects followed by a red histogram after rejecting photons that pass kWeird and in blue the distribution is plotted after rejecting photons further requiring kDiWeird to be true.

on the other hand is $E6/E2$ (Figure 4.3), where $E2$ is the summed energy in two highest energy crystals and $E6$ is the energy of all the 6 nearest adjacent crystals around the central 2 crystals.

Figure 4.4a shows the distribution of $1-E4/E1$ (called as swiss cross variable). The peak around 1 is due to the presence of spikes. The second distribution (Figure 4.4b) shows the distribution of $E6/E2$, where the entries at -1 and close to zero are due to spikes.

The thresholds that are chosen to flag a spike are taken as $E4/E1 < a \log_{10}(E1) + b$ (EB: $a = 0.04$ and $b = -0.024$, EE: $a = 0.02$ and $b = -0.0125$). While kDiweird flags a spike if $E6/E2 < 0.04$.

Offline cleaning is a third level cleaning on the reconstructed objects (photons and electrons) where the same topological cleaning is applied. In addition, the reconstructed time(T) of the most energetic ECAL crystal in the cluster (seed) is required to be in-

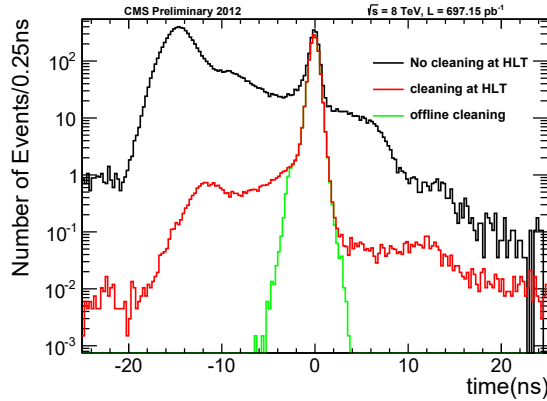


Figure 4.5: The timing distribution is plotted using data where, no cleaning at HLT is applied (black), topological cleaning (used at HLT) is applied (red) and topological and timing cleaning (used in offline reconstruction) are applied (green).

time. So if $|T| > 5\sigma$ (out of time) from zero, where σ is the single channel time resolution (better than 1 ns for $E > 4$ GeV), it does not form a valid cluster. Figure 4.5 shows the distribution of the reconstructed time of signals from the seed crystals of photon candidates for 8 TeV pp collision events. The peak at zero is due to prompt electromagnetic showers. The secondary peak at 10 ns is due to spikes. The origin of the 10 ns is due to differences in the pulse shapes of spikes and EM energy deposits. Distributions are normalized by the integrated luminosity. A large rejection of the out-of-time signals due to spikes is achieved by applying topological cleaning in the HLT (red histogram). Additional rejection is provided by applying timing cuts offline (green histogram). The left-hand shoulder in the green histogram is understood to be due to the presence of beam halo events.

4.3 Spike killing efficiency using 2012 data

With the increasing luminosity at the LHC from its start in year 2010 till the end of phase 1 run in December 2012, the pile up (PU) conditions faced by the CMS detector changed drastically. The average number of interactions per bunch crossing increased from less than 5 to more than 20. The rate of spikes is directly proportional to the number of interactions per bunch crossing. Thus, it is important to understand how sensitive the mitigation techniques discussed in section 4.2 are with respect to the increasing number of interactions. Since both online and offline spike killing techniques are based on the nature of event activity around the spike in the ECAL, the expectation is that the performance would go low as the pile up increases making the spike less isolated.

Figure 4.6a shows the fraction of spikes triggering the L1 EG-15 trigger versus event pile-up using the 2011B data at 7 TeV. The hit that matches with the L1 candidate that

triggered L1 EG-15 trigger is defined as a spike if its $E_T > 8$ GeV with swiss-cross above 0.95. With a working point of sFGVB threshold as 258 MeV and spike killing threshold of 8 GeV in 2011, it shows that the fraction of spikes that trigger the EG-15 trigger goes beyond 10% at high pile-up shown in green. A mild dependence is observed with the increase in pile up interactions. However, if one emulates this data with a new setting of sFGVB threshold as 350 MeV and spike killing threshold as 12 GeV, it is found to be more robust against pile-up. These thresholds were implemented for the data-taking period in 2012.

In Figure 4.6b, the efficiency of the topological ECAL spike cleaning (kWeird) is plotted as a function of the number of pile-up vertices using pp collision data at 8 TeV. The efficiency of this cut is computed using 28 pb^{-1} of data taken in early 2012 where topological spike cleaning was disabled at HLT. A spike-enriched sample of photons is selected by requiring that the reconstructed time of the most energetic ECAL crystal in the photon cluster (seed) is out-of-time. Only events triggered by the HLT trigger with photon object above 150 GeV and photon seeds with reconstructed energy above 4 GeV are considered. To ensure the purity of the sample, beam halo events are removed from the sample. The plot shows that the efficiency of this cut is higher than 98% and there is no degradation with increase in pile-up. Error bars here refer to the statistical uncertainty.

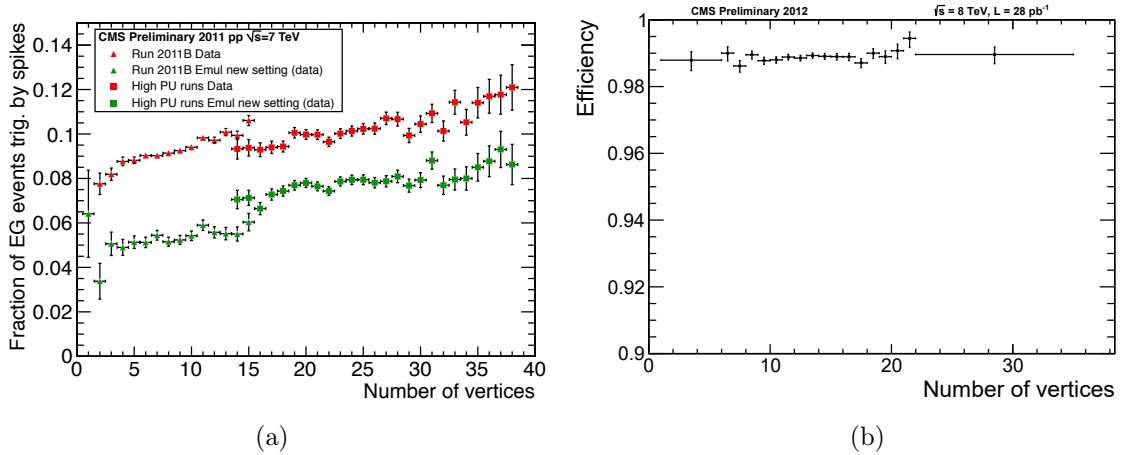


Figure 4.6: a) Fraction of spike-induced EG triggers as a function of the number of reconstructed vertices for the 2011B data (triangles) and High pileup runs (squares). The red points represent the spike removal working point used in 2011 and the green points the optimized working point for 2012 [56]. b) Efficiency of the Swiss-cross topological cut as a function of the number of reconstructed vertices for early 2012 data.

4.4 Spike simulation

The baseline programme of LHC running has been divided in two phases depending on the considerable luminosity increase after the phase-1 run completes. Phase-1 run is proposed to complete in 2022. There are two long shutdowns (LS) planned during phase-1 run. Currently, a long shutdown (LS1) is ongoing and another one (LS2) is planned during 2018-2019. Phase-2 run of LHC is intended to start in 2025 after a long shutdown (LS3) during 2023-2024. Projected integrated luminosity collected by the end of phase-1 and phase-2 running is 300fb^{-1} and 3000fb^{-1} respectively. Expected average pile-up conditions during the phase-1 run is about 70 and 140 for the phase-2 run. Since spikes are a potential problem and need specific attention for the collection of good data at CMS, the sensitivity of spike mitigation techniques needs to be understood with the luminosity and PU conditions expected at high luminosity LHC (HL-LHC) at 14 TeV.

To understand the nature of spikes its simulation is implemented in the Monte Carlo and is tuned using the minimum-bias triggered data at 7 TeV referred to as “default” tuning [57, 58]. This section in first part describes the validation of spike simulation using 8 TeV data with default tuning. In the second part, a description of how the spike simulation is used to predict the performance at 14 TeV and high event pile-up, also with detector ageing (increased electronic noise in EB) is covered.

4.4.1 Validation of spike simulation using 8 TeV data

For the validation of spikes-simulation, data from 2012 Run C data-taking period is considered. Data corresponds to the events coming from Run Number 202299 and is required to trigger on any of the Zero-bias trigger.

A corresponding minimum-bias sample is generated with Run C conditions at 8 TeV with average in-time pile-up interactions as $\langle\text{PU}\rangle = 20$, the detector ageing scenario as an input from Run C data itself, a default out-of-time (OOT) pile up scenario of $[-3, +2]^1$ with bunch spacing at 50 ns and spikes activated with the default tuning. Figure 4.7 shows the comparison of rechit energy, swiss-cross and timing respectively between the 2012 Data with this spikes-simulated sample.

Figure 4.7a shows that MC underestimates the rechit energies towards the higher end of the energy spectrum above 10 GeV, while the swiss-cross spectrum in Figure 4.7b is well predicted by MC. The timing distribution for rechits above 2 GeV in Figure 4.7c tells

¹In simulation, out-of-time (OOT) pile up scenario is defined using a time window with bunch spacings separated by 25 ns. For a time window given by $[-n1, n2]$, it represents $(n1+n2)$ bunch crossings in addition to the main bunch crossing (BX0) where $n1$ and $n2$ correspond to previous and later bunch crossings. For this given time window, if the bunch spacing is doubled to 50 ns, additional bunch crossings that are simulated in addition to the BX0 are about half.

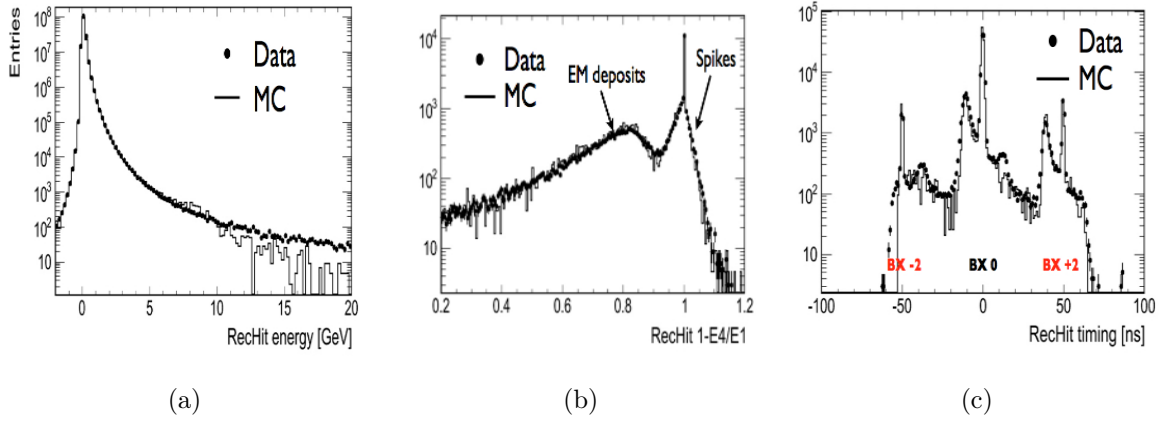


Figure 4.7: 2012 Data/MC comparison plot of a) rehit energy b) swiss-cross and c) rehit timing with spikes simulated in MC.

that an overall feature of timing distribution is modelled fine in MC as compared to the data. In this plot, 3 peaks refer to the hits from 3 bunch crossings (BX) coming from BX0 along with an early and late bunch crossing at ± 50 ns. Other peaks appear due to the presence of spikes.

4.4.2 Validation of spike simulation at 14 TeV

Since the spikes simulation at 8 TeV represents data satisfactorily, it is extended to predict the nature of spikes at 14 TeV. It has been observed that along with the data taking over the span of 3 years, the dark current in APD's has increased compared to when the detector was new. This translates to an increase in electronic noise in the ECAL [59]. When the spike-simulation has been done at 14 TeV, dark current and noise parametrization for the degraded detector corresponding to various integrated lumi has been given as the inputs [59, 60]. Though, if the temperature at which ECAL is operated currently (at 18°C) is reduced, noise can be controlled. A specific scenario is considered with integrated luminosity of 1000fb^{-1} and average pile up of 140. This corresponds to the conditions with integrated luminosity of 3000fb^{-1} and average pile up of 140 but with the temperature reduction in ECAL to 8°C compared to the current operation at 18°C. Thus it helps to understand how much mitigation techniques might gain if the temperature is brought down as discussed in next section 4.5. In Figure 4.8a, the electronic noise is plotted in ADC counts as a function of eta in the ECAL Barrel. As one goes towards the higher eta region, the noise increases as the neutron dose increase. Also with the ageing of the detector, equivalent to saying as the integrated lumi increases, the noise increases.

Along with the noise modelling, two high event pile-up conditions with in-time pile

up as $\langle \text{PU} \rangle = 70, 140$ have been considered at 14 TeV corresponding to end LHC and high luminosity LHC. The OOT pile-up conditions have also been extended to $[-12, +3]$ with bunch spacing decreased to 25 ns [61]. However, for the case at 8 TeV, the noise and pile-up conditions have been taken directly from data. The OOT scenario used for 8 TeV is $[-8, +2]$ at bunch spacing of 50 ns. Figure 4.8b shows the increase in pile-up interactions per bunch crossing (BX) for different pile-up conditions between 8 TeV and 14 TeV runs with which the simulation has been done.

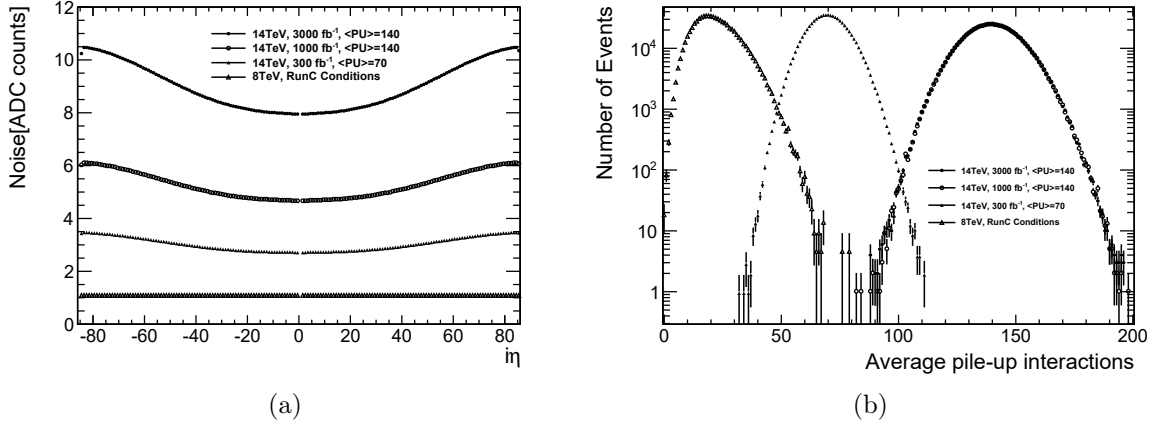


Figure 4.8: a) Noise increase with the ageing of the detector. c) Pile-up interactions per bunch crossing.

To understand how spikes scale at 14 TeV with different pileup conditions, there are multiple factors that it depends on. As observed from data, there is a logarithmic dependence on center of mass energy, as number of charged particles produced in the collision increase logarithmically with c.o.m energy. Thus, if the spike rate is known at a given energy, it can be translated to what one would expect at higher c.o.m energy using the relation,

$$\frac{r_2}{r_1} = \frac{\log(E_2)}{\log(E_1)} \quad (4.1)$$

where, E_1 and E_2 are the 2 center of mass energies and r_1, r_2 are the corresponding spike rates. One expects the number of spikes to scale linearly with pile-up. However, this dependence gets biased by the presence of OOT pile-up conditions as the pulse is reconstructed from the 10 digitized samples with a timing window of 25 ns. A spike is identified as an APD digi that has a maximum digitized sample with 50 ADC counts above the pedestal. The spikes that occur during in-time collisions should mostly have a pulse with maximum on the 6th sample, similarly in-time spikes coming from other BXs should have the the maximum on the respective time sample. Thus, to observe the scaling

of spikes with pile-up, a count on spikes is made per event which have their maximum on 6 sample and that is compared with the in-time pile up at BX0. Figure 4.9 shows such a plot and a linear increase in spikes is observed as the in-time pile up interactions at BX0 increase between the different samples.

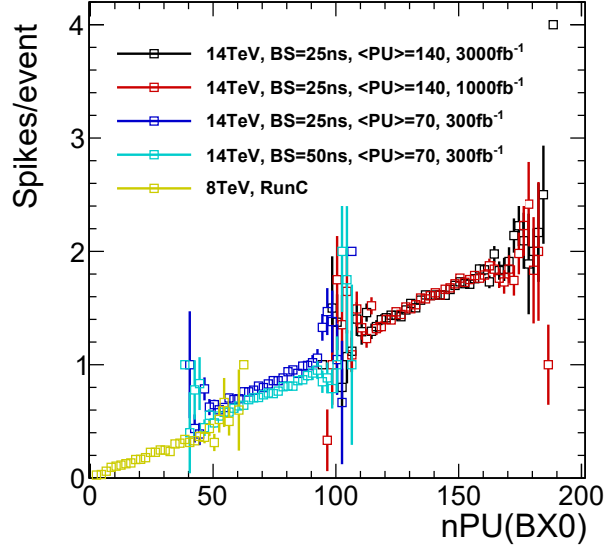


Figure 4.9: Spike rate (number of in-time spikes with ADC count above 50) plotted as a function of in-time pile up (pile up corresponding to BX0).

4.5 Future projections

Since the spike-simulation depicts an adequate scaling of spikes in high pile up environment at higher c.o.m energy, this section presents the summary of the results on spike rejection and signal inefficiency obtained from upgrade simulations studies. In terms of spikes rejection, it is expected that the performance worsens at 14 TeV with the high pile-up and the degraded detector. Samples that are used include spike and $Z \rightarrow e\bar{e}$ MC events generated at 14 TeV with a range of ageing and event pile-up conditions based on the different phases of LHC running. Thus, the samples considered for the study include:

- Run2012C ageing and PU conditions
- Integrated lumi = 300fb^{-1} , mean PU=70
- Integrated lumi = 1000fb^{-1} , mean PU=140
- Integrated lumi = 3000fb^{-1} , mean PU=140

4.5.1 Offline spike killing performance

Figure 4.10 and 4.11 show the swiss cross distributions from 8 TeV and 3 different categories of 14 TeV sample with a side-by-side comparison of equivalent spike and $Z \rightarrow ee$ samples in left and right respectively.

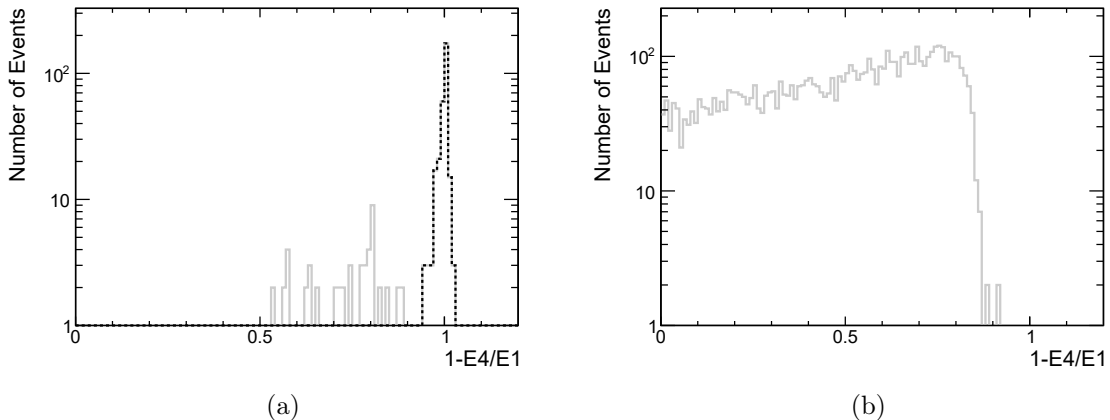


Figure 4.10: The swiss-cross distribution is plotted for spikes and $Z \rightarrow ee$ in left and right respectively for 8 TeV MC sample with 2012C ageing and PU conditions.. In left plot, the distribution is plotted for all the hits with their energy above 10 GeV (gray) and for the hits that are recognized as a spike (matched to an APD digi above an amplitude of 50 ADC counts) in black dotted line. In right plot, all the seeds of the super-clusters above 10 GeV are being considered.

As we move on to higher ageing in 14 TeV samples, the tail of the swiss-cross distribution from the hits that are matched to a spike moves towards the lower end of the spectrum and thus start having a non-zero overlap with the hits that come from real super-clusters pointing towards a need of optimization. This is as expected as the activity around the hit increases due to higher pileup and noise environment.

In Figure ?? timing distribution has been plotted from 14 TeV sample with ageing at 3000fb^{-1} of integrated lumi for equivalent spike and $Z \rightarrow ee$ samples in left and right respectively. In both the plots, dotted line shows the hits that get tagged by swiss-cross > 0.95 , thus showing that this requirement of swiss-cross at higher ageing has an inefficiency in the region for BX0 between ± 12.5 ns for spikes in the left plot and a higher probability to mis-tag the real super-clusters in the right plot. The similar observation can be read from Figure 4.13 where the distribution in η has been made. In addition, it clearly shows that as one goes towards the higher η region, mis-tagging increases due to higher noise in this region.

The efficiency of $\text{swiss-cross}(1-E4/E1) > 0.95$ is plotted in Figure 4.14 as a function of time, energy, η and pile up. All the plots show a coherent behaviour telling an inefficiency in the tagging of spikes as the pile-up and noise in the detector increases. The equivalent

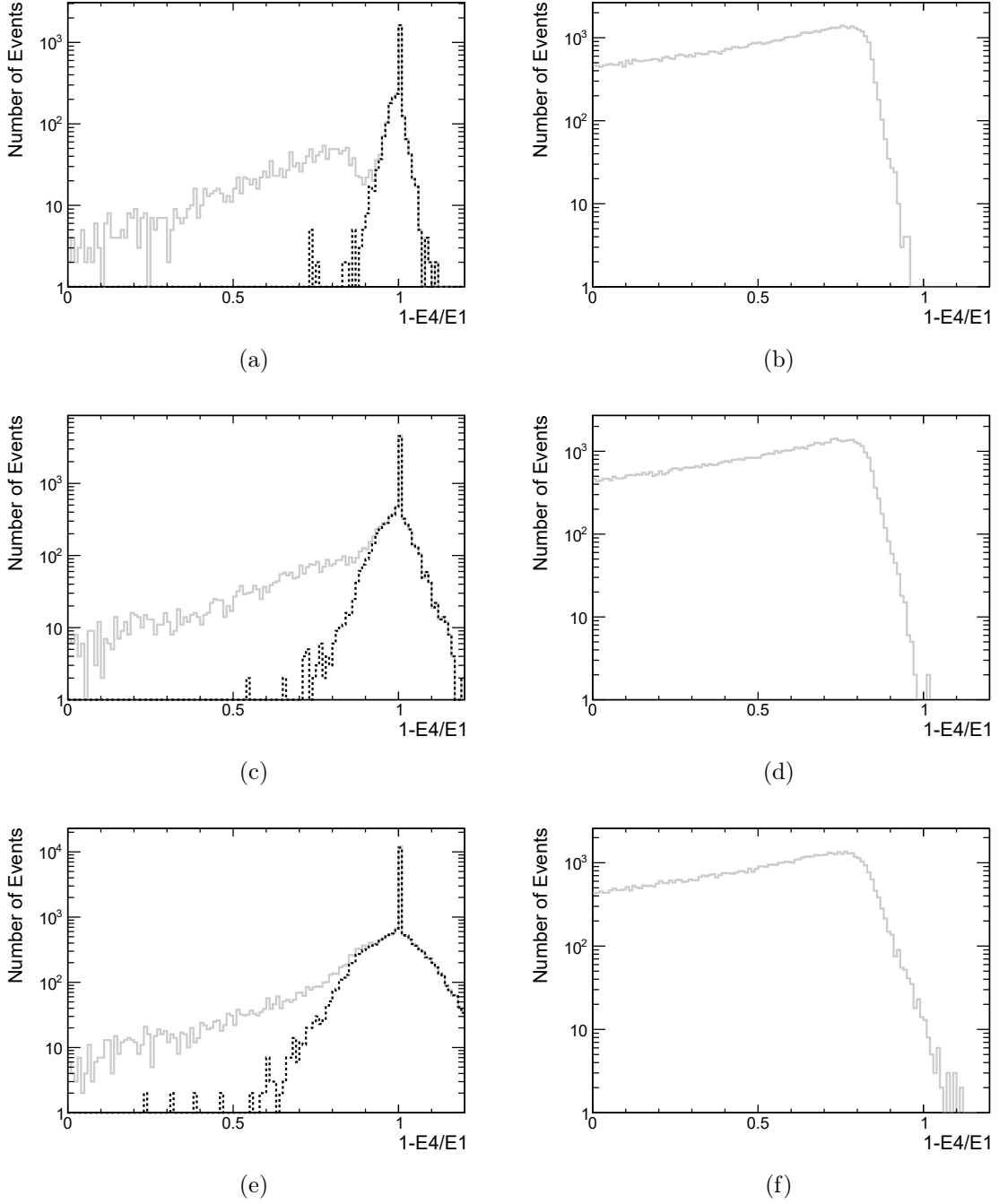


Figure 4.11: The swiss-cross distributions are plotted for spikes and $Z \rightarrow e\bar{e}$ in left and right respectively for 14 TeV MC samples. Three different rows here show three different run conditions with $\langle \text{PU} \rangle = 70$, integrated lumi = 300fb^{-1} ; $\langle \text{PU} \rangle = 140$, integrated lumi = 1000fb^{-1} and $\langle \text{PU} \rangle = 140$, integrated lumi = 3000fb^{-1} . For left set of plots, the distribution is plotted for all the hits with their energy above 10 GeV (gray) and for the hits matched to a spike in black dotted line. For Zee samples, all the seeds of the super-clusters above 10 GeV are being considered.

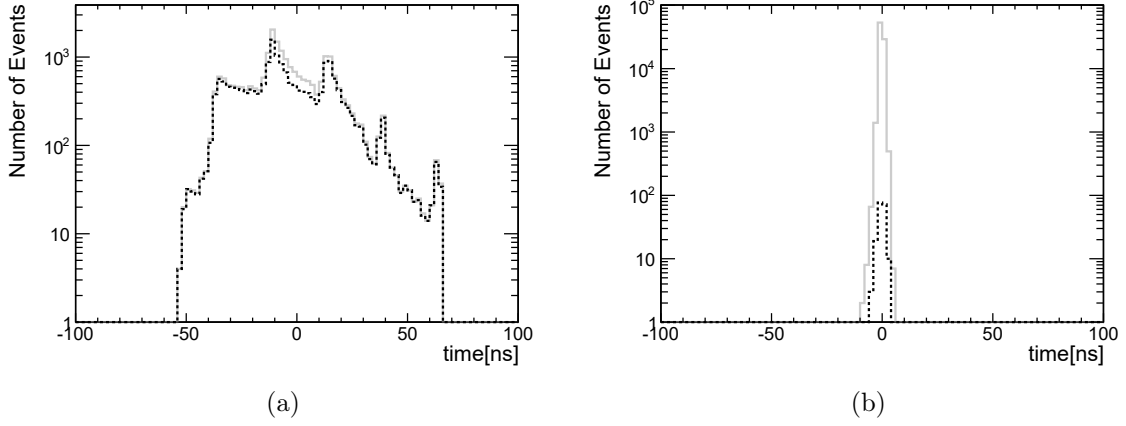


Figure 4.12: The timing distribution is plotted for 14 TeV MC sample with mean PU = 140 and ageing of 3000 fb^{-1} for spikes and $Z \rightarrow ee$ in a) and b) respectively. In left plot, the distribution is plotted for all the hits that get matched to an APD digi with their energy above 10 GeV (gray). In right plot, all the seeds of the super-clusters above 10 GeV are being considered in gray. Black dotted line shows the hits which get flagged by swiss-cross ($1-E4/E1 > 0.95$).

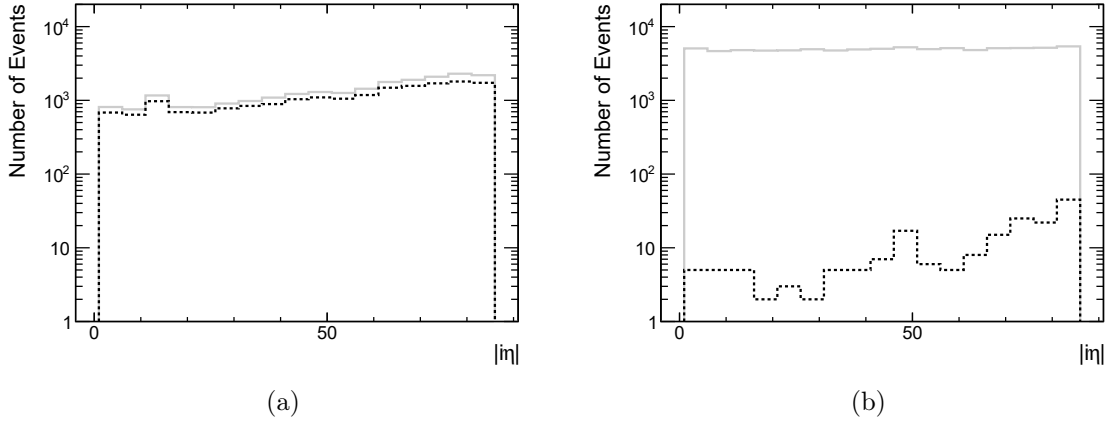


Figure 4.13: The m distribution is plotted for 14 TeV MC sample with mean PU = 140 and ageing of 3000 fb^{-1} for spikes and $Z \rightarrow ee$ in c) and d) respectively. In left plot, the distribution is plotted for all the hits that get matched to an APD digi with their energy above 10 GeV (gray). In right plot, all the seeds of the super-clusters above 10 GeV are being considered in gray. Black dotted line shows the hits which get flagged by swiss-cross ($1-E4/E1 > 0.95$).

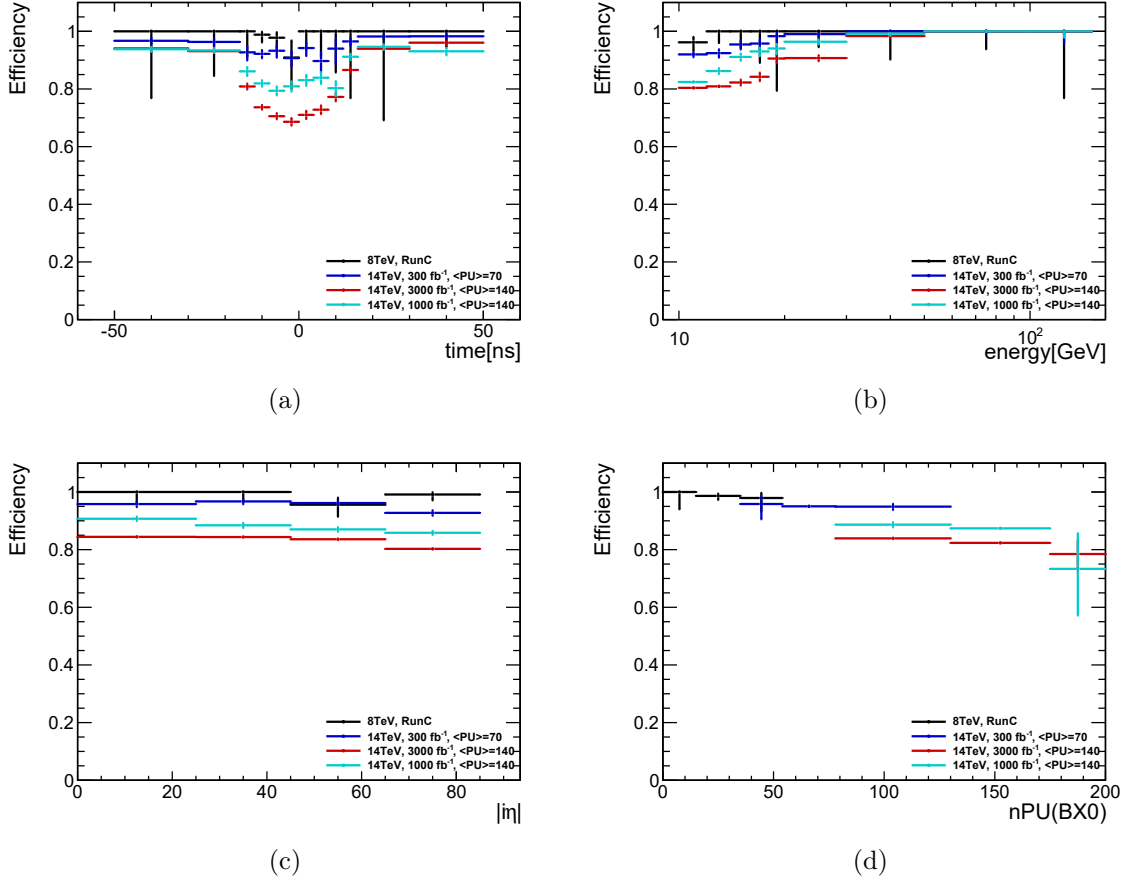


Figure 4.14: Efficiency of swiss cross cut ($1-E_4/E_1 > 0.95$) is plotted as a function of a) time, b) energy, c) eta and d) pile up in spike samples.

plot for $Z \rightarrow ee$ samples is plotted in Figure 4.15 as a function of η here exhibiting the same feature as mentioned before for increase in mis-tagging probability with higher η .

Since HLT uses swiss-cross algorithm, the aim of the study is to find an optimal point that rejects spikes maximally but real EM showers minimally at HLT. Thus, the efficiency of swiss-cross is scanned as the function of its values between 0.7 and 1.2 in both the spike and Zee samples in Figure 4.16 in the full readout region. For requiring the hits in the full readout region, hits are required to be with ± 12.5 ns (i.e. from BX0) and above an energy of 10 GeV. The plot illustrates that at the given value of swiss-cross < 1 , starting from the low pile up environment at 8 TeV towards the higher one at $\langle \text{PU} \rangle = 140$ at 14 TeV with the increase in ageing, the efficiency to tag spikes worsens seen in the first part of the plot. Left plot also says that the efficiency gets better as one goes towards the lower values of swiss-cross, however if one goes small enough in values of swiss-cross mis-tag probability increases as observed in the right plot.

Figure 4.17 gives the similar information showing the super-cluster efficiency Vs spike rejection for various values of swiss-cross in full readout region. This shows for the black

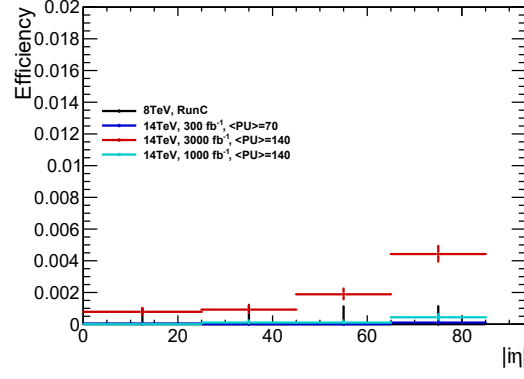


Figure 4.15: Efficiency of swiss cross cut ($1-E4/E1 > 0.95$) is plotted as a function of eta in Zee samples.

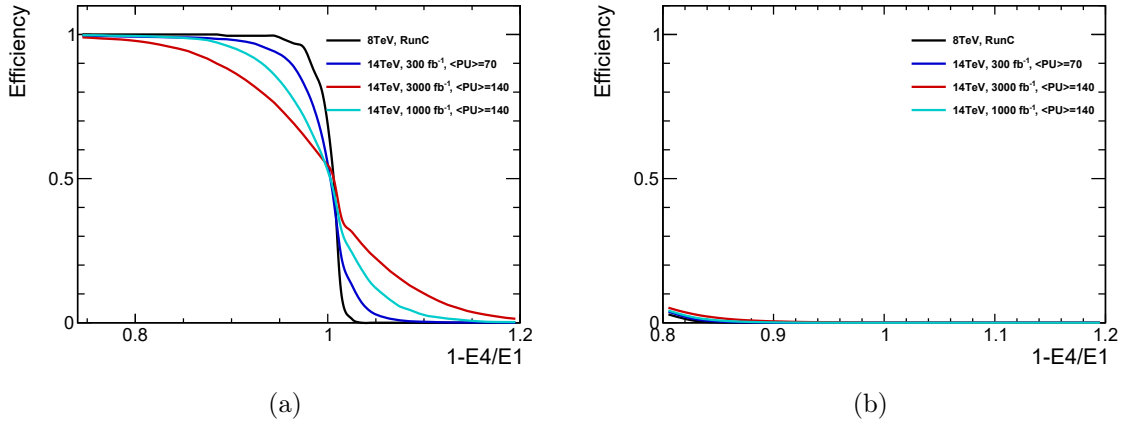


Figure 4.16: a) Efficiency of tagging spikes is plotted as a function of swiss cross value in spike samples (spike hits in the full readout region). b) Efficiency of tagging super-clusters is plotted as a function of swiss cross value in Zee samples.

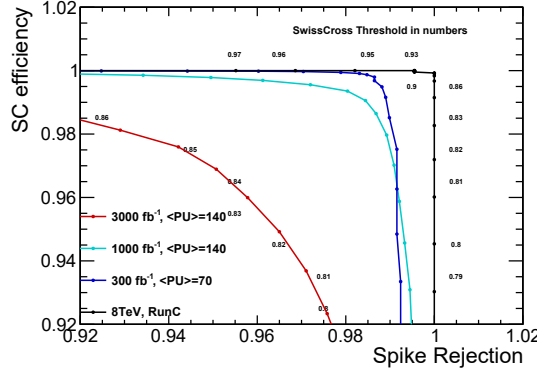


Figure 4.17: Super-cluster efficiency Vs Spike rejection curves for various values of the Swiss-cross cut for hits in full-readout regions

curve for 8 TeV, a shape edge at swiss-cross value of 0.9 where spike rejection is 100% with a very slight decrease in SC efficiency from 100%. However, as one looks at the sample with ageing of 300fb^{-1} and $\langle\text{PU}\rangle = 70$, the spike rejection at a swiss-cross value of 0.9 goes down to $\sim 98.2\%$ with about similar SC efficiency. Looking at the cases with $\langle\text{PU}\rangle = 140$ and an ageing increase from 1000fb^{-1} to 3000fb^{-1} , situation gets worse. One achieves a SC efficiency of about 99% with 98.2% rejection of spikes at a lower swiss-cross value of 0.85 for 1000fb^{-1} case while a lower SC efficiency of $\sim 96\%$ with $\sim 95.7\%$ spike rejection at swiss-cross = 0.83. At lower values of swiss-cross, the pattern shows an opposite behaviour between the samples for 300fb^{-1} and 1000fb^{-1} , that is at a similar value of SC efficiency, spike rejection is better for 1000fb^{-1} than 300fb^{-1} . This is understood as the statistical fluctuation.

Given a degraded performance of swiss-cross at HL-LHC conditions, an offline timing information can be used to achieve further rejection of spikes. Figure 4.18 shows the effect of an additional timing requirement on various samples with $|t| > 3/5/7/10$ ns with the full readout read in ± 12.5 ns. A hit is tagged as a spike in this case it either passes the swiss-cross threshold OR is out of the timing window ($|t| > X || 1 - E4/E1 > Y$). As expected the spike-rejection improves as tighter the timing requirement becomes with the same SC efficiency. However, for the case of 3000fb^{-1} , if the timing cut becomes very tight, the SC efficiency gets affected as well because at higher noise the timing resolution deteriorates.

4.5.2 Online Spike Rejection Performance

To study the performance of the online sFVGB algorithm as a function of detector ageing and event pileup, the algorithm has been emulated using the the offline reconstruction. Only hits in towers with full readout are considered. For the spike sample, the spike

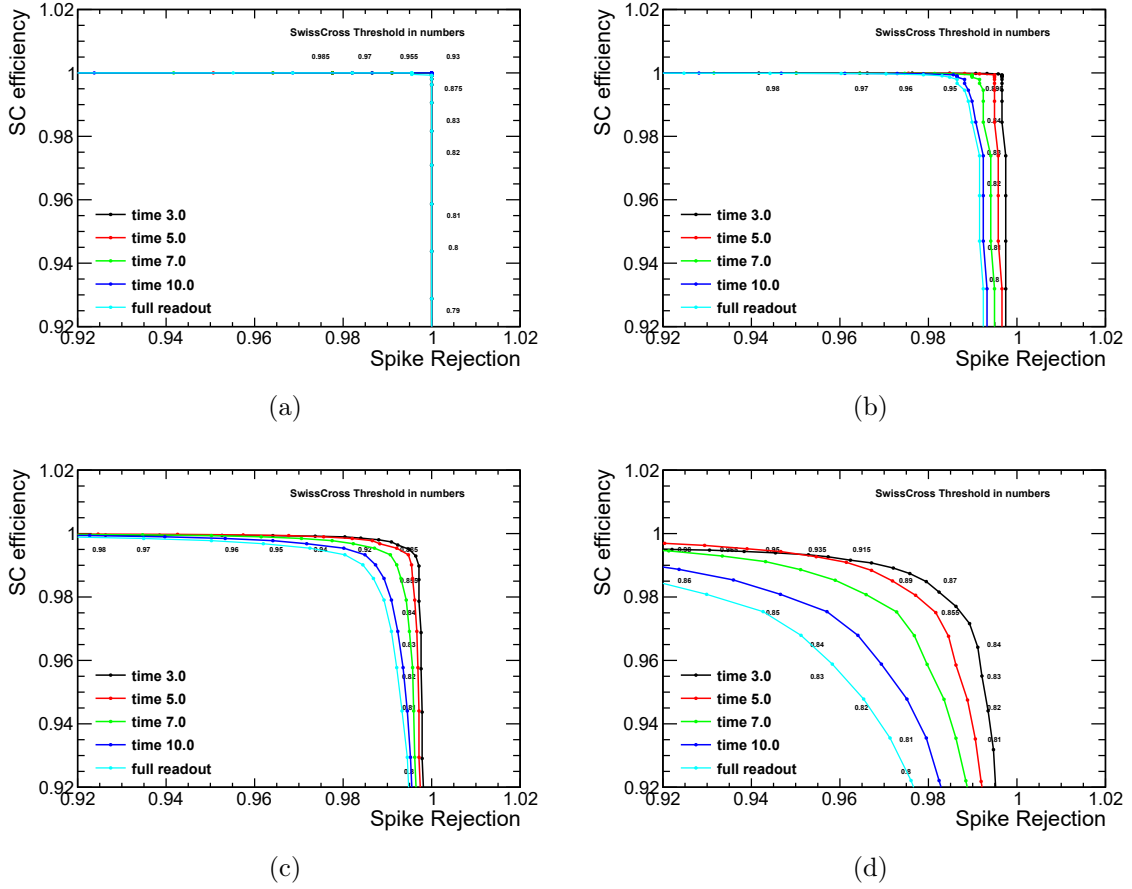


Figure 4.18: Efficiency/rejection curves for various values of the Swiss-cross cut, for hits in full-readout regions including the effect of adding a timing for a) Run2012C ageing and PU conditions b) Integrated lumi = 300fb⁻¹, mean PU=70, c) Integrated lumi = 1000fb⁻¹, mean PU=140 and d) Integrated lumi = 3000fb⁻¹, mean PU=140.

candidate is identified by considering hits in a tower that contains an APD digi with amplitude greater than 50 ADC counts (corresponding to approximately 2 GeV). For the $Z \rightarrow ee$ sample, hits are considered in towers containing a super-cluster seed with energy greater than 4 GeV.

The resulting efficiency versus rejection curves for the various ageing and PU conditions are shown in Figure 4.19. These curves are shown for a variety of tower killing thresholds, ranging from 5 to 20 GeV in transverse energy. The degradation of spike-killing performance with ageing and PU is clear when comparing results for a given value of the killing threshold.

One important conclusion is that for the case of an integrated luminosity of 3000fb⁻¹ and a mean PU of 140, it is not possible to maintain a high ($> 95\%$) spike killing efficiency while achieving a small ($< 5\%$) inefficiency for accepting EM showers. This is true even for a killing threshold of 20 GeV, the highest considered in this study. If one cools the detector

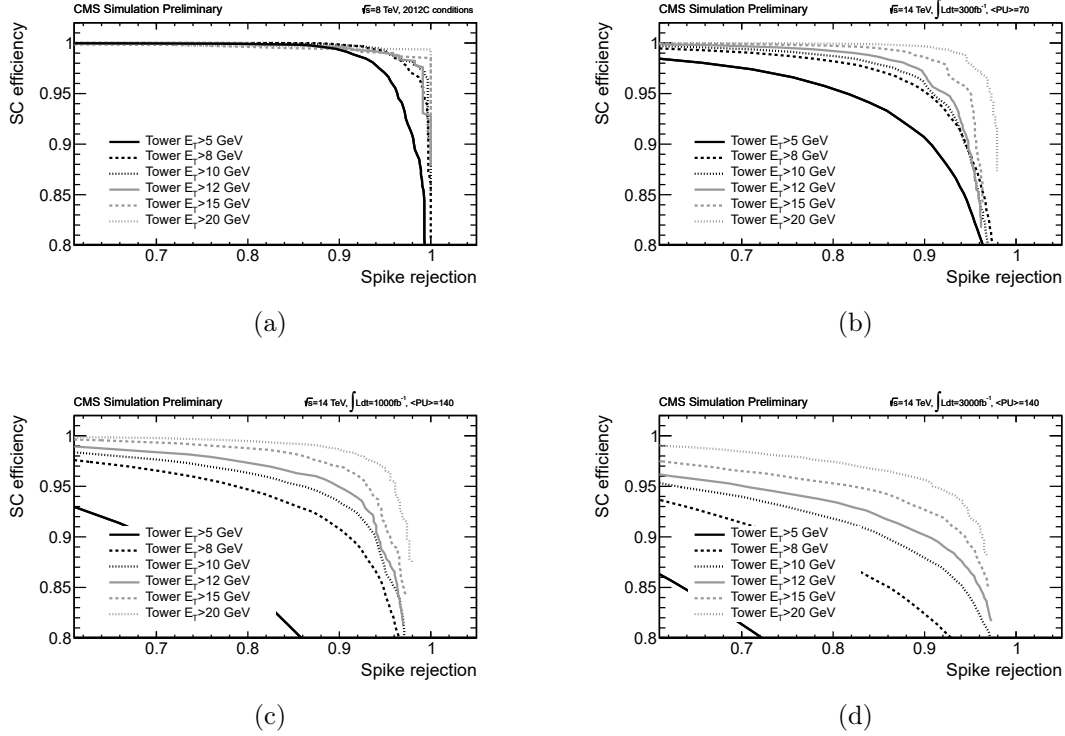


Figure 4.19: Efficiency of the sFGVB algorithm for rejecting spike signals versus acceptance of super-clusters from $Z \rightarrow ee$ events, for a range of ageing and PU conditions and for different threshold values of the transverse energy sum of the rechits in the tower. The conditions simulated are: a) Run2012C ageing and PU conditions; b) integrated lumi = 300 fb⁻¹, mean PU=70; c) integrated lumi = 1000 fb⁻¹, mean PU=140 and d) integrated lumi = 3000 fb⁻¹, mean PU=140.

from 18 to 8°C, roughly equivalent to going from an ageing of 3000 fb⁻¹ to 1000 fb⁻¹, the performance is better, but still marginal.

4.6 Summary

A brief summary of spike properties is presented. Algorithms have been developed to efficiently mitigate spikes both online (at L1 and HLT) and in offline analyses. Since a minimal degradation in the online (L1) spike killing efficiency is observed as a function of pile-up, the single channel E_T threshold and killing thresholds are re-tuned for high pile up conditions and are applied for 2012 data-taking. No degradation in efficiency is observed with high pile-up conditions at HLT using 2012 data.

A study is conducted to validate and optimize spike killing algorithms at higher luminosity and pile up conditions at the LHC using spike-simulation. A satisfactory agreement between data and MC at 8 TeV is reproduced using spike-simulation. Spikes are found to

scale linearly with pile up conditions both at 8 TeV and 14 TeV.

A degraded performance is evident at 14 TeV run conditions as pile-up and noise conditions evolve at the LHC. Upto LS3 with integrated lumi = 300^{-1} and mean PU=70 online performance from sFGVB algorithm for spike-killing is adequate but killing threshold needs to be raised. Performance at high level trigger may gain from adding a timing requirement. Beyond LS3 conditions, sFVGB performance appears to be insufficient at 3000fb^{-1} , even with a 20 GeV killing threshold. To recover the satisfactory performance, a study on additional rejection using single channel readout [62] and timing/pulse shape discrimination in the ECAL Barrel electronics is being explored.

Chapter 5

Analysis

The final state of $\gamma + \cancel{E}_T$ in pp collisions provides a rich avenue for the search of new physics. However, as discussed already in Section 1.3, this thesis explores the production of LED via direct graviton production at LHC via this final state. To define any analysis, understanding the signal and its backgrounds is crucial which is covered in the first and second section of this chapter. Section 5.3 details the selection criteria developed for this analysis. Standard model production of $Z(\nu\bar{\nu})+\gamma$ constitutes the most important irreducible background for the new physics searches with $\gamma + \cancel{E}_T$ final state. The two tree level Feynman diagrams for this process are shown in Figure 5.1.

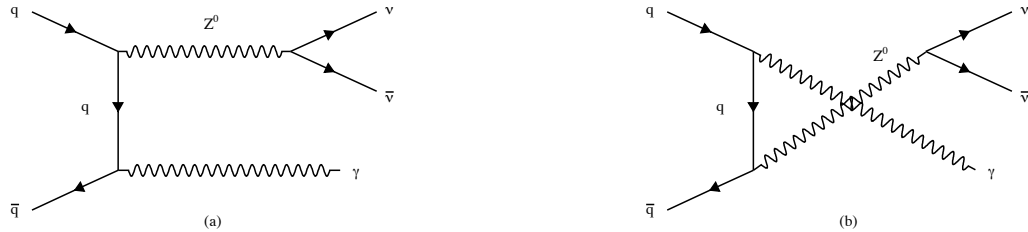


Figure 5.1: Tree level Feynman diagrams for the process $q\bar{q} \rightarrow \gamma Z$.

Thus, the cross section for the $Z(\nu\bar{\nu})+\gamma$ process is first extracted using data. To look for new physics in this final state, an excess in the photon p_T spectrum is studied compared to SM predictions. If no deviation from the SM expectation is observed then limits are set on the parameters (M_D, n) of the model.

The cross section measurement is based on the formula:

$$\sigma \times Br = \frac{N_{data} - N_{BG}}{A \times \epsilon \times L} \quad (5.1)$$

where, σ is the cross-section for the process $pp \rightarrow Z\gamma$ and Br is the branching ratio for $Z \rightarrow \nu\bar{\nu}$, which has been assumed to be 100% in this study. N_{data} is the observed number of events and N_{BG} is the number of estimated background events. A is the geometrical and kinematic acceptance of the selection criteria, ϵ is the selection efficiency within the acceptance, and L is the integrated luminosity.

The combined efficiency, $A \times \epsilon$ is estimated using the Monte Carlo simulation which is corrected with a scale factor ρ to account for the difference between the efficiency in the data and Monte Carlo:

$$A \times \epsilon = A \times \epsilon_{MC} \times \rho \quad (5.2)$$

where, $A \times \epsilon_{MC}$ is the total selection efficiency estimated from the Monte Carlo. Section 5.4 gives an overview of event selection efficiencies and corresponding scale factors. Once the event selection is applied to the data, number of events in the signal region (N_{data}) are counted and the events from SM expectation (N_{BG}) are estimated in Section 5.5. $A \times \epsilon_{MC}$ calculation is discussed in Section 5.7 followed by the systematics discussion in Section 5.8. Having all the necessary inputs, the results are interpreted in the last Section 5.9 as cross-section measurement of $Z(\nu\bar{\nu})+\gamma$ and limits on ADD model of large extra dimensions.

5.1 Signal

The signal samples are produced with PYTHIA8 [63] generator interfaced within the framework of CMS software (CMSSW). It includes the implementation of the photon + graviton production via contact interaction as well as gauge mediation as shown in Figure 1.1.

In this analysis the number of large extra dimensions (n) from $n = 3$ up to $n = 6$ for M_D values of 1 TeV, 2 TeV and 3 TeV has been considered. Events are generated at a center of mass energy 7 TeV. The cross section for these points of the parameter space are given in Table 5.1. Very low p_T signal events will have large contamination from the irreducible $Z(\nu\bar{\nu})+\gamma$ background. Therefore, the samples are generated with relatively high p_T requirement on the photon using a generator level cut: $p_T^\gamma > 130$ GeV. The simulation and reconstruction of the signal sample are done using CMSSW which

n	$\sigma(\text{pb})$ for M_D value of		
	1 TeV	2 TeV	3 TeV
3	0.094	0.0072	0.00106
4	0.109	0.0062	0.00069
5	0.135	0.0057	0.00047
6	0.176	0.0050	0.00033

Table 5.1: Total signal cross-sections, in pb, for the signal for different model parameters calculated by PYTHIA8 with a lower value on Photon p_T of 130 GeV.

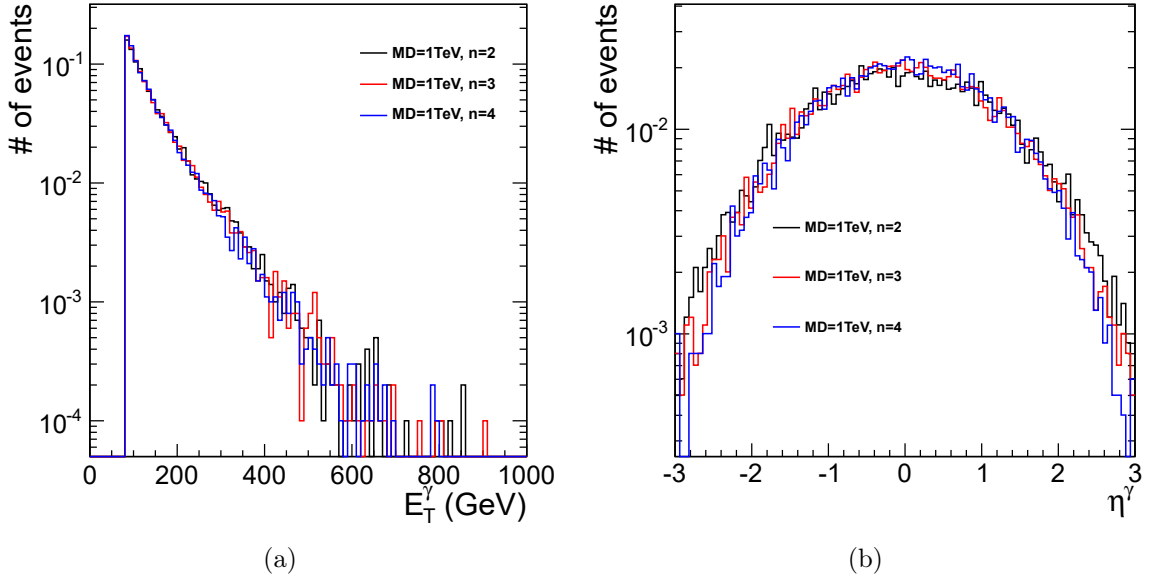


Figure 5.2: Kinematic distributions for the photon at the generator level: (a) photon p_T distribution, (b) photon η distribution. Histograms are normalized to unity.

implements detector simulation using GEANT4.

The distributions in Figure 5.2 show that kinematics of the photon does not change as number of extra dimensions change.

PYTHIA calculates the cross-sections at leading order (LO). However at the LHC, next-to-leading order (NLO) QCD contributions play a significant role. Thus, the cross-sections have been scaled to next-to-leading order cross-sections using BAUR [64] matrix element generator. K-factors, ratio of NLO-to-LO cross sections are used to correct LO cross sections from PYTHIA and are summarized in Table 5.2. They are calculated for photon $p_T > 145$ GeV, $|\eta^\gamma| < 1.4442$, $E_T^\gamma > 130$ GeV and without jet and track veto as the base selection as described in section 5.3.

n	$M_D = 1.0$ TeV	$M_D = 1.2$ TeV	$M_D = 1.4$ TeV	$M_D = 1.6$ TeV	$M_D = 1.8$ TeV	$M_D = 2.0$ TeV
3	1.82	1.70	1.61	1.54	1.49	1.45
4	1.66	1.55	1.46	1.40	1.34	1.30
5	1.56	1.46	1.38	1.31	1.26	1.22
6	1.48	1.38	1.31	1.25	1.21	1.17

Table 5.2: K-factors as a function of M_D and number of extra dimensions n .

5.2 Backgrounds

Various physics processes and non-collision phenomena that constitute the backgrounds are grouped into categories based upon how they are treated.

Non-collision phenomena are a serious background to this analysis which relies on a limited number of final state particles. These can be sub-divided into three categories:

- Electromagnetic showers induced by beam halo muons.
- Spikes in the ECAL.
- Showers induced by bremsstrahlung photon from cosmic ray muons in the ECAL.

There are a few collision generated processes with sizable cross section for which data-driven techniques are used to estimate their contribution. These are:

- QCD multi-jet events that can contribute to the background if a jet fakes a photon and additional hadronic activity is mismeasured yielding E'_T .
- $W \rightarrow e\nu$ events in which the electron is reconstructed as a photon.

Finally, to estimate backgrounds from a variety of physics processes, MC simulations are used:

- $Z(\nu\bar{\nu}) + \gamma$, the main irreducible background from SM.
- $W \rightarrow \mu\nu$ events in which the muon produce a hard photon through bremsstrahlung.
- $W \rightarrow \tau\nu$, with $\tau \rightarrow e\nu_\tau\bar{\nu}_e$
- $W \rightarrow \tau\nu$, with $\tau \rightarrow$ hadrons, especially a π^0 meson.
- $W(l\nu)\gamma$ production where the charged lepton is lost.
- $\gamma +$ jets events if the jet is mismeasured yielding E'_T .
- $\gamma\gamma$ events if one of the γ escapes the detection.

All the samples used for the analysis and their details have been listed out in Appendix A.

5.3 Event Selection

In the signal topology, a single photon is expected depositing its energy in the ECAL. To select such events in the data, the event sample is extracted from single photon triggers. The triggers used for this analysis are listed in Table 5.3, along with the corresponding integrated luminosity for each trigger. As instantaneous luminosity increased, the single photon trigger threshold increased in order to control the trigger rate. To account for this change, an offline p_T threshold is chosen such that it is above the highest trigger threshold. At least one photon object with p_T of at least 145 GeV is required. High p_T photons are reconstructed based on the clusters (formed by super-clustering algorithms) from the crystals within the ECAL as discussed in detail in section 3.3. The photon is also required to be in the barrel fiducial region of the detector ($|\eta| < 1.4442$).

Trigger	Integrated Luminosity (pb^{-1})
HLT_Photon75_CaloIdVL_v1	5.962
HLT_Photon75_CaloIdVL_v2	40.69
HLT_Photon75_CaloIdVL_v3	168.2
HLT_Photon125_v1	120.1
HLT_Photon125_v2	535.3
HLT_Photon135_v1	1150.
HLT_Photon135_v2	2974.
Total	4994.

Table 5.3: Integrated luminosity by trigger.

Each event is required to pass good vertex quality criteria and have atleast one good primary vertex where it is required to have atleast four degrees of freedom from the vertex fit (section 3.2.1). The vertex is required to be within the luminous region ($|z| < 24$ cm) and within the radius of the beam pipe ($\rho < 2$ cm). Additionally, for events with more than 10 tracks, 25% of them are required to be of good quality. This selection removes “scraping” events¹.

A jet can be misidentified as a photon when a neutral particle such as π^0 (or η) within the jet carries a significant fraction of the p_T and the photons from its subsequent decay are collimated such that they appear as a single photon in ECAL. To minimize the contribution coming from mismeasured jets requirements are placed on the isolation variables and shower width. The values of these cuts have been chosen to maximize signal efficiency and background rejection. These requirements are [66]:

- Ecal Isolation: Sum E_T of the ECAL RecHits within a hollow cone of $0.06 < \Delta R <$

¹ Events with fewer than 10 tracks or less good quality tracks could be coming from scraping events which come due to the off beam component, which on interaction with the beam pipe produce a stream of charged particles in the detector [65].

0.40 about the super-cluster, excluding a strip in η of 0.04, is required to be less than $4.2 + 0.006 \times p_T^\gamma$.

- Hcal Isolation: Sum E_T of the HCAL towers within a hollow cone of $0.15 < \Delta R < 0.40$ about the super-cluster is required to be less than $2.2 + 0.0025 \times p_T^\gamma$.
- Track Isolation: Sum of p_T of tracks in a hollow cone of $0.04 < \Delta R < 0.40$, excluding a strip in η of 0.015, about the super-cluster is required to be less than $2.0 + 0.001 \times p_T^\gamma$.
- HadronicOverEM: The hadronic energy within $\Delta R < 0.15$ about the photon super-cluster divided by the electromagnetic energy in the super-cluster should be less than 0.05.
- $\sigma_{i\eta i\eta}$: The width of the shower in $i\eta$ -space is required be less then 0.013. The shower shape variables are defined as:

$$\sigma_{\alpha\beta}^2 = \frac{\sum_{i=1}^n (\alpha_i - \bar{\alpha}_{seed})(\beta_i - \bar{\beta}_{seed})w_i}{\sum_{i=1}^n w_i}, w_i = \max \left(0, 4.7 + \ln \left(\frac{E_i}{E_{5 \times 5}} \right) \right) \quad (5.3)$$

where, $\sigma_{\alpha\beta}$ is defined in $i\eta - i\phi$ space ($\alpha, \beta = i\eta, i\phi$). Here, i runs over each of the crystals within a 5×5 array of crystals centered around the seed of the super-cluster. w_i are energy weighted factors where E_i is the energy of each crystal and $E_{5 \times 5}$ is the energy of 5×5 array of the seed cluster. These variables characterizes the shape of the electromagnetic shower in transverse plane of $i\eta - i\phi$ helping to identify if the profile is similar to the photons coming from the collision vertex.

Figure 5.3 shows the distributions for all the isolation variables for signal photon compared to jets that fake photons coming from QCD background. While making the distributions all other cuts have been applied except the variable being looked at, these distributions are referred to as “N-1” plots.

Electrons are identified from super-clusters in the ECAL using the information from tracker. Therefore, electrons may be misreconstructed as photons due to inefficiency in the track reconstruction. To clean the sample from single electron events, if an event has hits in the pixel layer of the tracker which are compatible with the track of an electron extrapolated from candidate super-cluster in ECAL (termed as matching pixel seed) the event is vetoed. The selection criteria that distinguishes photons from jets and from electrons collectively are referred to as the “Photon Identification” criteria.

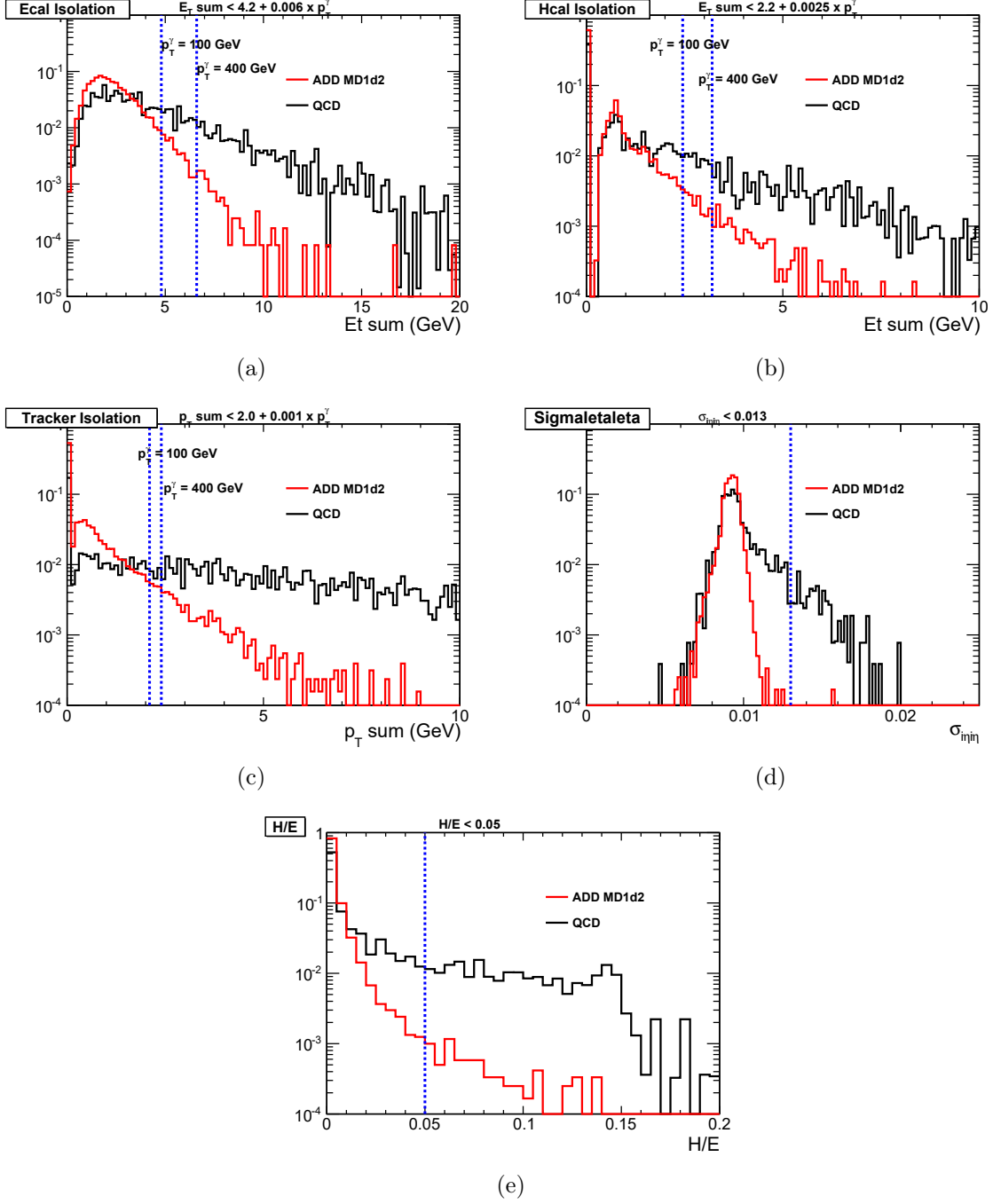


Figure 5.3: N-1 distributions for all the isolation variables a) ECAL isolation, b) HCAL isolation, c) Tracker isolation, d) HadronicOverEM and e) σ_{inn} .

To deal with the non-collision backgrounds from cosmics, halo, and anomalous calorimeter signals, the events are required to pass these criteria:

- Non Spike:
 - $\sigma_{i\eta i\eta} > 0.001$
 - $\sigma_{i\phi i\phi} > 0.001$
 - The largest intracluster time difference (LICTD) between crystals with more than 1 GeV deposited must have an absolute value less than 5 ns
 - ratio of the energy of the 3x3 array of crystals centered on the seed crystal to the energy of the super-cluster , $R9 < 1$
- Non Cosmics/Halo:
 - Seed crystal time is required to be within 3 ns (± 3 ns around the 0 ns of ECAL is prompt).
 - Events are rejected if a CosmicMuon² is reconstructed in the muon detectors. This discriminates against both cosmic ray bremsstrahlung and beam halo muon bremsstrahlung.

Track isolation is a measure of hadronic activity in the tracker around the direction of the photon candidate. It is computed using tracks which originate from the primary vertex, assigned as the origin for the photon. In higher pileup environment, the probability of assigning a wrong vertex is high, leading to a bias towards smaller value of this quantity. Thus an additional track isolation is computed in the same manner, but with respect to each vertex in the event. The largest value of this isolation is required to be smaller than the track isolation threshold, thus ensuring that this electromagnetic object is indeed isolated from any charged hadron activity within the event.

Events are required to have $E_T' > 130$ GeV. The E_T' present in the event is calculated based on the algorithm discussed in Ref [46].

To minimize the contribution from $W\gamma$, $Z\gamma$ and γ +jet events an event is vetoed if there is a jet reconstructed with p_T above a p_T threshold of 40 GeV within $|\eta| < 3.0$. An event is also vetoed if there is a track with p_T above 20 GeV that is $\Delta R > 0.04$ away from the photon candidate. These are referred to as the jet and track vetoes.

Figure 5.4 shows the highest p_T^γ candidate event. An isolated deposit in the ECAL layer of the CMS detector corresponds to a photon with $p_T=384$ GeV along with a minimal activity present in the event.

²CosmicMuon refers to the reconstructed muons in which the individual segments within the muon system are not required to be projective.

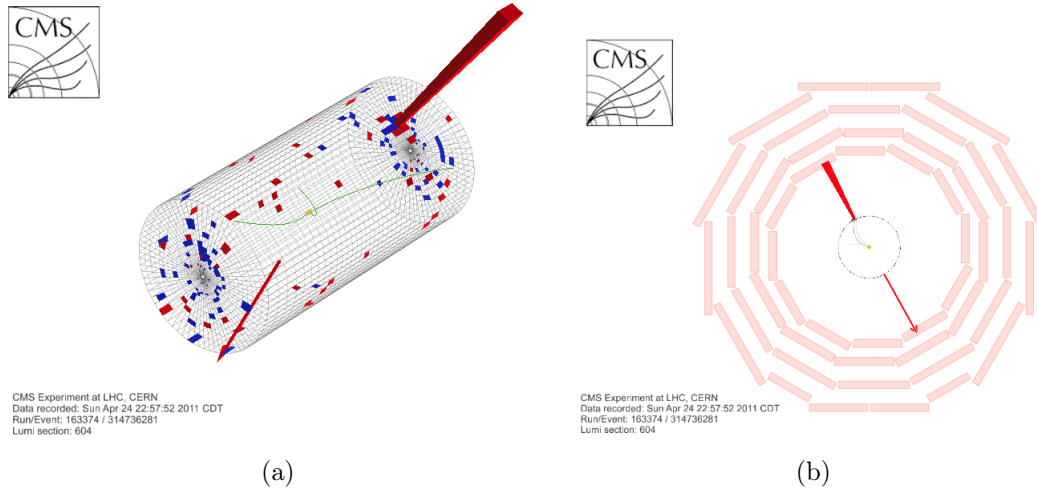


Figure 5.4: An event display for the highest p_T^γ event in 5 fb^{-1} of data in a) Cylindrical and b) X-Y view.

The event selection is optimized (discussed in Appendix B) to improve the ADD search sensitivity i.e., to provide the lowest value for the expected upper limit on ADD cross section at 95% CL.

5.4 Selection Efficiencies

5.4.1 Trigger selection

All the triggers listed in Table 5.3 use the same L1 trigger as L1SingleEG20, which fires if an L1 electromagnetic object above an E_T threshold of 20 GeV raw energy is present in the event. Since the offline threshold is 145 GeV, it has been assumed that the full L1 efficiency is attained before the HLT selection itself is applied. At the HLT, three selections are used: an E_T threshold (75, 125, and 135 GeV respectively for triggers), loose isolation cuts (looser than the offline selection), and a very loose selection on shower shape³ noted by “CaloIdVL”. The shower shape selection⁴ is enough to include a sizeable amount of beam halo for which showers are typically twice as wide in η compared to the width expected from electromagnetic objects, it is reasonable to assume that it is fully efficient.

However, to estimate the turn-on due to threshold, prescaled backup triggers with the same selection criteria (CaloIdVL) that were run concurrently with the unprescaled triggers are used. This allows to observe the turn on curve for the trigger at HLT by measuring the efficiency with respect to the lower threshold trigger. Tight photon candidates

³Here, shower shape refers to $\sigma_{i\eta i\eta}$ as defined earlier

⁴The actual value of the cut at HLT in the barrel is 0.024.

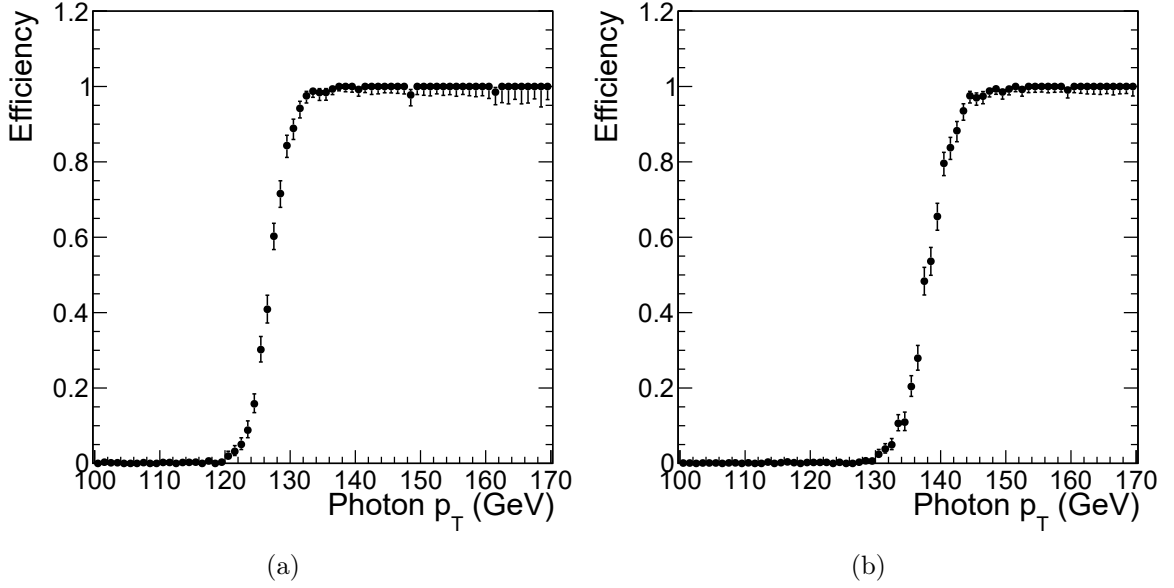


Figure 5.5: Efficiency of single photon trigger a) (HLT_Photon125) and b) (HLT_Photon135)

in events that explicitly pass the lower threshold triggers form the denominator while how many of these events fire the unprescaled signal trigger form the numerator. The trigger efficiency for the HLT paths HLT_Photon125 and HLT_Photon135 is plotted as a function of photon p_T in Figures 5.5a and 5.5b. Full efficiency is reached for $p_T > 145$ GeV with respect to the offline threshold.

5.4.2 Photon identification

To estimate the photon identification efficiencies in data, “tag-and-probe” technique has been used with $Z \rightarrow e^+e^-$ events since the photon selection identification quantities have similar efficiency for electrons and photons. Thus any relevant data effects should be visible in clean samples of Z boson decays and allow for a correction to the photon MC.

In this method, one of the electrons is required to pass the tight photon requirements, trigger requirement and should have an associated track. This electron is called as the “tag” electron. However, other electron called as “probe”, is required to have either a track or a super-cluster. Then, two different invariant mass distributions for tag and probe pairs are fit to Z peak. In one case the probe passes the identification criteria and in another case it fails. The distributions are fitted using the convolution of a Breit-Wigner and a Crystal Ball function for signal and a “exponential decay + error” function for the background. Efficiency is estimated for both data and MC as 0.848 ± 0.011 and 0.879 ± 0.006 respectively. Thus, the scale factor (their ratio as Data/MC) corresponding to

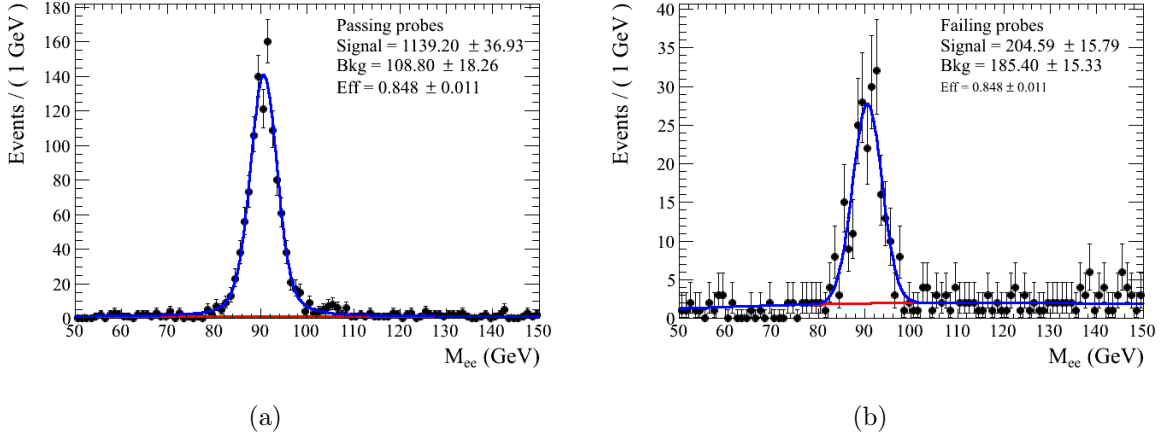


Figure 5.6: Invariant mass and fits for tag and probe method applied to data [68].

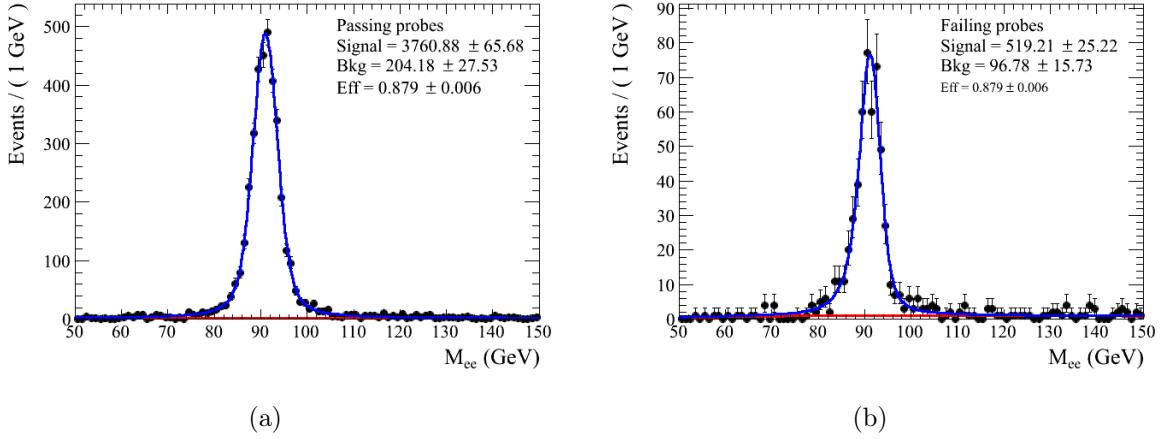


Figure 5.7: Invariant mass and fits for tag and probe method applied on Monte Carlo [68].

identification criteria used is measured to be 0.96 ± 0.02 [67].

5.4.3 Embedded spike removal

Anomalous calorimeter signals may be “embedded” within the clusters of energy formed by prompt photons from collisions. To ensure the energy deposition within the cluster is consistent with the prompt photons both in pattern and timing, the crystals with energy greater than 1 GeV which are clustered into our photon candidate are required to be within 5 ns of the seed crystal’s time.

$Z \rightarrow e^+e^-$ candidate sample is used to calculate the efficiency of the LICTD cut. The candidates pass the regular candidate selection criteria except here a pixel seed is required. $|LICTD| < 5$ ns cut is imposed to calculate the ratio of events in the sample that pass the requirement to the entire sample. This yields an efficiency of $98.3\% \pm 0.9\%$. Since

the MC is fully efficient, ϵ is equal to the $\frac{\text{data}}{\text{MC}}$ scale factor ρ . The result is cross-checked with $W e \nu$ sample and a good agreement is found between the two.

5.4.4 Veto efficiency

Three vetoes are studied: vetoes on reconstructed cosmic muons, jets $p_T > 40$ GeV within $|\eta| < 3.0$, and tracks $p_T > 20$ GeV that are $\Delta R > 0.04$ away from the photon candidate object. Since the jet and track vetoes both remove events with jet activity, these vetoes are correlated. Therefore, the efficiency of vetoing an event that has jets or tracks (Trk+Jet efficiency) is computed together.

The efficiency of event vetoes are studied from ($W \rightarrow e \nu$) and $Z(\nu \bar{\nu}) + \gamma$ samples. $W \rightarrow e \nu$ Monte Carlo and data events are selected in a manner identical to the monophoton sample with the exception that a pixel seed is required to identify the electron. Table 5.4 shows the veto efficiency for both the samples in data in Monte Carlo.

Efficiency	$W e \nu$ MC	$W e \nu$ Data	$Z \nu \bar{\nu} \gamma$ MC	Cand Data
CosMu Eff.	0.90 ± 0.17	0.89 ± 0.05	0.94 ± 0.04	0.60 ± 0.09
Trk+Jet Eff.	0.45 ± 0.07	0.49 ± 0.02	0.70 ± 0.03	0.33 ± 0.05

Table 5.4: N-1 efficiencies

For the cosmic muon efficiency, it is observed that candidate data sample for $Z(\nu \bar{\nu}) + \gamma$ has a lower efficiency than in MC. It is expected because cosmic muons are not simulated in MC. But, the same pattern is not seen for the case of $W e \nu$ MC and data. This can be understood by the fact that in $W \rightarrow e \nu$ candidate sample, the requirement of the pixel seed helps to eliminate cosmic muon bremsstrahlung events that occur in data. Thus, $Z(\nu \bar{\nu}) + \gamma$ candidates are more susceptible to have cosmic contamination than the $W \rightarrow e \nu$ candidates because there is no pixel seed requirement for monophoton events. Further, the efficiency of vetoing only on the cosmic muons is studied using the much larger statistics of a data $Z \rightarrow e^+ e^-$ sample. The $Z \rightarrow e^+ e^-$ candidates are selected by requiring two tight photons with $p_T > 30$ GeV. The super-clusters of the two photons are required to have matching pixel seeds in the pixel layer of the tracker. Jet and track vetoes as described in 5.3 are applied to these events. The efficiency is measured to be 89.9% in data and 94.3% in MC respectively, producing a data-to-MC efficiency scale of 0.95 ± 0.01 for vetoing on the cosmic muons.

The Trk+Jet efficiency discrepancy between $W \rightarrow e \nu$ and $Z(\nu \bar{\nu}) + \gamma$ is expected because typically the W is recoiling against a jet, whereas the Z is recoiling against the photon. This means there are more events eliminated with a jet veto in the W sample compared to the Z sample. With this taken into account, the data to MC scale factor for jet and track veto is being taken as 1.0 ± 0.1 with the conservative assignment of 10% uncertainty.

The difference in efficiencies between data and MC are summarized in Table 5.5. The combined value of the scale factor, ρ is 0.90 ± 0.11 with contributions from the trigger, photon reconstruction and the vetoes. This scale factor is used to scale the MC simulated backgrounds to correct for the differences observed in efficiencies between the real and simulated events.

Source	Estimate for ρ
Trigger	1.00 ± 0.02
Large Intra Cluster Time Difference	0.983 ± 0.009
Photon Efficiency	0.96 ± 0.02
Jet and track veto	1.00 ± 0.10
Cosmic muons veto	0.95 ± 0.01
Total	0.90 ± 0.11

Table 5.5: The difference in the efficiencies between data and Monte Carlo simulation.

5.5 Backgrounds estimates using Monte Carlo

The following SM backgrounds are estimated using MC: $Z(\nu\bar{\nu})+\gamma$, $W(l\nu)\gamma$, $\gamma + \text{jets}$ and $\gamma\gamma$. All estimates are based on full detector simulation and include pileup conditions. $Z(\nu\bar{\nu})+\gamma$ is the largest background that contributes to this analysis. Its contribution is estimated using LO generator PYTHIA. The cross-section as well as the shape of the differential p_T distribution has been studied upto NLO QCD using BAUR [68]. To understand NLO contribution passing our selection criteria, k-factor is calculated for : $p_T^\gamma > 145$ GeV, $|\eta^\gamma| < 1.4442$, $E_T' > 130$ GeV, $|\eta^\nu| < 5$, and $|\eta^{jet}| < 3$. The resulting global k-factor is 1.19. Here, the NLO events are generated using the CTEQ66 PDF and the LO events are generated with the CTEQ6L1 PDF. However, sensitivity of the k-factor to the choice of PDF is calculated as PDF uncertainty of ± 0.05 . Additional uncertainty due to the choice of factorization and renormalization scale is calculated as ± 0.05 and ± 0.02 respectively. The total number of the $Z(\nu\bar{\nu})+\gamma$ events contributing to the event sample from data is estimated to be 45.3 ± 7.4 events.

With a total cross-section of 7.9 nb at 7 TeV at the LHC, $W \rightarrow l\nu$ is one of the important backgrounds to be studied in this analysis. The relative contributions are estimated from the possible ways in which the $W \rightarrow l\nu$ gives a high E_T' event with a high p_T photon in the final state. The W to lepton decay has a real source of E_T' and contributes to the background if charged lepton is lost and an ISR or FSR photon reaches the detector. Most of the background estimated with MC is attributed to ISR while the FSR contribution from W is small. The FSR contribution is estimated using a high \hat{m}

sample ($\hat{m} > 200$ GeV) of $W \rightarrow l\nu$ events from PYTHIA. To avoid double counting from electrons faking photons, the electron is required to be soft ($p_T < 50$ GeV) after the FSR emission at the generator level. An FSR photon is misidentified as a monophoton candidate only when the electron from a very high mass offshell W decay, loses most of its energy to the emitted FSR photon. For the cases, where electron can possibly fake a photon is separately considered as a background discussed in 5.6.2.

Diphoton events can fake our signal if one of the photons escapes detection, giving rise to fake E_T and a real photon. The $\gamma + jets$ process at the LHC has a large cross section and can fake our signal if either

- the jet is misreconstructed, giving rise to fake MET, and the real photon is detected, or
- the real photon escapes the detector, giving rise to fake MET, and the jet fakes a photon.

While the contribution from the latter case is included in the data-driven estimation section of background events where a jet is misidentified as a photon (section 5.6.1), the contribution from the former case is estimated using a PYTHIA-based MC sample. To avoid double counting with the data-driven estimate of the jet faking photon background, MC events are subtracted where the photon candidates do not originate from the hard scattering.

The total estimated number of events originating from the electron, muon, and the tau final states of W decays, as well as those from the diphoton and γ +jet channels, that pass all cuts are reported in Table 5.10. These numbers here are reported without pile-up re-weighting discussed below.

	Vertex	Scraping	Non Cosmics	MET	Photon ID & p_T^γ & $ \eta^\gamma $	Track Iso	Jet Veto	Track Veto	HLT	events in 5.0 fb ⁻¹
W+ γ	0.999	0.999	0.591	0.002	8.19e-05	7.62e-05	1.41e-05	1.22e-05	1.22e-05	4.27 ^{+1.74} _{-1.16}
W $\rightarrow e\nu$	0.998	0.998	0.992	0.236	0.0085	0.0069	0.0048	0.0032	0.0032	0.36 ^{+0.13} _{-0.10}
W $\rightarrow \mu\nu$	0.997	0.997	0.116	0.014	0.000	0.000	0.000	0.000	0.000	0.00 ^{+0.05} _{-0.0}
W $\rightarrow \tau\nu$	0.999	0.999	0.780	0.124	0.018	0.015	0.0092	0.0083	0.0083	0.26 ^{+0.12} _{-0.08}
Diphoton	0.999	0.999	0.923	0.010	0.0069	0.0066	0.0017	0.0012	0.0012	0.54 ^{+0.60} _{-0.27}
γ +Jet	0.998	0.998	0.750	0.012	0.0060	0.0058	6.20e-07	3.38e-07	3.38e-07	0.63 ^{+0.58} _{-0.29}

Table 5.6: Cumulative efficiencies of the background processes after successive analysis cuts and in the last column it shows the total number of events from every background at 5.0 fb⁻¹.

5.5.1 Rescaling of MC for pileup distribution

In high-luminosity colliders, multiple interactions per bunch crossing affects the reconstruction efficiency. To simulate the presence of these pile-up events in Monte Carlo

simulation, the hard scattered interactions are overlayed with a number of minimum bias interactions. However, the number of these artificial interactions in the simulation does not match the data profile for a given run period. In this analysis, all Monte Carlo events have been re-weighted for this effect. The re-weighting procedure takes into account the true number of pile up interactions per bunch crossing giving an agreement between data and simulated pile-up vertices. Measured inelastic total cross section is used to obtain the pileup profile for data. The uncertainty in the measured inelastic total cross section is propagated to the acceptance calculation. The implementation of this procedure is described in detail in [69].

5.6 Data-driven estimates

5.6.1 Jet fakes photon background

Any analysis involving final state photons is contaminated with “fakes” from QCD multijet and dijet events. Specifically, these “fakes” occur when one of the high E_T jets fragments mainly into isolated neutral pions or η s which decay to two photons. These photons are sufficiently collimated to appear as a single electromagnetic shower in the ECAL.

The rate at which hadronic activity from jets will pass the photon selection criteria is $\sim 10^{-3} - 10^{-4}$. Though this rate appears small, the QCD production cross section is large enough compared to $Z(\nu\bar{\nu}) + \gamma$ production to provide a potentially important background.

The jet faking photon rate is estimated directly from the data to avoid the dependence from the shower modelling in MC. A sample of fake photons that are kinematically similar to our candidate events is used to estimate the fake ratio and fake ratio is then applied to provide a normalized estimate of the background.

True fake ratio is defined as the ratio of EM-like jets passing the photon selection to the number of EM-like jets passing a “loose”⁵ photon selection. It is obtained in two steps. In the first step, a raw fake ratio is obtained as the ratio of number of events with a object that pass the photon selection criteria to the objects that fails any of the isolation criteria and are loose photons. In the second step, fraction of true isolated photons in the numerator sample is estimated and subtracted to identify the true fake ratio.

To measure the raw fake ratio, a control sample from the data is used in which an event is required to have a photon object with $p_T > 145$ GeV but with $\cancel{E}_T < 20$ GeV and no vetoes on tracks or jets. In this sample, the photon objects that pass the photon identification criteria used the candidate events form the numerator. However, the denominator selection is kept “loose” to select the “fakes” as below:

⁵thresholds on the isolations are loosened to ensure the object is a jet

- Ecal Isolation $> 4.2 + 0.006 \times p_T^\gamma$
- Hcal Isolation $> 2.2 + 0.0025 \times p_T^\gamma$
- Track Isolation $> 3.5 + 0.001 \times p_T^\gamma$

as well as very loose photon selection requirements:

- Ecal Isolation $< \min [5.0 \times (4.2 + 0.006 \times p_T), 0.2 \times p_T^\gamma]$
- Hcal Isolation $< \min [5.0 \times (2.2 + 0.0025 \times p_T), 0.2 \times p_T^\gamma]$
- Track Isolation $< \min [5.0 \times (3.5 + 0.001 \times p_T), 0.2 \times p_T^\gamma]$
- HadronicOverEM < 0.05
- $\sigma_{i\eta i\eta} < 0.013$
- No pixel seed

Figure 5.8a shows the distribution of for selected photons in numerator and denominator.

To remove the contamination from real photons in the numerator, a fit is performed using binned likelihood estimator [70] with shower shape templates in $\sigma_{i\eta i\eta}$ from data and Monte Carlo. For the real photons γ +jet MC is used. For the fake template, a sample from data is used with an EM cluster present in it. Here, the events are selected by choosing events within a side-band of track isolation (tracks p_T sum around the direction of photon) as:

- $(2.0 + 0.001 \times p_T) < \text{Track Isolation} < (4.0 + 0.001 \times p_T)$

The fake template is dominated by QCD-multijets. To estimate the fraction of real photons, the shower-shape templates fitting is done for various p_T bins. Figure 5.8b shows the result of the template fitting in one such p_T bin.

Figure 5.8c shows the true fake ratio corrected from the real photons [68]. True fake ratio is parametrized in the following form as a function of p_T :

$$f_{p_T^\gamma} = 0.2551 - 2.406 \times 10^{-3} p_T^\gamma + 1.323 \times 10^{-5} p_T^{\gamma^2} \quad (5.4)$$

Once the true fake ratio is estimated, an estimate on the number of jets faking photons is made. A sample is chosen from the data which satisfies all other cuts of the analysis but not the candidate photon identification selection. This candidate photon identification selection is replaced by the selection criteria for denominator type photons taken in the

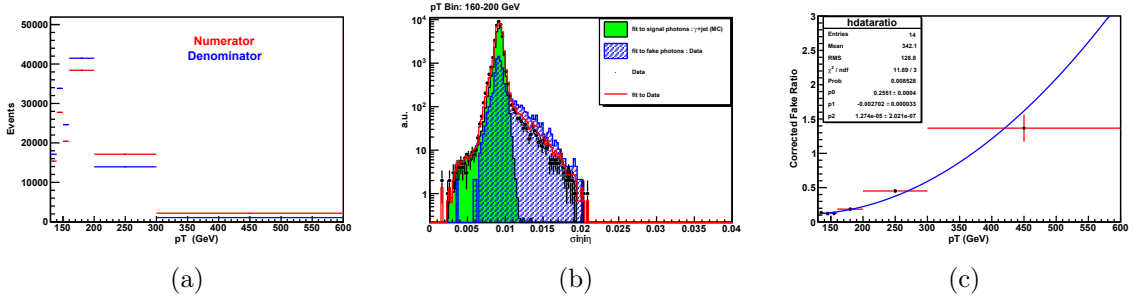


Figure 5.8: a) events selected in numerator (red) and denominator (blue) for the raw fake ratio b) a template distribution for σ_{inj} and fits to QCD and true photon components in p_T bin of 160 to 200 GeV. c) True fake ratio ratio as a function of p_T [68].

fake ratio. If $N_{deno}(p_T)$ is the number of such events at a given p_T , then estimated jet faking photons at the p_T is given by :

$$N_{fake}(p_T) = f_{p_T}^{\gamma} * N_{deno}(p_T) \quad (5.5)$$

This is done on event by event basis. The estimated total number of QCD events is 11.15 ± 3.75 . A conservative systematic uncertainty of 30% has been assigned with many factors taken into account. These include 1σ variation of the various the fit parameters in the fake ratio, systematics due to the different choices of sideband selection and bins size of the shower shape templates.

5.6.2 Electron faking photon background

Electrons can be misidentified as photons if a pixel seed matching with the super-cluster in the ECAL is not found. The largest of these backgrounds would be from $W \rightarrow e\nu$ events, in which the W boson is produced far off-shell yielding an electron plus E_T signature identical to our signal events.

The pixel match efficiency has been measured elsewhere [71] to be 0.9940 ± 0.0025 , and has been found to be constant as a function of p_T . A sample of electron candidate events in the data with an event selection identical to that of the monophoton candidate events is selected, except the pixel seed is required instead of vetoed. This gives an estimate of the number of electron events with similar kinematics to our candidate events in data. This is divided by the pixel match efficiency to extrapolate back to the true number of electron events in the data. This number of events is then weighted by the pixel match inefficiency (see equation 5.6) to give an estimate of the number of these electron events

which would “leak” into our candidate sample.

$$N_e = N_{pixmatch} \times \frac{(1 - \epsilon)}{\epsilon} \quad (5.6)$$

The total number of pixel matched candidate events is 583. When properly weighted, this yields an estimated 3.52 ± 1.48 events.

5.6.3 Non-collision backgrounds

Since none of the non-collision processes (cosmics/spikes/halo) are well modelled by Monte Carlo, an estimate is made for their contribution in the candidate sample using the timing distribution⁶ and a series of templates using data.

Spikes template: Spikes are typically removed from the candidate sample through both timing and nature of the topology of the cluster. To estimate the in-time contribution, a time template for anomalous signals is made. R9 cut is implemented in the selection criteria to identify these signals. Thus, here instead of selecting on showers looking like an EM shower, this requirement on R9 is reversed ($R9 \geq 1.0$) to provide a timing distribution for spikes shown in Figure 5.9a.

Beam halo template: To make a halo template, information from HCAL Endcap (HE) is used to form a HE tagger [68, 72]. If this tagger is true for an event along with the event selection vetoes on jet and tracks, it yields a high purity beam halo sample. For an event to pass the HE tagger, it must

- Have a Calo Tower with energy in hadronic endcaps (HE) above an energy threshold (> 1 GeV).
- The Calo Tower must be aligned in ϕ with the cluster in the ECAL ($\Delta\phi < 0.2$).
- The energy deposited in HE is within radial distance of 110 cm and 140 cm
- An isolated Calo Tower in the tracker with tracks p_T sum to less than 2 GeV around it within a cone of 0.4 in ΔR .

The timing distribution is shown in Figure 5.9b.

⁶Whenever the time of the photon object is referred, it is the timing of seed crystal in the cluster.

Prompt template: In order to form the templates for the photons coming from collisions, the same event selection is applied except for the isolation based on the tracker isolation is inverted. Inverting the track isolation ensures the tracker activity which is attributed to originate from collisions. The timing distribution is shown in Figure 5.9c

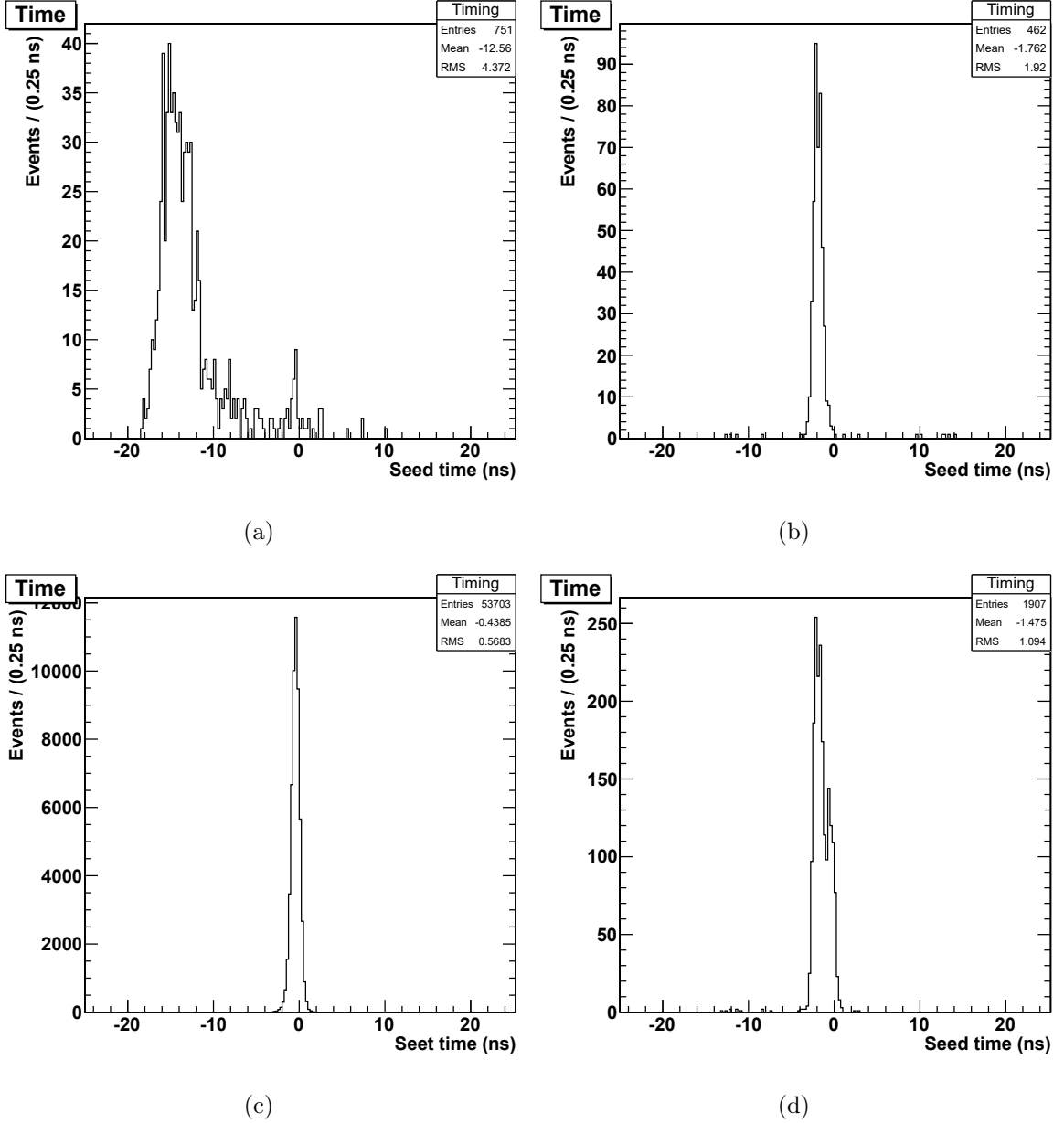


Figure 5.9: Timing distribution of photons for a) spikes, b) tagged as beam halo using the HE tagger, c) prompt photons and d) candidate sample with vetoes. [68]

Estimate in the candidate sample: Figure 5.9d shows the timing distribution for candidate events that pass photon identification requirements except for the timing and shower shape requirement. There is no appreciable contribution from anomalous signals,

or cosmic ray events (which one expects to flat in time).

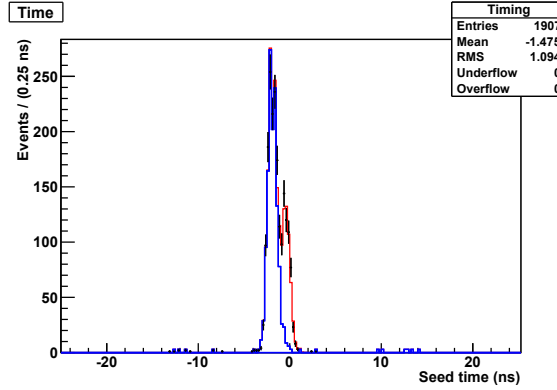


Figure 5.10: Fit of template shapes to candidate timing distribution, shown in both linear and log scales. The contribution in blue is from beam halo and red corresponds to prompt candidates. A contribution due to anomalous signals would have been purple, but the fitter rejected this hypothesis in the candidate sample. [68]

The beam halo contribution is estimated to be 1287 ± 64.9 events in the 3 ns timing window (Figure 5.10b) using the timing templates discussed above.

Original estimation in the candidate sample is done with the shower shape information in. The shower shape distribution for beam halo events is different from that of prompt photons or hadronic jets. From the beam halo sample used to make the timing template, it is expected that beam halo events that pass the shower shape requirement of $\sigma_{i\eta i\eta} < 0.13$ are only 0.87 ± 0.43 percent of the total. Thus, the beam halo contribution to the monophoton event selection is estimated as 11.1 ± 4.6 events.

A detailed study can be found in [68], [73]. The photon p_T spectra and E_T^γ for ADD signals ($M_D = 1$ TeV, $n=3$) and SM backgrounds are shown in Figure 5.11. To ensure there is no bias present due to the vetoes in the selection criteria, the data-MC comparisons are done in the control regions by removing the vetoes as shown in Figure 5.12.

5.7 Acceptance Calculation

$A \times \epsilon_{MC}$ is defined as the ratio of events that pass the selection criteria to the total of generated events.

The $A \times \epsilon_{MC}$ for $Z(\nu\bar{\nu}) + \gamma$ process is estimated as 0.452 ± 0.003 for $E_T^\gamma > 145$ GeV and $|\eta| < 1.4$.

The values for $A \times \epsilon_{MC}$ for ADD signal samples are summarized in Table 5.8, calculated for \hat{p}_T cutoff of 130 GeV at the generator level. The error estimate includes the statistical uncertainty on the estimation due to the limited size of the MC sample.

Source	Estimate	Uncertainty
Beam Halo	11.1	4.6
Jet Fakes Photon	11.2	3.8
Electron Fakes Photon	3.5	1.5
$W\gamma$	3.1	1.1
γ +jet	0.5	0.2
$\gamma\gamma$	0.6	0.3
Total Background to $Z(\nu\nu\gamma)$	30.0	6.3
$Z \rightarrow \nu\nu + \gamma$	45.3	7.4
Total SM Expectation	75.3	9.7
Total Observed	73	-

Table 5.7: Summary of estimated background events and observed candidate events from the data

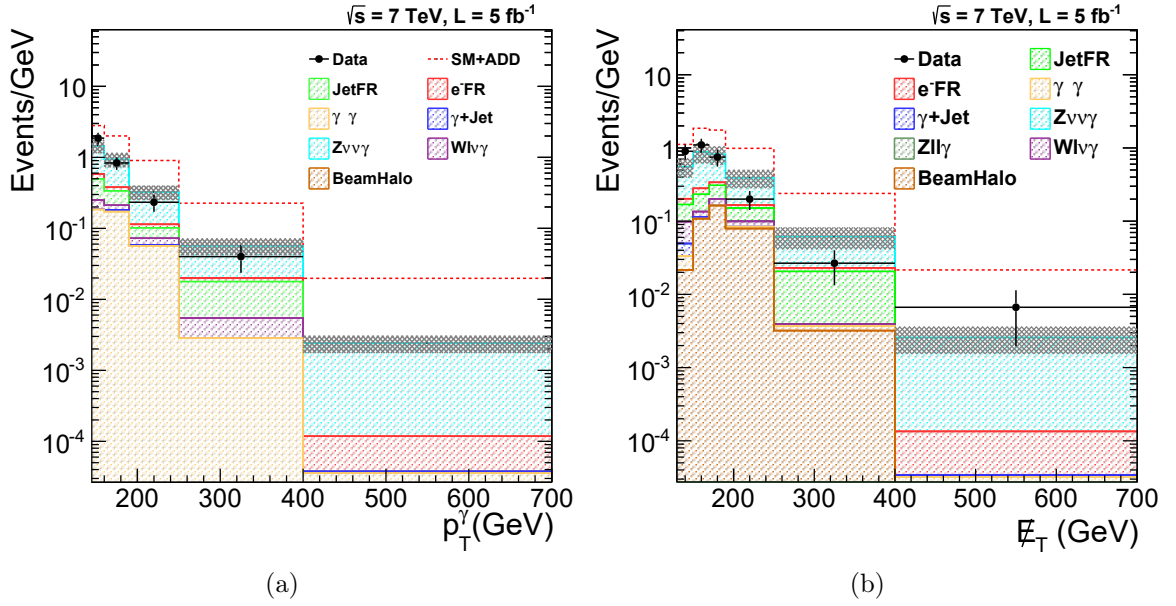


Figure 5.11: Photon p_T spectra and E_T for the Standard Model processes and ADD extra dimensions after the full event selection overlaid with $M_D = 1$ TeV, $n=3$.

M_D (TeV)	$A \times \epsilon_{MC}$			
	n=3	n=4	n=5	n=6
1	0.249 ± 0.004	0.243 ± 0.004	0.249 ± 0.004	0.248 ± 0.004
2	0.239 ± 0.004	0.246 ± 0.004	0.253 ± 0.004	0.267 ± 0.004
3	0.255 ± 0.004	0.255 ± 0.004	0.253 ± 0.004	0.254 ± 0.004

Table 5.8: Calculated $A \times \epsilon_{MC}$ as a function of M_D and n for $\hat{p}_T > 130$ GeV.

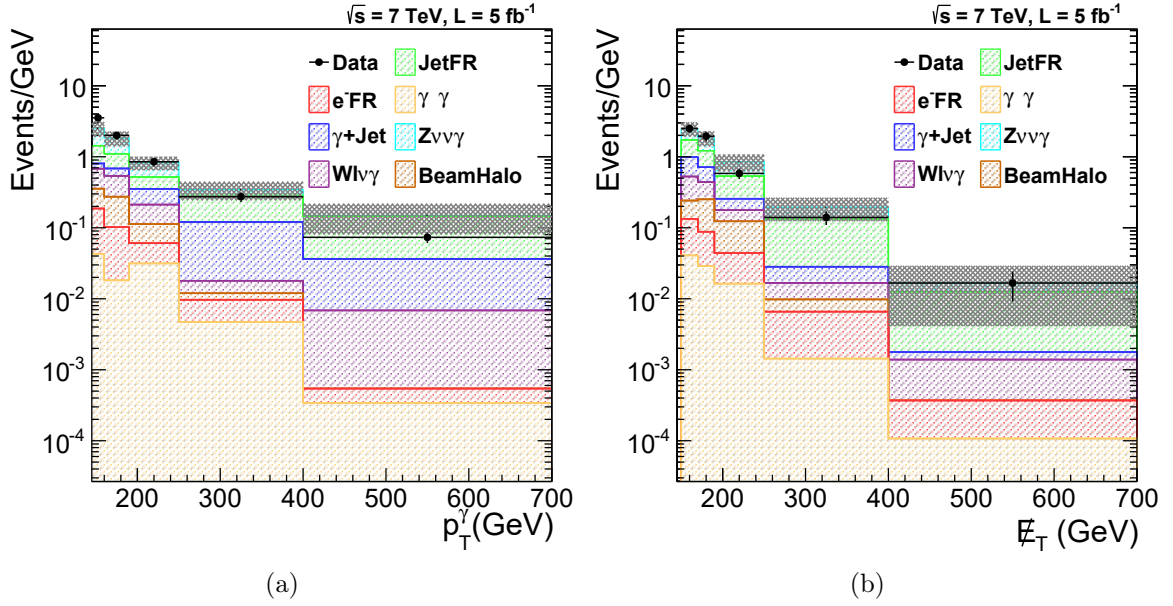


Figure 5.12: Photon p_T and E_T comparison between Standard Model processes and the data in the region where jet and track vetoes are removed.

5.8 Systematics

PDF uncertainty: The theoretical cross section measurement comes from the Monte Carlo event generator which uses a given parton distribution function. This introduces a systematic uncertainty in the cross-section estimation. The Monte Carlo sample for $Z(\nu\bar{\nu})+\gamma$ is generated with PYTHIA using CTEQ6L1 [74] PDF and k-factor is obtained with BAUR MC, which uses the CTEQ61 and CTEQ66 PDF for LO and NLO calculations. The PDF uncertainty is calculated by using different PDF sets, MSTW08LO [75] and CTEQ66 recommended by PDF4LHC guidelines [76, 77]. The observed error in acceptance due to variation in PDF sets is $\pm 2.4\%$ for $Z(\nu\bar{\nu})+\gamma$.

Vertex uncertainty: As mentioned earlier in section 5.3, there is a possibility that candidate photon is associated to a wrong vertex which can affect photon E_T and E_T calculation in the event. To study this, a control sample of $W(e\nu)$ is used from data. Since electrons have both a track and a cluster in ECAL, a track is identified associated with this electron and is excluded knowingly to obtain a new primary vertex for the event with the rest of the tracks. To get a new primary vertex, the sum of the squares of the track p_T (excluding the matched track) is calculated for each vertex in the event, and the one with the maximum track p_T^2 sum is matched to the original primary vertex from the event. In 38% of the events, the primary vertex selected by excluding the electron track is not the one obtained in the event where this electron track information is taken into

consideration.

In these 38% mismatched events, photon E_T is calculated with respect to the newly assigned vertex. The relative difference with the old vertex is found to introduce an additional 2% to the photon transverse energy resolution which is propagated as a systematic uncertainty in the acceptance.

Pile-up uncertainty: As discussed in section 5.5.1, pile-up scenario in MC simulation is different from the data. In order to take this into account, a pile-up re-weighting is done and overall a good agreement is seen between data and MC simulation as shown in Figure 5.13. The corresponding change in acceptance introduces an uncertainty of $\pm 2.4\%$ for $Z(\nu\bar{\nu})+\gamma$.

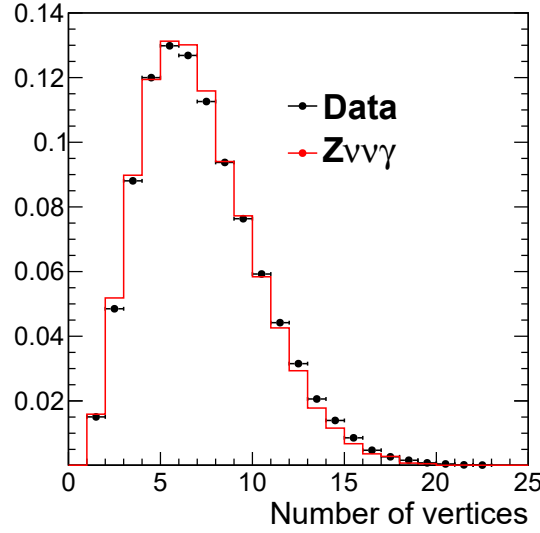


Figure 5.13: Number of vertices for the data and pile up reweighted $Z(\nu\bar{\nu})+\gamma$ sample.

Energy-scale of various physics objects: The uncertainty on the photon energy scale is estimated to be 1.5% based on the final-state radiation measurement with Z [67]. The E_T scale uncertainty is taken as a conservative 5%, based on the estimate derived from the 2010 data [33]. The uncertainty on the E_T resolution is taken as the difference between the MC prediction and the measured resolution in the data, which corresponds to approximately 10%. Jet energy scale uncertainties version 2011V2 are used [78]. Jet energy resolution is scaled up by 10% based on the stretching method described in [79].

A summary of the systematic uncertainties on $A \times \epsilon_{MC}$ is presented in Table 5.9.

Source	Sys error in $A \times \epsilon_{MC}$ [%]	
	$Z(\nu\bar{\nu})+\gamma$	ADD
Energy scale	± 4.3	± 2.7
Photon Vertex	± 0.3	± 0.3
E_T	+1.6-3.1	± 0.4
jet energy scale	± 0.8	+0.9 -1.1
jet resolution +10%	± 0.2	-0.6
Pile-up	± 2.4	± 2.5
PDFs	± 2.4	± 2.9
Total	+5.7 -6.3	+4.8 -4.9

Table 5.9: Systematic uncertainties on $A \times \epsilon_{MC}$ calculation.

5.9 Results

5.9.1 Cross-section measurement for $Z(\nu\bar{\nu})+\gamma$ process

All the input parameters that have been used for the calculation of the cross-section of $Z(\nu\bar{\nu})+\gamma$ process are listed in table

N_{data}	73 ± 8.5
N_{BG}	30.0 ± 6.3
$A \times \epsilon_{MC}$	0.452 ± 0.003
ρ	0.90 ± 0.11
L (fb $^{-1}$)	4.99 ± 0.11

Table 5.10: Summary of the parameters needed for cross-section calculation

The cross-section for $Z(\nu\bar{\nu})+\gamma$ process is measured to be 21.2 ± 4.2 (stat.) ± 4.3 (syst.) ± 0.5 (lumi.) fb using Equation 5.1, for $E_T^\gamma > 145$ GeV and $|\eta| < 1.4$ which is in good agreement with the theoretical NLO prediction of 21.9 ± 1.1 fb [80].

5.9.2 Limits on the ADD model of large extra dimensions

In earlier works on graviton searches at CMS only a number counting experiment has been performed [22]. In this thesis, a study of a shape based limit for graviton search has been presented. As discussed in section 1.3, the shape of the photon p_T distribution varies as a function of MD (also can be seen from figure 5.14). Making use of this additional information, one can construct a more powerful likelihood based test statistic to discriminate between the background only and signal + background hypotheses.

The total number of $\gamma + E_T$ events observed in data, within the kinematic cuts are in agreement with the expected number of events from all the background sources

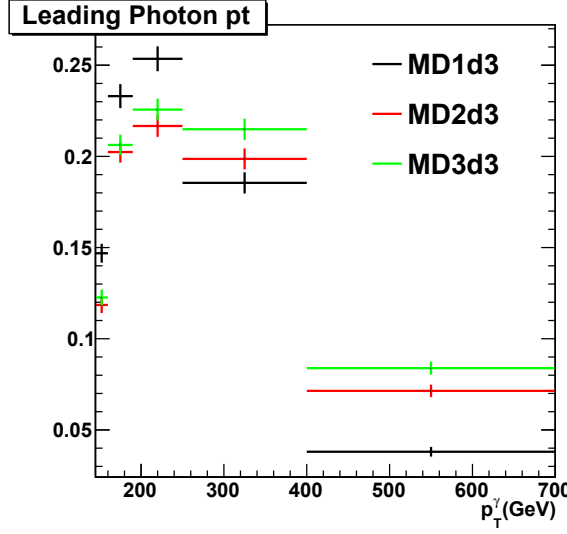


Figure 5.14: Shape comparison of Photon p_T spectrum between various MD values

(SM processes + non collision processes), within the experimental errors. The level of incompatibility of the observed data with “signal + background” hypothesis is quantified using the standard CL_S statistic [81]. It is defined as the ratio of two p-values, $p_{s+b}/1 - p_b$ where,

$$p_{s+b} = \int_{q_{obs}}^{\infty} f(q|s+b)dx \quad \text{and} \quad p_b = \int_{-\infty}^{q_{obs}} f(q|b)dx \quad (5.7)$$

Here, $f(q|\mu)$ is the probability density function for the test statistic q given the hypothesis μ is true. For a number counting experiment the test statistic q is taken as the profile likelihood ratio [82]:

$$q_\mu = -2 \ln \frac{\mathcal{L}(data|\mu, \hat{\theta}_\mu)}{\mathcal{L}(data|\hat{\mu}, \hat{\theta})}, \quad \text{with a constraint } 0 \leq \hat{\mu} \leq \mu \quad (5.8)$$

Here, θ denotes the set of nuisance parameters, on which the background model $b(\theta)$ depends. μ is the parameter of interest (POI). In the profile likelihood ratio in equation 5.8 the numerator is obtained by maximizing the likelihood function within the subspace $\mu=0$. This is the maximization of likelihood under the background only hypothesis. $\hat{\theta}_\mu$ denotes the point in the nuisance parameter space for which the numerator maximizes (while μ is held at zero). In the denominator the likelihood is maximized over the full (μ, θ) space. $(\hat{\mu}, \hat{\theta})$ is the point in parameter space where the maximum of the denominator occurs.

For a shape based analysis the likelihood gets modified with a product over all bins of

the photon p_T histogram.

$$\mathcal{L}(\text{data}|\mu, \theta) = \prod_i \frac{(\mu s_i + b_i)^{n_i}}{n_i!} e^{-(\mu s_i + b_i)} \quad (5.9)$$

The systematic errors are folded into this likelihood function as another multiplicative likelihood term. To obtain this auxiliary term, a Bayesian approach is taken. Given the estimated value ($\tilde{\theta}$) of the nuisance parameters (which, in the present context, are the bin by bin estimated backgrounds), the experimenter's degree of belief in the true value of the parameters (θ) is expressed with some well behaved density function $\rho(\theta|\tilde{\theta})$. In this analysis a log-normal distribution was chosen for $\rho(\theta|\tilde{\theta})$. If the density function $\rho(\theta|\tilde{\theta})$ is interpreted as a posterior probability function, then using Bayes theorem:

$$\rho(\theta|\tilde{\theta}) \sim p(\tilde{\theta}|\theta) \cdot \pi(\theta) \quad (5.10)$$

the likelihood $p(\tilde{\theta}|\theta)$ of obtaining the observed nuisance parameters ($\tilde{\theta}$) can be obtained, under the assumption of a flat prior, $\pi(\theta)$. Then the likelihood statistic, with systematic errors incorporated becomes,

$$\mathcal{L}(\text{data}|\mu, \theta) = \prod_i \frac{(\mu s_i + b_i)^{n_i}}{n_i!} e^{-(\mu s_i + b_i)} \cdot \rho(\theta|\tilde{\theta}) \quad (5.11)$$

The K-factor systematic is taken to be fully correlated amongst bins since all bins are simultaneously affected in the same direction with a systematic variation of the k-factor due to change in choice of pdf or scale or the value of α_s .

The level of incompatibility of data with the ADD model varies from point to point in the parameter space (M_D, n). An upper limit on the signal cross section has been computed for all M_D values, such that the $CL_S < 0.05$, corresponding to a 95% C.L. The region of the parameter space where the ADD model predicted signal cross section is more than the measured upper limit on cross section, is reported as excluded.

The expected and observed 95% CL limits are summarized in Table 5.11. Figure 5.15a shows the shape based limits on the signal cross section compared to the counting experiment limits in figure 5.15b along with the cross section for 4 extra dimensions as a function of M_D . As can be seen from these, the shape based limit improves compared to the counting experiment. Also, a check is done where the limits are obtained bin by bin where one observes that within a particular p_T bin, the expected and observed limit between various signal points is different. This happens due to the translation of the limit

M_D (TeV)	σ (fb)			
	n=3	n=4	n=5	n=6
1	12.9(19.6)	14.3(20.9)	13.9(20.4)	13.1(19.7)
2	10.4(16.5)	10.1(16.1)	9.9(15.8)	10.0(15.9)
3	9.2(14.7)	9.3(14.7)	9.3(14.8)	9.2(14.8)

Table 5.11: ADD 95% CL observed(expected) limits on the cross section as a function of M_D and n ($p_T > 130$ GeV).

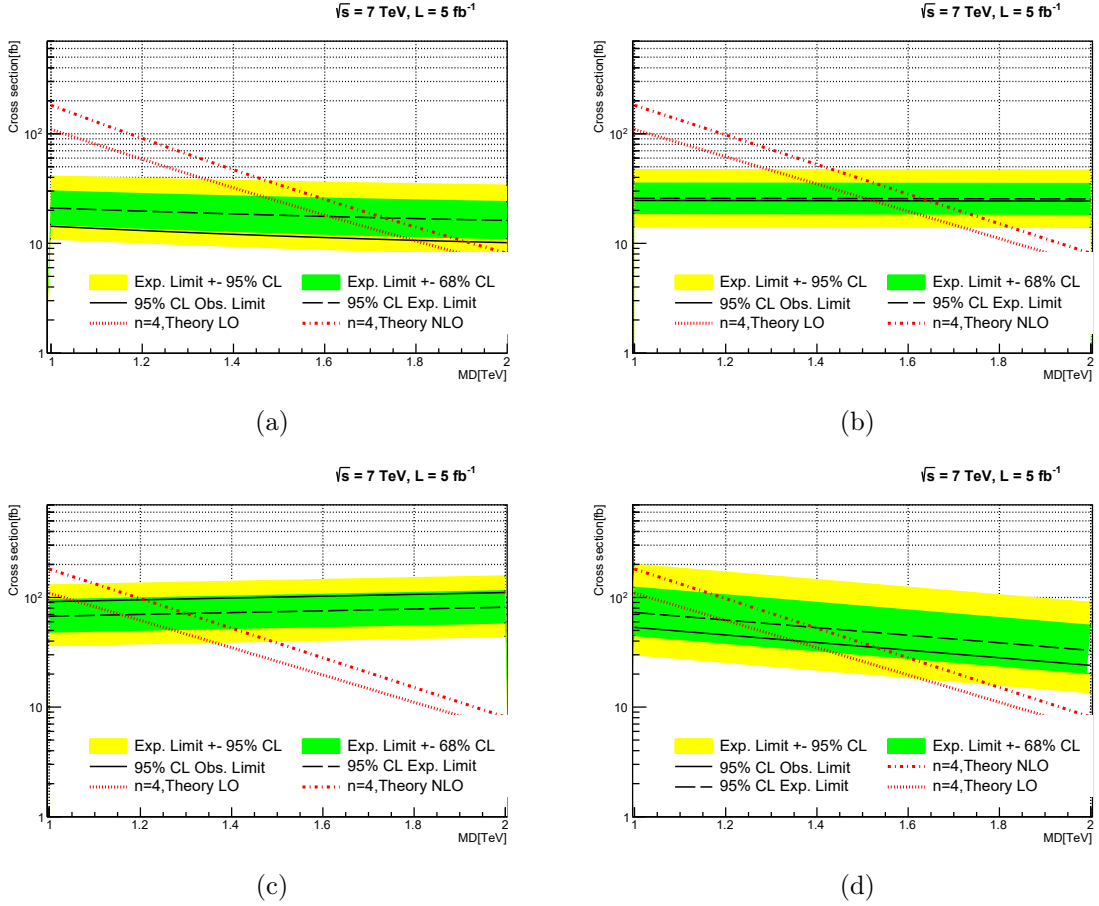


Figure 5.15: 95% CL upper limit on the cross section is plotted along with the cross-section for 4 extra dimensions as a function of M_D a) using shape based limit b) using counting limit for all the p_T bins c) using only first p_T bin and d) using only fifth p_T bin.

from number of events to the limit on the cross-section where $A \times \epsilon$ differs from one signal point to another for a given p_T bin.

Limits on M_D with and without k-factors are summarized in Table 5.12.

n	Obs.Limit(with k-factor) [TeV]	Obs.Limit(without k-factor) [TeV]
3	2.00	1.96
4	1.99	1.96
5	1.98	1.97
6	1.98	1.97

Table 5.12: 95%CL observed limits on M_D as a function of n, with and without the k-factor applied

A comparison with the existing limits from the Tevatron and LEP, a counting experiment at CMS and shape based limits are shown in Figure 5.16. The limits on the ADD model of large extra dimensions for the $\gamma + \cancel{E}_T$ topology are extended by this present measurement at $\sqrt{s} = 7$ TeV and an integrated luminosity of 4.994 fb^{-1} . M_D values up to ~ 2 TeV at a 95% confidence level using NLO calculation are excluded.

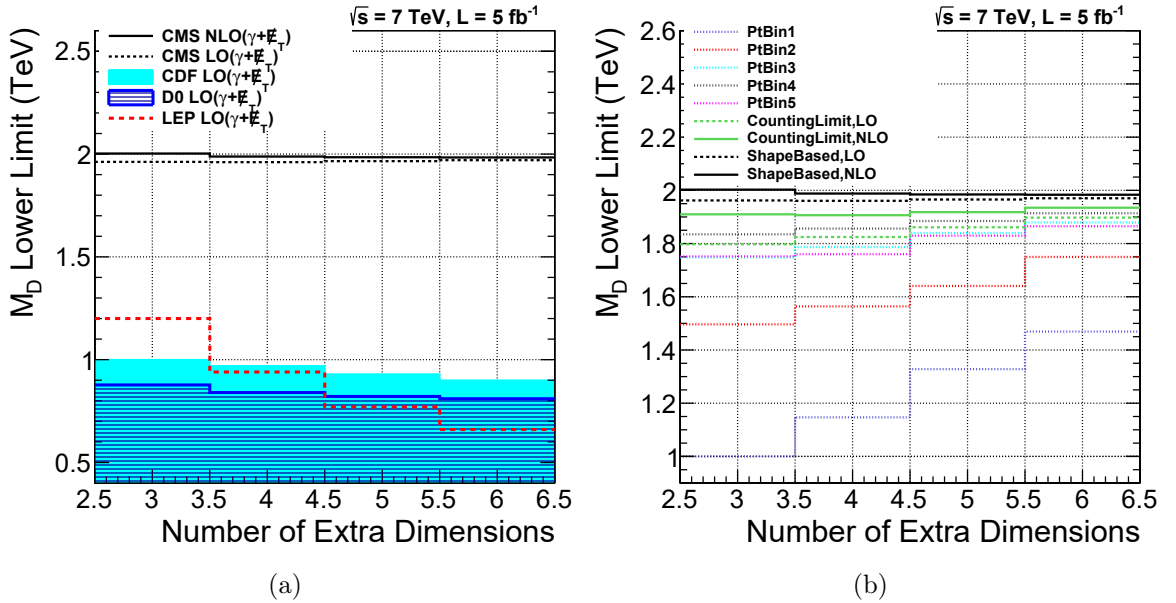


Figure 5.16: a) Limits on M_D as a function of n and comparison with LEP and Tevatron results for $\gamma + \cancel{E}_T$. b) Limits on M_D as a function of n and comparison between shape-based and counting limits within the CMS experiment.

5.10 Summary

A study of events with a photon and missing transverse energy in the final state is performed with pp collision data at $\sqrt{s} = 7 \text{ TeV}$ and 4.994 fb^{-1} of integrated luminosity taken

by the Compact Muon Solenoid detector at the LHC. A total of 73 events is observed with the monophoton signature in the data. This is in good agreement with the prediction from the Standard Model of 75.3 ± 9.7 events. The cross section is measured to be 21.2 ± 4.2 (stat.) ± 4.3 (syst.) ± 0.5 (lumi.) fb for $Z(\nu\bar{\nu})+\gamma$ process with $p_T^\gamma > 145$ GeV and $|\eta|^\gamma < 1.4$, in good agreement with the theoretical prediction of 21.9 ± 1.1 fb. The measurement is interpreted as a limit on the parameter space of the ADD model of large extra dimensions. The limits imposed by this measurement are $M_D > 2.00 - 1.98$ TeV for $n = 3 - 6$, which are an extension of the current limits set by measurements in the $\gamma + \cancel{E}_T$ topology.

Bibliography

- [1] J. J. Thomson. XXIV. On the structure of the atom: an investigation of the stability and periods of oscillation of a number of corpuscles arranged at equal intervals around the circumference of a circle; with application of the results to the theory of atomic structure. *Philosophical Magazine Series 6*, 7:39:237–265, 1904. <http://dx.doi.org/10.1080/14786440409463107>.
- [2] E. Rutherford. The Scattering of α and β Particles by Matter and the Structure of the Atom. *Philosophical Magazine Series 6*, 21:669–688, 1911. <http://www.lawebdefisica.com/arts/structureatom.pdf>.
- [3] J. Chadwick. Possible Existence of a Neutron. *Nature*, 129:312, 1932. <http://www.nature.com/nature/journal/v129/n3252/abs/129312a0.html>.
- [4] M. Glashow. Partial symmetries of weak interactions. *Nucl. Phys.*, 22:579–588, 1961. <http://www.sciencedirect.com/science/article/pii/0029558261904692>.
- [5] S. Weinberg. A model of leptons. *Phys. Rev. Lett.*, 19:1264–1266, 1967. <http://journals.aps.org/prl/abstract/10.1103/PhysRevLett.19.1264>.
- [6] A. Salam. Weak and electromagnetic interactions. in *Elementary particle physics: relativistic groups and analyticity* (N. Svartholm, ed.), p. 367, *Almqvist and Wiskell. Proceedings of the eights Nobel symposium*, 1968.
- [7] Michael E. Peskin and Daniel V. Schroeder. *An Introduction to Quantum Field Theory*. Perseus Books, Cambridge, Massachusetts, 1995.
- [8] Francis Halzen and Alan Martin. *Quarks & Leptons: An introductory course in modern particle physics*. John Wiley & Sons, New York, USA, 1984.
- [9] Pasquale Musella. Measurement of the inclusive photon production cross section and study of associated W-photon production in proton-proton collisions at the LHC. *CERN-THESIS-2011-050*, 2011.

- [10] R. Brout F. Englert. Broken symmetry and the mass of gauge vector mesons. *Phys. Rev. Lett.*, 13:321–323, 1964. <http://journals.aps.org/prl/abstract/10.1103/PhysRevLett.13.321>.
- [11] P.W. Higgs. Broken symmetry and the masses of gauge fields. *Phys. Rev. Lett.*, 13:508, 1964. <http://journals.aps.org/prl/abstract/10.1103/PhysRevLett.13.508>.
- [12] C.R. Hagen G.S. Guralnik and T.W.B. Kibble. Global conservation laws and massless particles. *Phys. Rev. Lett.*, 13:585–587, 1964. <http://journals.aps.org/prl/abstract/10.1103/PhysRevLett.13.585>.
- [13] S. Weinberg J. Goldstone, A. Salam. Broken symmetries. *Phys. Rev.*, 127:965–970. <http://journals.aps.org/pr/abstract/10.1103/PhysRev.127.965>.
- [14] Nima Arkani-Hamed, Savas Dimopoulos, and G.R. Dvali. The Hierarchy problem and new dimensions at a millimeter. *Phys.Lett.*, B429:263–272, 1998. [http://dx.doi.org/10.1016/S0370-2693\(98\)00466-3](http://dx.doi.org/10.1016/S0370-2693(98)00466-3).
- [15] Lisa Randall and Raman Sundrum. A Large mass hierarchy from a small extra dimension. *Phys.Rev.Lett.*, 83:3370–3373, 1999. <http://dx.doi.org/10.1103/PhysRevLett.83.3370>.
- [16] Gian F. Giudice, Riccardo Rattazzi, and James D. Wells. Quantum gravity and extra dimensions at high-energy colliders. *Nucl.Phys.*, B544:3–38, 1999. [http://dx.doi.org/10.1016/S0550-3213\(99\)00044-9](http://dx.doi.org/10.1016/S0550-3213(99)00044-9).
- [17] G L Landsberg. Extra Dimensions and More. Technical Report hep-ex/0105039, May 2001. <http://cds.cern.ch/record/500268/>.
- [18] Steen Hannestad and Georg G. Raffelt. Supernova and neutron star limits on large extra dimensions reexamined. *Phys.Rev.*, D67:125008, 2003. <http://dx.doi.org/10.1103/PhysRevD.69.029901>.
- [19] C.D. Hoyle, U. Schmidt, Blayne R. Heckel, E.G. Adelberger, J.H. Gundlach, et al. Submillimeter tests of the gravitational inverse square law: a search for 'large' extra dimensions. *Phys.Rev.Lett.*, 86:1418–1421, 2001. <http://dx.doi.org/10.1103/PhysRevLett.86.1418>.
- [20] Serguei Chatrchyan et al. Search for Large Extra Dimensions in the Diphoton Final State at the Large Hadron Collider. *JHEP*, 1105:085, 2011. [http://dx.doi.org/10.1007/JHEP05\(2011\)085](http://dx.doi.org/10.1007/JHEP05(2011)085).

- [21] Serguei Chatrchyan et al. Search for large extra dimensions in dimuon and dielectron events in pp collisions at $\sqrt{s} = 7$ TeV. *Phys.Lett.*, B711:15–34, 2012. <http://dx.doi.org/10.1016/j.physletb.2012.03.029>.
- [22] Serguei Chatrchyan et al. Search for Dark Matter and Large Extra Dimensions in pp Collisions Yielding a Photon and Missing Transverse Energy. *Phys.Rev.Lett.*, 108:261803, 2012. <http://dx.doi.org/10.1103/PhysRevLett.108.261803>.
- [23] Serguei Chatrchyan et al. Search for New Physics with a Mono-Jet and Missing Transverse Energy in pp Collisions at $\sqrt{s} = 7$ TeV. *Phys.Rev.Lett.*, 107:201804, 2011. <http://dx.doi.org/10.1103/PhysRevLett.107.201804>.
- [24] Serguei Chatrchyan et al. Search for dark matter and large extra dimensions in monojet events in pp collisions at $\sqrt{s} = 7$ TeV. *JHEP*, 1209:094, 2012. [http://dx.doi.org/10.1007/JHEP09\(2012\)094](http://dx.doi.org/10.1007/JHEP09(2012)094).
- [25] Lyndon R Evans and Philip Bryant. LHC Machine. *J. Instrum.*, 3:S08001. 164 p, 2008. <https://cds.cern.ch/record/1129806/>.
- [26] S. Chatrchyan et al. The CMS experiment at the CERN LHC. *JINST*, 3:S08004, 2008. <http://dx.doi.org/10.1088/1748-0221/3/08/S08004>.
- [27] Description and performance of the CMS track and primary vertex reconstruction. Technical Report CMS-PAS-TRK-11-001, CMS collaboration, CERN, Geneva, 2013. <http://cms.cern.ch/iCMS/analysisadmin/cadi?ancode=TRK-11-001>.
- [28] *The CMS electromagnetic calorimeter project: Technical Design Report*. Technical Design Report CMS. CERN, Geneva, 1997. <https://cds.cern.ch/record/349375>.
- [29] CMS Collaboration. Energy resolution of the barrel of the CMS Electromagnetic Calorimeter. Technical report, 2007. <http://dx.doi.org/10.1088/1748-0221/2/04/P04004>.
- [30] Photon reconstruction and identification at $\sqrt{s} = 7$ TeV. Technical Report CMS-PAS-EGM-10-005, CERN, 2010. Geneva, 2010. <https://cds.cern.ch/record/1279143/>.
- [31] CMS Collaboration. Energy calibration and resolution of the CMS electromagnetic calorimeter in pp collisions at $\sqrt{s} = 7$ TeV. *JINST*, 8(arXiv:1306.2016. CMS-EGM-11-001. CERN-PH-EP-2013-097):P09009. 51 p, Jun 2013. <https://cds.cern.ch/record/1554142/>.

- [32] Met performance in 8 TeV data. Technical Report CMS-PAS-JME-12-002, CERN, Geneva, 2013. <https://cds.cern.ch/record/1543527/>.
- [33] CMS Collaboration. Missing transverse energy performance of the CMS detector. *JINST*, 6(arXiv:1106.5048. CMS-JME-10-009. CERN-PH-EP-2011-051):P09001. 56 p, Jun 2011. <https://cds.cern.ch/record/1361632/>.
- [34] *The CMS muon project: Technical Design Report*. Technical Design Report CMS. CERN, Geneva, 1997. <https://cds.cern.ch/record/343814>.
- [35] S. Agostinelli et al. GEANT4: A Simulation toolkit. *Nucl.Instrum.Meth.*, A506:250–303, 2003. [http://dx.doi.org/10.1016/S0168-9002\(03\)01368-8](http://dx.doi.org/10.1016/S0168-9002(03)01368-8).
- [36] *CMS The TriDAS Project: Technical Design Report, Volume 2: Data Acquisition and High-Level Trigger. CMS trigger and data-acquisition project*. Technical Design Report CMS. CERN, Geneva, 2002. <https://cds.cern.ch/record/578006>.
- [37] *CMS TriDAS project: Technical Design Report, Volume 1: The Trigger Systems*. Technical Design Report CMS. CERN, Geneva, 2000. <https://cds.cern.ch/record/706847>.
- [38] *CMS Physics: Technical Design Report Volume 1: Detector Performance and Software*. Technical Design Report CMS. CERN, Geneva, 2006. <https://cds.cern.ch/record/922757>.
- [39] Tracking and Vertexing Results from First Collisions. Technical Report CMS-PAS-TRK-10-001, CERN, 2010. Geneva, 2010. <https://cds.cern.ch/record/1258204/>.
- [40] Tracking and Primary Vertex Results in first 7 TeV Collisions. Technical Report CMS-PAS-TRK-10-005, CERN, 2010. Geneva, 2010. <https://cds.cern.ch/record/1279383/>.
- [41] R Fruhwirth, Wolfgang Waltenberger, and Pascal Vanlaer. Adaptive Vertex Fitting. Technical Report CMS-NOTE-2007-008, CERN, Geneva, Mar 2007. <https://cds.cern.ch/record/1027031/>.
- [42] Electron reconstruction and identification at $\sqrt{s} = 7$ TeV. Technical Report CMS-PAS-EGM-10-004, CERN, Geneva, 2010. <https://cds.cern.ch/record/1299116/>.
- [43] CMS Collaboration. Search for supersymmetry in events with photons and low missing transverse energy in pp collisions at $\sqrt{s} = 7$ TeV. *Phys. Lett. B*,

- 719(arXiv:1210.2052. CMS-SUS-12-014. CERN-PH-EP-2012-272):42–61. 27 p, Oct 2012. <https://cds.cern.ch/record/1483525/>.
- [44] CMS Collaboration. Performance of CMS muon reconstruction in pp collision events at $\sqrt{s} = 7$ TeV. *JINST*, 7(arXiv:1206.4071. CMS-MUO-10-004. CERN-PH-EP-2012-173):P10002. 81 p, 2012. <http://iopscience.iop.org/1748-0221/7/10/P10002>.
 - [45] Commissioning of the Particle-flow Event Reconstruction with the first LHC collisions recorded in the CMS detector. Technical Report CMS-PAS-PFT-10-001, 2010. <https://cds.cern.ch/record/1247373/>.
 - [46] Particle-flow event reconstruction in cms and performance for jets, taus, and met. Technical Report CMS-PAS-PFT-09-001, CERN, 2009. Geneva, Apr 2009. <https://cds.cern.ch/record/1194487/>.
 - [47] Matteo Cacciari, Gavin P. Salam, and Gregory Soyez. The Anti-k(t) jet clustering algorithm. *JHEP*, 0804:063, 2008. doi:<http://dx.doi.org/10.1088/1126-6708/2008/04/063>.
 - [48] M. Anderson et al. Review of clustering algorithms and energy corrections in ECAL. Technical Report CMS-IN-10-008, 2010. https://cms.cern.ch/iCMS/jsp/openfile.jsp?type=IN&year=2010&files=IN2010_008.pdf.
 - [49] Torbjorn Sjostrand, Stephen Mrenna, and Peter Z. Skands. PYTHIA 6.4 Physics and Manual. *JHEP*, 0605:026, 2006. <http://dx.doi.org/10.1088/1126-6708/2006/05/026>.
 - [50] Johan Alwall, Michel Herquet, Fabio Maltoni, Olivier Mattelaer, and Tim Stelzer. MadGraph 5 : Going Beyond. *JHEP*, 1106:128, 2011. [http://dx.doi.org/10.1007/JHEP06\(2011\)128](http://dx.doi.org/10.1007/JHEP06(2011)128).
 - [51] Piet Verwilligen. Data driven determination of $Z\nu\nu$ background to new-physics searches with jets and missing transverse momentum at CMS. *CERN-THESIS-2012-150*, 2012.
 - [52] R.M. Brown, K. Deiters, Q. Ingram, and D. Renker. Response of CMS avalanche photo-diodes to low energy neutrons. *Nucl.Instrum.Meth.*, A695:146–149, 2012. <http://dx.doi.org/10.1016/j.nima.2011.12.005>.
 - [53] David A. Petyt. Anomalous APD signals in the CMS Electromagnetic Calorimeter. *Nucl.Instrum.Meth.*, A695:293–295, 2012. <http://dx.doi.org/10.1016/j.nima.2011.10.025>.

- [54] Pascal Paganini. CMS Electromagnetic Trigger commissioning and first operation experiences. Technical Report J. Phys.: Conf. Ser. 160 01206, CERN, Geneva, 2009. <http://iopscience.iop.org/1742-6596/160/1/012062>.
- [55] Alexandre Zabi. Triggering on electrons and photons with CMS. Technical Report CMS-CR-2012-028. CERN-CMS-CR-2012-028, CERN, Geneva, Jan 2012. <http://cds.cern.ch/record/1454210/>.
- [56] Alexandre Zabi. Triggering on electrons and photons with the CMS experiment at the LHC. Technical Report CMS-CR-2012-211. CERN-CMS-CR-2012-211, CERN, Geneva, Aug 2012. <https://cds.cern.ch/record/1484864/>.
- [57] <http://goo.gl/kpAJBD>.
- [58] <https://twiki.cern.ch/twiki/bin/viewauth/CMS/EcalAPDSimulation>.
- [59] CMS Collaboration. APD dark current evolution in CMS. *CMS Detector Note*, 2013/015, 2013. In preparation.
- [60] CMS Collaboration. Simulation of the CMS ECAL noise in the LHC RUN1. *CMS Analysis Note*, 2013/331, 2013. In preparation.
- [61] CMS Collaboration. Tuning of out-of-time pileup simulation with CMS ECAL data. *CMS Analysis Note*, 2013/330, 2013. In preparation.
- [62] CMS Collaboration. Mitigation of anomalous signals in the CMS ECAL. *CMS Analysis Note*, 2013/329, 2013. In preparation.
- [63] Torbjorn Sjostrand, Stephen Mrenna, and Peter Z. Skands. A Brief Introduction to PYTHIA 8.1. *Comput.Phys.Commun.*, 178:852–867, 2008. <http://dx.doi.org/10.1016/j.cpc.2008.01.036>.
- [64] U. Baur, T. Han, and J. Ohnemus. QCD corrections to hadronic $W\gamma$ production with nonstandard $WW\gamma$ couplings. *Phys.Rev.*, D48:5140–5161, 1993. <http://dx.doi.org/10.1103/PhysRevD.48.5140>.
- [65] <https://twiki.cern.ch/twiki/bin/view/CMSPublic/SWGuideEJTermBeamHaloId>.
- [66] <https://twiki.cern.ch/twiki/bin/viewauth/CMS/Vgamma2011PhotonID>.
- [67] CMS Collaboration. Study of $W\gamma$ and $Z\gamma$ production at CMS with $\sqrt{s} = 7$ TeV. *CMS Analysis Note*, 2011/251, 2011.

- [68] CMS Collaboration. $Z\gamma$ at $\sqrt{s} = 7$ TeV where Z Decays Invisibly. *CMS Analysis Note*, 2011/108, 2011.
- [69] <https://twiki.cern.ch/twiki/bin/view/CMS/PileupRewighting>.
- [70] <http://root.cern.ch/root/html/doc/TFractionFitter.html>.
- [71] CMS Collaboration. Search for Gauge Mediated Supersymmetry Breaking Using Two Photons and Missing Transverse Energy. *CMS Analysis Note*, 2011/515, 2011.
- [72] V. Gaultney, Y. Gershtein, A. Askew. Beam Halo Tagging Study Using Correlations in the Electromagnetic and Hadronic Calorimeters. *CMS AN-2009/052*, 2009.
- [73] CMS Collaboration. Search for ADD Extra-dimensions with Photon + MET signature. *CMS Analysis Note*, 2011/319, 2011.
- [74] J. Pumplin, D.R. Stump, J. Huston, H. Lai, P. Nadolsky, and W. Tung. New generation of parton distributions with uncertainties from global QCD analysis. *JHEP*, 07:012, 2002.
- [75] A.D. Martin, W.J. Stirling, R.S. Thorne, and G. Watt. Parton distributions for the LHC. *Eur. Phys. J. C*, 63:189, 2009.
- [76] M. Botje, J. Butterworth, A. Cooper-Sarkar, A. de Roeck, J. Feltesse, S. Forte, A. Glazov, J. Huston, R. McNulty, Torbjorn Sjöstrand, and Robert Thorne. The PDF4LHC Working Group Interim Recommendations. arXiv:1101.0538, 2011.
- [77] <https://twiki.cern.ch/twiki/bin/view/CMSPublic/SWGuideEWKUtilities>.
- [78] CMS Collaboration. Determination of Jet Energy Calibration and Transverse Momentum Resolution in CMS. *JINST*, 06:11002, 2011.
- [79] The CMS Collaboration. Jet Resolution Determination at $\sqrt{s} = 7$ TeV. *JME-10-009*, 2010.
- [80] The CMS Collaboration. Measurement of the production cross section for $Z\gamma \rightarrow \nu\bar{\nu}\gamma$ in pp collisions at $\sqrt{s} = 7$ TeV and limits on $ZZ\gamma$ and $Z\gamma\gamma$ triple gauge couplings. *SMP-12-020*, 2012.
- [81] G. Cowan, K. Cranmer, E. Gross, O. Vitells. Asymptotic formulae for likelihood-based tests of new physics. *Eur.Phys.J., C* 71:1554, 2011.
- [82] CMS Collaboration. Procedure for the LHC Higgs boson search combination in summer 2011. *CMS Analysis Note*, 2011/298, 2011.

Appendices

Appendix A

List of samples used for the analysis

A.1 Data Samples

To select events in data, a skimming criteria has been applied based on the activity seen in ECAL and HCAL only.

- $E_T^\gamma > 130$ GeV.
- ratio of hadronic energy to electromagnetic energy (H/E) < 0.05 .

The datasets skimmed for this analysis are listed in Table [A.1](#).

Data Samples
/Photon/Run2011A-May10ReReco-v1/AOD
/Photon/Run2011A-PromptReco-v4/AOD
/Photon/Run2011A-PromptReco-v6/AOD
/Photon/Run2011A-05Aug2011-v1/AOD
/Photon/Run2011B-PromptReco-v1/AOD

Table A.1: List of datasets used in this analysis.

A.2 Monte Carlo samples

The Monte Carlo simulated backgrounds are used from the Summer11 official production where the effect of out-of-time pileup has been included with the bunch structure of $[-3, +2]$ at 50 ns. The background sample of $Z(\nu\bar{\nu})+\gamma$ events was not available in Summer11 production, thus a private sample is generated using official tools to maintain the consistency of the generated events. For the diboson backgrounds, samples are generated privately as well. These private samples are all generated including pileup, which is necessary as the increased instantaneous luminosity of the 2011 LHC data has an effect on

detector performance and background estimation. These samples have been reconstructed using CMSSW_4_2_3. The following parameters are used for the production of all the MCs:

- Center of mass energy 7 TeV
- Magnetic field 3.8 Tesla
- Out-of-time pileup
- Detector calibration and alignment using START conditions
- Global Tag used for simulation: MC_42_V12
- For Jet Energy Correction(JEC) *L1FastJet*, *L2Relative* and *L3Absolute* corrections are applied on particle flow jets.

The MC samples used are listed in Table A.2 and A.3.

M_D , TeV	n	DataSet Name	Events	Lumi,fb ⁻¹
1	3	/ADDmonoPhoton_MD-1_d-3_7TeV-pythia8/Summer11-PU_S4_START42_V11-v1	54280	246
1	4	/ADDmonoPhoton_MD-1_d-4_7TeV-pythia8/Summer11-PU_S4_START42_V11-v1	51695	197
1	5	/ADDmonoPhoton_MD-1_d-5_7TeV-pythia8/Summer11-PU_S4_START42_V11-v1	51350	156
1	6	/ADDmonoPhoton_MD-1_d-6_7TeV-pythia8/Summer11-PU_S4_START42_V11-v1	52570	122
2	3	/ADDmonoPhoton_MD-2_d-3_7TeV-pythia8/Summer11-PU_S4_START42_V11-v1	52975	3529
2	4	/ADDmonoPhoton_MD-2_d-4_7TeV-pythia8/Summer11-PU_S4_START42_V11-v1	50688	3866
2	5	/ADDmonoPhoton_MD-2_d-5_7TeV-pythia8/Summer11-PU_S4_START42_V11-v1	52570	4403
2	6	/ADDmonoPhoton_MD-2_d-6_7TeV-pythia8/Summer11-PU_S4_START42_V11-v1	53380	4883
3	3	/ADDmonoPhoton_MD-3_d-3_7TeV-pythia8/Summer11-PU_S4_START42_V11-v1	55000	25183
3	4	/ADDmonoPhoton_MD-3_d-4_7TeV-pythia8/Summer11-PU_S4_START42_V11-v1	55000	38678
3	5	/ADDmonoPhoton_MD-3_d-5_7TeV-pythia8/Summer11-PU_S4_START42_V11-v1	55000	56381
3	6	/ADDmonoPhoton_MD-3_d-6_7TeV-pythia8/Summer11-PU_S4_START42_V11-v1	55000	78966

Table A.2: Details of the Monte Carlo samples used for ADD signal.

Process	DataSet Name	Events	Lumi, fb ⁻¹
$Z(\rightarrow \nu\bar{\nu}) + \gamma$	private production (Pythia)	100000	2630.194
$Z(\rightarrow ll) + \gamma + Jets(ee \text{ and } \mu\mu)$	private production (Madgraph)	754839	54.738
$W(\rightarrow l\nu) + \gamma + Jets$	private production (Madgraph)	1062987	49.649
$W \rightarrow e\nu$	/WToENu_TuneZ2_7TeV-pythia6/ Summer11-PU_S3_START42_V11-v2/AODSIM	5304113	0.671
$W \rightarrow \mu\nu$	/WToMuNu_TuneZ2_7TeV-pythia6/ Summer11-PU_S3_START42_V11-v2/AODSIM	3954916	0.500
$W \rightarrow \tau\nu$	/WToTauNu_TuneZ2_7TeV-pythia6/ Summer11-PU_S3_START42_V11-v2/AODSIM	3999901	0.506
Photon+ <i>Jet</i>	/G_Pt30to50_TuneZ2_7TeV_pythia6/ Summer11-PU_S3_START42_V11-v2/AODSIM	2177187	0.130
	/G_Pt-50to80_TuneZ2_7TeV_pythia6/ Summer11-PU_S3_START42_V11-v2/AODSIM	2016427	0.741
	/G_Pt-80to120_TuneZ2_7TeV_pythia6/ Summer11-PU_S4_START42_V11-v1/AODSIM	1625917	3.636
	/G_Pt-120to170_TuneZ2_7TeV_pythia6/ Summer11-PU_S3_START42_V11-v2/AODSIM	2066070	24.546
	/G_Pt-170to300_TuneZ2_7TeV_pythia6/ Summer11-PU_S4_START42_V11-v1/AODSIM	1496472	66.098
	/G_Pt-300to470_TuneZ2_7TeV_pythia6/ Summer11-PU_S3_START42_V11-v2/AODSIM	2070808	1.387×10^3
	/G_Pt-470to800_TuneZ2_7TeV_pythia6/ Summer11-PU_S3_START42_V11-v2/AODSIM	2050475	1.550×10^4
	/DiPhotonBorn_Pt-25To250_7TeV-pythia6/ Summer11-PU_S4_START42_V11-v2/AODSIM	532860	23.820
	/DiPhotonBorn_Pt-250_7TeV-pythia6/ Summer11-PU_S4_START42_V11-v2/AODSIM	526156	6.517×10^4
Diphoton (Box)	/DiPhotonBox_Pt-25To250_7TeV-pythia6/ Summer11-PU_S4_START42_V11-v2/AODSIM	510284	41.252
	/DiPhotonBox_Pt-250_7TeV-pythia6/ Summer11-PU_S4_START42_V11-v2/AODSIM	256518	1.233×10^6
QCD	/QCD_Pt-30to50_TuneZ2_7TeV_pythia6/ Summer11-PU_S3_START42_V11-v2/AODSIM	4919871	9.2×10^{-5}
	/QCD_Pt-50to80_TuneZ2_7TeV_pythia6/ Summer11-PU_S3_START42_V11-v2/AODSIM	4907406	7.7×10^{-4}
	/QCD_Pt-80to120_TuneZ2_7TeV_pythia6/ Summer11-PU_S3_START42_V11-v2/AODSIM	4827473	6.1×10^{-3}
	/QCD_Pt-120to170_TuneZ2_7TeV_pythia6/ Summer11-PU_S3_START42_V11-v2/AODSIM	4872513	4.2×10^{-2}
	/QCD_Pt-170to300_TuneZ2_7TeV_pythia6/ Summer11-PU_S3_START42_V11-v2/AODSIM	4953963	0.204
	/QCD_Pt-300to470_TuneZ2_7TeV_pythia6/ Summer11-PU_S3_START42_V11-v2/AODSIM	4938811	4.227
	/QCD_Pt-470to600_TuneZ2_7TeV_pythia6/ Summer11-PU_S3_START42_V11-v2/AODSIM	3934921	56.03370

Table A.3: Details of the simulated samples used for background analysis.

Appendix B

Selection optimization

The selection optimization aiming to improve ADD search sensitivity is performed at given integrated luminosity. For the optimization, 1.14 fb^{-1} of data is used. Best sensitivity is given by the selection which provides the lowest value for the expected upper limit on the ADD cross section at 95 % CL. The cut values for the photon P_T^γ , E_T , jet and track veto have been optimized. Each cut value is varied separately or in combination with the correlated variable with it (jet and track veto, for example).

B.1 Photon P_T^γ and E_T combined cut optimization

Since, photon P_T^γ and the E_T are highly correlated variables in the monophoton final state, it is chosen to vary photon P_T^γ and E_T cut values at once while keeping them equal. Summary of the scan is given in table B.1.

Scenario	N_{BG}	$A \times \epsilon_{MC}$	Expected Limit 95CL σ, fb
$P_T^\gamma > 95, E_T > 95, P_T^{Jet} < 20, P_T^{Trk} < 10$	60.25 ± 8.01	0.177 ± 0.022	119
$P_T^\gamma > 110, E_T > 110, P_T^{Jet} < 20, P_T^{Trk} < 10$	36.65 ± 5.29	0.128 ± 0.017	118
$P_T^\gamma > 130, E_T > 130, P_T^{Jet} < 20, P_T^{Trk} < 10$	20.59 ± 3.35	0.095 ± 0.012	119
$P_T^\gamma > 160, E_T > 160, P_T^{Jet} < 20, P_T^{Trk} < 10$	8.79 ± 1.79	0.0613 ± 0.0086	126
$P_T^\gamma > 200, E_T > 200, P_T^{Jet} < 20, P_T^{Trk} < 10$	3.07 ± 0.63	0.0363 ± 0.0049	138
$P_T^\gamma > 300, E_T > 300, P_T^{Jet} < 20, P_T^{Trk} < 10$	0.51 ± 0.13	0.0099 ± 0.0016	281

Table B.1: ADD search sensitivity: $P_T^\gamma = E_T$ scan.

It is observed that for values of $P_T^\gamma = E_T$ in the range of 95-130 GeV, the expected upper limit for ADD cross section has a constant value of about 120 fb, while for $P_T^\gamma = E_T > 160$ GeV the sensitivity decreases with the increase of the photon P_T^γ cutoff. Thus, this suggests the optimal photon P_T^γ cut to be below 160 GeV. After taking into account

the HLT P_T^γ threshold requirement and efficiency turn-on , $P_T^\gamma > 145$ GeV was chosen as optimal threshold for the analysis.

B.2 \cancel{E}_T cut optimization

While P_T^γ and \cancel{E}_T are highly correlated in the monophoton topology, an additional hadronic activity in the event suggest that cut on \cancel{E}_T could be further optimized with respect to the photon P_T^γ . Choosing a lower cut on the \cancel{E}_T would minimize the effect on the selection from that additional hadronic activity. Therefore, to have a \cancel{E}_T equal or lower than the P_T^γ cut is considered and \cancel{E}_T cut optimization scan is performed in the vicinity of the P_T^γ value. Table B.2 summarizes the resulting effect on expected upper limit of the ADD cross section. The overall observation shows a minimal dependence on the \cancel{E}_T cut value for the tested range and thus $\cancel{E}_T > 130$ GeV is selected to be used in conjunction with $P_T^\gamma > 145$ GeV.

Scenario	N_{BG}	$A \times \epsilon_{MC}$	Expected Limit 95CL σ, fb
$P_T^\gamma > 95, \cancel{E}_T > 80, P_T^{J\text{et}} < 20, P_T^{Trk} < 10$	67.25 ± 8.44	0.189 ± 0.022	118
$P_T^\gamma > 95, \cancel{E}_T > 90, P_T^{J\text{et}} < 20, P_T^{Trk} < 10$	62.56 ± 8.10	0.183 ± 0.022	116
$P_T^\gamma > 95, \cancel{E}_T > 95, P_T^{J\text{et}} < 20, P_T^{Trk} < 10$	60.25 ± 8.01	0.177 ± 0.022	119
$P_T^\gamma > 95, \cancel{E}_T > 80, P_T^{J\text{et}} < 30, P_T^{Trk} < 15$	87.71 ± 9.99	0.255 ± 0.029	100
$P_T^\gamma > 95, \cancel{E}_T > 90, P_T^{J\text{et}} < 30, P_T^{Trk} < 15$	81.53 ± 9.27	0.246 ± 0.028	103
$P_T^\gamma > 95, \cancel{E}_T > 95, P_T^{J\text{et}} < 30, P_T^{Trk} < 15$	77.88 ± 9.49	0.238 ± 0.029	100

Table B.2: ADD search sensitivity : \cancel{E}_T scan.

B.3 Jet and track veto optimization

Jet and track vetoes are highly correlated, therefore for the optimization a simultaneous variation in the cut values is surveyed. Five different selection scenarios are chosen, defined by the P_T^γ and \cancel{E}_T selection cuts and then the variation of the jet and track veto. All five scenarios show same trend as a function of the veto - ADD search sensitivity improves by relaxing the veto, while the value $P_T^{J\text{et}} < 40, P_T^{Trk} < 20$ are reached. Summary of the scan is shown in table B.3.

Scenario	N_{BG}	$A \times \epsilon_{MC}$	Expected Limit 95CL σ ,fb
$P_T^\gamma > 95, \cancel{E}_T > 80, P_T^{Jet} < 20, P_T^{Trk} < 10$	67.25 ± 8.44	0.189 ± 0.022	118
$P_T^\gamma > 95, \cancel{E}_T > 80, P_T^{Jet} < 30, P_T^{Trk} < 15$	87.71 ± 9.99	0.255 ± 0.029	101
$P_T^\gamma > 95, \cancel{E}_T > 90, P_T^{Jet} < 20, P_T^{Trk} < 10$	62.56 ± 8.10	0.183 ± 0.0222	116
$P_T^\gamma > 95, \cancel{E}_T > 90, P_T^{Jet} < 30, P_T^{Trk} < 15$	81.53 ± 9.27	0.246 ± 0.0281	99
$P_T^\gamma > 95, \cancel{E}_T > 95, P_T^{Jet} < 20, P_T^{Trk} < 10$	60.25 ± 8.01	0.177 ± 0.022	119
$P_T^\gamma > 95, \cancel{E}_T > 95, P_T^{Jet} < 30, P_T^{Trk} < 15$	77.88 ± 9.49	0.238 ± 0.029	100
$P_T^\gamma > 95, \cancel{E}_T > 95, P_T^{Jet} < 40, P_T^{Trk} < 20$	92.75 ± 10.39	0.255 ± 0.032	96
$P_T^\gamma > 95, \cancel{E}_T > 95, P_T^{Jet} < 50, P_T^{Trk} < 35$	106.46 ± 11.2	0.280 ± 0.035	97
$P_T^\gamma > 140, \cancel{E}_T > 130, P_T^{Jet} < 20, P_T^{Trk} < 10$	16.8 ± 3.3	$0.086 \pm .011$	121
$P_T^\gamma > 140, \cancel{E}_T > 130, P_T^{Jet} < 30, P_T^{Trk} < 15$	23.4 ± 3.5	$0.117 \pm .015$	97
$P_T^\gamma > 140, \cancel{E}_T > 130, P_T^{Jet} < 40, P_T^{Trk} < 20$	26.9 ± 3.9	$0.135 \pm .017$	92
$P_T^\gamma > 180, \cancel{E}_T > 170, P_T^{Jet} < 20, P_T^{Trk} < 10$	5.0 ± 0.9	0.0490 ± 0.0065	121
$P_T^\gamma > 180, \cancel{E}_T > 170, P_T^{Jet} < 30, P_T^{Trk} < 15$	6.2 ± 1.0	0.0675 ± 0.0087	92
$P_T^\gamma > 180, \cancel{E}_T > 170, P_T^{Jet} < 40, P_T^{Trk} < 20$	8.1 ± 1.4	0.0787 ± 0.0097	90

Table B.3: ADD search sensitivity: jet and track veto scan.